NORTHWESTERN UNIVERSITY

Motion of Thin Droplets Due to Surfactants and Gravity

A DISSERTATION

SUBMITTED TO THE GRADUATE SCHOOL
IN PARTIAL FULFILLMENT OF THE REQUIREMENTS

for the degree of
DOCTOR OF PHILOSOPHY
Field of Applied Mathematics

By
Matthew Allen Clay

EVANSTON, ILLINOIS
June 2007

© Copyright by Matthew Allen Clay 2007
All Rights Reserved

ABSTRACT

Motion of Thin Droplets
Due to Surfactants and Gravity

Matthew Allen Clay

The motion of thin drops under the effects of surfactants and gravity is studied. First, the effects of surfactant and temperature on the spreading of a viscous droplet are considered. Lubrication theory is used to develop a two-dimensional model for the evolution of the droplet. The surfactant is assumed to be insoluble, and it may transport onto and off of the droplet interface at the contact line. A linear temperature gradient and a gradient in the surface energy along the substrate are examined. We find that these effects together can increase the speed of the translation of the droplet. When contact-angle hysteresis is included, surfactant transport along the interface can cause the droplet to stop moving. These results are compared with a three-dimensional axisymmetric lubrication model and are found to be in good agreement. A fully three-dimensional lubrication model is formed that allows the droplet to translate down an inclined plane. Critical Bond numbers and angles of inclination are calculated for when the droplet remains pinned to the plane. A larger hysteresis window is found to require a higher Bond number to force the droplet to begin moving. These results compare favorably with other published studies. We construct a stability diagram that details the Bond numbers for which the droplet will remain pinned to the surface, when it will translate at a steady speed, and when it will begin to deform. The formation of cusps and pearling behavior of droplets is discussed.

Acknowledgments

I would like to thank my adviser, Michael J. Miksis, for his support during my studies. I would also like to thank my other committee members, David Chopp and Stephen H. Davis, for the helpful comments on this thesis. While these fine professors were the ones who helped the most with my thesis, every professor in Applied Mathematics has been very helpful and friendly to me, and they all get my heartfelt thanks.

But it is not just the professors who make a department great. I would not have been able to navigate through the Northwestern paperwork or merely get from one day to the next without the excellent help of Edla D'Herckens and Beth Siculan. While they are no longer with Applied Mathematics, Judy Piehl and Mo Ormiston provided invaluable help while I knew them. For me at least, their stay was all too brief.

I also want to thank all the students of the department for their support over the many years, fruitful discussions on math, and entertaining discussions on everything else. I have known many of you over the years, and I am glad to have come here. It is difficult to think of a nicer place to have spent the time.

Finally, my thanks my family for all their love and support. I am very lucky to have you. A special thanks to Catherine for her patience, love, and compassion in waiting for me to finish.

Contents

List of Figures

List of Tables

Chapter 1

Introduction

The problem of a liquid droplet spreading on a solid substrate is of significant theoretical and practical interest. This is a free boundary problem where the droplet interface and its contact line need to be determined as part of the solution. The line where a solid substrate and two immiscible fluids (e.g. air and water) come together is called the contact line. Surface tension and the boundary conditions at the contact line drive the spreading of the droplet. This spreading problem has generated considerable interest lately and there are several review articles that discuss the difficulties encountered in this type of problem; see, e.g., Dussan V.[21], Davis[15], de Gennes[16], Oron *et al.*[64], and Miksis[61]. In this work, a lubrication approximation is applied to study the spreading of a thin liquid drop. The first case examined is a two-dimensional drop with an insoluble surfactant along its surface and both thermal and surface energy gradients along the substrate. We then extend these results to the case of a three-dimensional axisymmetric droplet with surfactant but without thermal or surface energy gradients. Finally, we develop a full three-dimensional formulation that allows us to explore the spreading of a drop on an inclined plane.

Surfactant has many applications in medicine and industry. Gaver and Grotberg[30, 31] studied how surfactant is transported on mucus films, with applications to the lungs, with some recent investigations performed by Craster and Matar[13], Matar[57], and Matar *et al.*[58]. Premature infants frequently have underdeveloped lungs which do not have the proper surfactant coatings. Surfactant replacement therapy aims to coat the air sacs in the lungs with artificial surfactant in an effort to keep them from collapsing. Another use of surfactants is as a medication delivery technique. The medicine piggybacks onto an aerosol spray that enters the lungs. Chabinyc *et al.*[9] present a method for making thin-film transistors (TFTs)

by using surfactants coated liquids to selectively dewet a patterned substrate. Other applications include using surfactants as detergents on droplets of liquid, breaking apart and dispersing oil droplets from an oil spill, and emulsifiers, which help stabilize a mixture of two immiscible liquids by binding to droplets of one liquid and keep it dispersed in the other liquid. Surfactants can also be considered contaminants whose effects must be minimized. In this view, it is important to understand how different the properties of the droplet's spreading will be when clean versus when contaminated.

A more recent application that involves surfactants is microfluidics. The field of microfluidics, where the length scales may be measured in microns, has begun to investigate the addition of surfactants into this difficult submillimeter scale. Gallardo *et al.*[28] used electrodes to dynamically adjust the surface tension gradients caused by surfactants. These redox-active surfactants were able to be manipulated into forcing the liquid into predetermined shapes. Grunze[36] predicted that this line of research and similar work by Gau *et al.*[29] will eventually result in a "laboratory on a chip" where liquids are actively shuttled around the surface of a microchip.

Although the classically accepted boundary condition along the droplet-substrate boundary is no-slip, when it is applied in a moving contact line problem, a nonintegrable stress singularity occurs. Dussan V. and Davis[23] examined the flow of a two-dimensional fluid-fluid interface moving down a solid surface. They found that the velocity field at the contact line is multi-valued and discontinuous, which, for Newtonian fluids, leads to one of the fluids exerting infinite forces on the substrate at the contact line. They showed that these problems existed in the model and were not due to the lack of exact solutions. Any amount of slip was found to eliminate the multivaluedness of fluid velocity and thus the infinite forces. Huh and Scriven[46] had previously found a singularity in the contact line when using the Stokes flow approximation, but were unable to determine either the nature of cause of the singularity. They imposed many assumptions on the interface, including requiring that it be perfectly flat, which prevented them from applying the normal stress boundary condition.

One method proposed to remove this singularity is to allow for slip near the contact line. Dussan V. and Davis [23] showed that any form of slip at the contact

line will eliminate the singularity. Here we will use a Navier slip condition of the form

$$\vec{u} \cdot \hat{t} = \lambda \, \mu \, \hat{n} \cdot \boldsymbol{S} \cdot \hat{t} \tag{1.1}$$

where $\vec{u}$ is velocity vector, $\hat{n}$ and $\hat{t}$ are the unit normal and tangential vectors on the fluid-solid interface, λ is the constant slip coefficient, and $\mu \boldsymbol{S}$ is the viscous stress tensor. This slip model provides that the slip is proportional to the shear stress on the substrate. The slip parameter λ is taken to be numerically small so that away from the contact line, where shear stresses are small, the slip model effectively enforces the no-slip constraint. Hocking[39] performed an asymptotic analysis of this slip model for a moving contact line in a low Reynolds number flow, including flow between parallel plates and flow through a pipe, and found that, as indicated by Dussan V. and Davis[23], the stresses remain finite. We will follow the example of Greenspan[35] and others and allow the slip parameter to vary with the thickness of the droplet. Haley and Miksis[37] compared three-dimensional axisymmetric droplets spreading with different slip models. They used the Navier slip condition with constant slip and with the slip depending on the thickness of the interface as either $1/h$ or $1/h^2$. They found no qualitative differences in the resulting droplet motion.

The Navier slip condition in (1.1) is not the only method to relieve the stress. For example, Huh and Mason[45] proposed a model that allowed the fluid to slip freely (no shear stress) in the neighborhood of the contact line but imposed a no-slip condition away from the contact line. There have also been generalizations of (1.1). For example, Thompson and Troian[80] have used molecular dynamics simulations to formulate an alternate relationship. This new formulation relates the amount of slip to the physical properties of the substrate. At present, the correctness of any one slip condition has not been proved. Although we use the Navier slip condition, our numerical scheme could be easily adapted for alternative conditions.

To surmount the difficulties with choosing a slip condition, it is possible to formulate the problem to eliminate the contact line entirely. A thin precursor film may be extended from the droplet to cover the substrate, eliminating a physical contact line[16]. While this model requires the precursor film to coat the entire substrate, thus being of infinite length, it succeeds in relieving the stress singularity at the contact line since a contact line does not actually exist in this model (see e.g. de Gennes[16]).

In some of these models the precursor film is just a liquid film significantly thinner than the droplet; in other studies additional physics, e.g. Van der Waals forces, are added into the models. Diez *et al.*[19] compare the slip model to the precursor model (without Van der Waals forces) and show that they both display similar behavior.

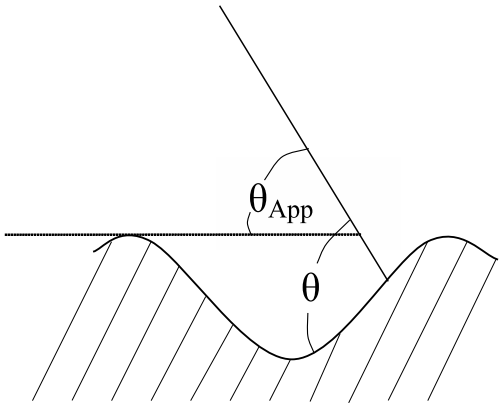

Figure 1.1: Actual versus apparent contact angles

Studies of contact lines invariably involve questions about the angle the interface makes with the underlying substrate, denoted θ. Any macroscopic analysis of the contact line reveals an apparent contact angle, θ_{App}. Unfortunately, this observed contact angle is not necessarily the actual contact angle θ. The speed of the apparent contact line has also been found to be related to the apparent contact angle θ_{App}. Although the slip condition relaxes stresses near the contact line, the stress is still quite large there. The interface thus undergoes a rapid change in curvature in the neighborhood of the contact line. Measurements of the contact angle differ when taken from a distance away from the contact line (θ_{App}) from what the angle is in the neighborhood of the contact line (θ). Many experiments have been performed to determine the nature of the contact angle-contact line velocity relationship[26, 70, 44, 10]. A few general features can be gleaned from these experiments. First, the contact angle increases monotonically for a liquid displacing a gas in all but very high Reynolds number regimes[61]. Second, there is a region $[\theta_{Rec}, \theta_{Adv}]$ where the contact line does not move. This phenomenon is called hysteresis and θ_{Rec} is referred to as the receding static contact angle and θ_{Adv} as the advancing static contact angle. Finally, a relationship between contact angle and contact line velocity can be extracted from

the experiments. In the work presented here, we will assume that this functional relation relates the actual slip velocity to the actual contact angle θ. The apparent angle θ_{App} could be thought of as that angle measured from a plane slightly raised above the substrate. The difference between θ and θ_{App} is demonstrated by Fig. 1.1, which shows a zoomed in view of the surface. Here the actual contact angle θ is shown on a surface with heterogeneity. The apparent contact angle θ_{App} is taken as the angle when the surface irregularities are smoothed out into a smooth plane.

In many cases, the contact angle – slip velocity relationship takes the form

$$\frac{U\mu\chi}{\sigma} = \theta^m - \theta_s^m \tag{1.2}$$

where U is the velocity of the contact line, μ is the viscosity of the liquid, χ is a parameter that depends on the nature of the solid-liquid-gas interaction, σ is the surface tension of the liquid, and θ_s is the static contact angle, chosen somewhere within the hysteresis window. Blake and Haynes[6] derived the $m = 1$ model for when $\theta - \theta_s \ll 1$ and it was the model chosen by Greenspan[35] for his initial work with lubrication theory. Tanner[77] and Lelah and Marmur[53] conducted experiments that support the model when $m = 3$. Zhang[84] conducted numerical simulations with a fixed actual contact angle and then attempted to determine the relationship between the contact line velocity and the apparent contact angle. He found that both $m = 1$ and $m = 3$ would fit the data. An alternative model examined by Ehrhard[24] is

$$\frac{U\mu\chi}{\sigma} = (\theta - \theta_s)^m . \tag{1.3}$$

Ehrhard examined this model for the case when $m = 3$. This relationship has been used by a number of investigators, including Ehrhard and Davis[25] and Anderson and Davis[2]. Haley and Miksis[37] studied this model for the cases of $m = 1, 2, 3$ and found no qualitative difference in the resulting spreading behavior. Hocking[42] has studied the case when $\chi \to 0$, which results in a constant contact angle. Relations of this form have been used by Greenspan[35], Ehrhard and Davis[25], Haley and Miksis[37], and Miksis[61] and will be used in this work.

To simplify the problem from the full Navier-Stokes equations, we apply a lubrication approximation. This model assumes that the droplet's height is much smaller than its radius. Greenspan[35] first used this assumption and derived a first

order in time, fourth order in space partial differential equation for the evolution of surface of a three-dimensional axisymmetric drop. Hocking[41] used the lubrication approximation to study droplets sliding and spreading down an inclined plane, although only for very small gravitational forces. Haley and Miksis[37], Ehrhard and Davis[25], and López *et al.*[56] have all extended this lubrication model in new directions.

The spreading of a nonisothermal drop with a contact line was studied by Ehrhard and Davis[25]. They used the lubrication approximation and assumed small capillary numbers but included a heated substrate. One of their results, which we shall return to later, was that heating could prevent a wetting droplet (zero advancing static contact angle) from continually spreading; it will only spread a finite distance. This model was extended to study nonuniform heating along a substrate by Smith[72], Benintendi and Smith[4], and Smith *et al.*[73]. These ideas will be extended here to consider a droplet moving along a nonuniformly heated substrate with a constant temperature gradient. This temperature gradient creates a thermocapillary-induced flow in the droplet that affects spreading. The effects of evaporation are neglected, but could be included by paralleling the model of Anderson and Davis[2].

The droplet dynamics change significantly when the substrate is inclined. A droplet that lies on a solid inclined plane is affected by two main forces, surface tension and gravity. Surface tension can be related to the contact angle, θ, resulting in a balance of forces in the neighborhood of the contact line. Gravity acts as a nonuniform force to pull the droplet down the plane. The fluid flows toward the front of the droplet, causing the contact angle to increase above the static angle, which drives spreading. By this analysis, any inclination of the plane will result in motion of the droplet.

Providing a nonzero hysteresis window allows the droplet to remain stationary on an inclined plane[5, 27]. In this case, the contact angle is able to steepen, allowing surface tension to balance the gravitational force. As long as the flow of fluid does not cause the rear of the droplet to drop below the hysteresis window, the droplet may remain stationary. The important consideration here is the ratio of the gravitational force to the surface tension force. This ratio is given by $B\sin(\alpha)$, where B is the Bond number and α is the angle of inclination. If this value is too large then

the droplet will not be able to remain stationary and will continue to travel down the plane. When gravity exerts a relatively small force on the droplet, in comparison to surface tension, it translates down the plane at a constant speed while maintaining its shape. Kim *et al.*[49] studied this sliding velocity using both analytics and experiments. They use a similar method to de Gennes[16] wherein they compare the gravitational potential energy with the energy dissipation of the sliding droplet. The droplet should be steadily sliding when these two functions are equal.

At higher forcing, however, the droplet rapidly travels down the substrate and deforms as it moves. It may either radically deform and rupture or else it may continue traveling in an unsteady configuration. In this latter case the droplet becomes elongated and develops a cusp in the rear. Fast moving but hydrophobic ($\theta_{Adv} \sim 180°$) drops were studied by Podgorski *et al.*[66], who described the "pearling" behavior of these drops, whereby they emit smaller drops from the tail of the cusp. This corner singularity and pearling behavior has been studied extensively. Asymptotic analysis of the cusp formation has been performed by Stone *et al.*[76], Roura and Fort[69], and Amar *et al.*[1]. Thiele *et al.*[79] briefly examined the cusp phenomenon using numerical calculations, and it is in this direction that we will go with our studies.

The stability of droplets on inclined planes has been investigated by a number of authors. Troian *et al.*[82] studied the linear stability of the leading edge of a thin fluid sheet using the precursor film model. López *et al.*[55] found the steady state profiles for nonisothermal drops and showed that a constant slip model produces instabilities for droplets on inclined planes. Analysis of the instabilities involved in the spreading of fluids has been conducted by Hocking[40], who noted the ridge that formed near the leading edge of the droplet. Hocking and Miksis[43] followed up this research with further numerical analysis of the ridge model. Thiele and Knobloch[78] examined the stability of a thin film of finite length. By choosing a finite size for their film, they are able to examine the stability at both the front and rear contact lines.

Diez and Kondic[17] investigated the flow of wetting films flowing down inclined planes under the lubrication approximation. They used a thin precursor film model to relax the contact line singularity and initialized their fluid to a traveling wave solution. Marching forward in time, they found that the inclination angle affects the shapes of the instability patterns. While the shapes differed at different inclination

angles, they did not affect the coating behavior of the fluid, implying that any wetting fluid would completely cover the surface. They have followed up this research by investigating the stability of other flows, including heterogeneous substrates[18] where they adjusted the thickness of the precursor film to achieve good agreement with experiments. They then perturb the precursor film thickness to model heterogeneities in the substrate. The heterogeneous surfaces produce fluid patterns similar to those created via front instabilities when the front is slightly perturbed. Similar work was performed by González *et al.*[33], who studied, both experimentally and numerically, the spreading of a thin two-dimensional film down a vertical plate. The thickness of the thin precursor region is measured experimentally and linked to their numerical method, helping to ensure a high quantitative correlation between the two. Gomba *et al.*[32] extended previous experiments into the micrometric range, examining the flow of small quantity of silicon oil down a vertical plane.

Our work extends nonisothermal droplets to include surfactant effects. Surfactants are amphiphilic molecules that lower the surface tension of a liquid interface. In such molecules one end contains a hydrophilic group while the rest of the molecule is hydrophobic. Because of this structure, they typically sit on the surface of the liquid, hence the term surface active agent from which the contraction surfactant is formed. Surfactant gradients create surface tension gradients which, in turn, affect the droplet spreading. As the droplet spreads, the surfactants move along its surface through advection and diffusion, creating a coupled surfactant-droplet system. Surfactants lower surface tension by adsorbing at the interface. Surfactants can be categorized as soluble or insoluble depending on whether they are absorbed into the bulk of the liquid or remain on the interface. We will be limiting our work to insoluble surfactants.

There have been many prior studies that examine surfactants spreading on thin films. Borgas and Grotberg[7] studied the two-dimensional behavior of a droplet coated with insoluble surfactants that is spreading on a thin film. Their model neglected gravity and horizontal pressure gradients. They constructed asymptotic equations that governed the spread of a monolayer of surfactant along the thin film, while moving with the steadily translating frame so the motion appeared steady. Surface diffusivity was found to prevent discontinuities at the leading edge of the

surfactant monolayer, as it instantly spreads to cover the entire thin film. Gaver and Grotberg[30] extended the work of Borgas and Grotberg by including gravity and computing numerical solutions to the coupled fluid-surfactant equations for thin films, i.e., the lubrication approximation. They moved the droplet from a thin film onto a solid substrate. Using a thin precursor model allowed them to look at a three-dimensional axisymmetric droplet configuration. Small Peclet numbers were found to result in surfactant spreading primarily by diffusion, while convection takes over for larger Peclet numbers. Very large Peclet numbers allowed large disturbances in surfactant concentrations. This method was used to verify experimental results by Gaver and Grotberg[31] for dilute concentrations of oleic acid on glycerin.

Jensen and Grotberg[47] studied soluble surfactants where the surfactant diffuses rapidly across the fluid layer. They used the thin-precursor film model and lubrication theory to analyze the two-dimensional spreading of the thin film droplet. They found the transport rates are not significantly affected by the solubility of the surfactant. The absorption of surfactant by the bulk of the fluid reduces surfactant gradients, decreasing the spreading rates for small times. At longer times, however, when the concentration of the surfactant monolayer and bulk have equilibrated locally, then the spreading of the surfactant monolayer can drive clean fluid before it, creating a narrow pulse of raised fluid just before the approaching surfactant.

Matar[57] took a slightly different approach when studying soluble surfactants. He constructed a one-dimensional nonlinear model for surfactant transport in both slow, large Peclet number, and fast, small Peclet number, diffusion cases. Rapid diffusion allowed him to use a cross-sectionally averaged concentration for the surfactant in the bulk. He then used numerical solutions and linear stability analyses to determine the effects that aid and retard rupture. For the rapid diffusion model, he found that increased Marangoni forces and surface viscosity help to retard rupture, while surfactant solubility and the rate of the sorption kinetics help to promote rupture. He and Ketterson[38] experimentally studied the spreading of water covered by a surfactant monolayer on a vertical glass slide. They found that the front of the water film was highly unstable and that the rate of spreading was linearly proportional to the surfactant surface pressure.

Palmer and Berg[65] performed an early study on the stability of a shallow

pool of liquid containing dissolved surfactant that is being heated from below. Their linear stability analysis showed that even mildly active surfactants had a strong influence on the fluid. As other authors have also determined, the transport mechanism for the surfactant is quite important, with diffusion and advection providing different behaviors. They found that large surfactant gradients help stabilize the droplet. Kumar and Matar[52] studied the stability of gravity-modulated (vibrating) thin films coated with insoluble surfactant. They used the lubrication approximation and Floquet theory to determine that long-wave disturbances are destabilized by gravity modulation, but only when surfactants are present on the fluid. Without surfactants, such disturbances are stable on clean fluids. Fingering instabilities of surfactant spreading on a thin film were analyzed by Matar and Troian[59, 60]. They found that the insoluble surfactant was responsible for the fingering instabilities, which result in the spreading film being sensitive to small disturbances in the film height or surfactant distribution.

Borhan and Mao[8] modeled a surfactant coated droplet moving through a circular tube at low Reynolds numbers. In this formulation the droplet never touches the edge of the tube and thus lacks a triple-line. They found that large Peclet numbers, by producing Marangoni stresses that oppose droplet motion, require increased pressure to move the droplet through the tube. Similarly, small Peclet numbers, by uniformly reducing the surface tension, can reduce the pressure needed to move the droplet. An analysis of a surfactant-laden drop falling through a low Reynolds number flow was performed by Johnson and Borhan[48]. As with the Borhan and Mao work, this, too, lacks a triple-line. They found that surfactants had a destabilizing effect on spreading droplets. The presence of surfactants caused more extreme deformation of the droplet, similar to the effects of an increased Bond number, preventing the falling droplet from achieving a steady state. Soluble surfactants were found to be more stable than insoluble surfactants, requiring a higher Bond number to cause breakup.

If surfactant can absorb and desorb from the substrate, then the local value of the surface tension can influence the dynamics of the droplet; this situation will be considered here. This transfer of surfactant has been investigated by Ramé[68], following the approach of Cox[12]. The full dynamics of a droplet were not considered, only the motion near a single contact line. He experienced much difficulty in relieving

the contact line singularity when flux is permitted, something that we, too, will deal with. Here we will study how insoluble surfactant effects can influence the dynamics of a spreading droplet in the thin film limit.

Chengara *et al.*[11] put forward the idea that the initial rapid spreading of surfactant coated droplets is due to the high surface tension gradients formed by the local loss of surfactant when the droplet spreads. As the drop spreads, the surfactant concentration is locally lowered, creating large surfactant gradients, which reinforce the spreading. Their conclusion is that contact line motion did not affect the initial spreading of droplets; the driving force for their surfactant solution on hydrophobic surface is the surface tension gradient that forms at the air-solution boundary.

Milliken *et al.*[62], extending the work of Stone and Leal[75], explored how insoluble surfactants can allow greater deformation of droplets. They found that surfactants have the greatest effect on the steady behavior of drops when the viscosity ratio between the drop and the surrounding fluid is small. They also showed that large surfactant gradients retard droplet spreading, a phenomenon to which we will be returning. They also analyzed the effects of surfactants on elongating droplets. In this configuration, surfactants change the time scale of the capillary waves, slowing the onset of the waves and producing growth modes along the entire length of the droplet.

In this thesis, we will formulate a lubrication approximation to the full Navier-Stokes equations for the motion of a droplet. In chapter 2, we formulate the problem for two-dimensional spreading droplets coated with insoluble surfactants and affected by thermal and surface energy gradients on the substrates. We describe our numerical method, which uses pseudo-spectral derivatives to solve a set of non-linear equations in chapter 3. The results of our two-dimensional investigations are presented in chapter 4; we explore the general behavior of surfactant coated droplets and also examine how surface energy gradients and temperature gradients can be used to propel a droplet along the surface. We then extend the surfactant coated droplet model into three dimensions, constructing an axisymmetric model in Chapter 5. In this chapter, temperature and surface energy gradients are not considered. In chapters 6–7, we formulate our numerical method and compare the three-dimensional axisymmetric results to the two-dimensional results, finding good agreement between

the two. We then move on to three-dimensions, where, in chapters 8–10, we go back and reformulate equations for three-dimensions and examine the spreading of a droplet as it slides down an inclined plane. While we do not include surfactant effects in the full three-dimensional model, we are able to compare our results to other researchers' predictions for spreading rates. We also look into the transition of a droplet from being stationary on the inclined plane, through a steadily translating regime, and finally to the limits of our model where the droplet catastrophically deforms.

Chapter 2

Two-Dimensional Problem Formulation

The spreading of an incompressible Newtonian liquid droplet on a flat substrate is considered. The droplet is bounded above by a passive gas while the substrate below may have a nonuniform temperature gradient applied to it. In this two-dimensional analysis we will apply a lubrication approximation to the equations of motion to consider the spreading of the droplet and the translational effects of the nonuniform temperature gradient. We will also consider the case where the substrate has been doped with surfactant, which acts as a surface energy gradient, causing the droplet to translate along the substrate.

2.1 Problem Formulation

Let x be the horizontal variable and y be the vertical variable. The distance from the substrate the free surface is denoted $h(r,t)$ and $R(t)$ and $L(t)$ are the positions of the right and left contact lines of the drop, which makes angles θ_R and θ_L with the substrate (see Fig. 2.1). The horizontal and vertical components of velocity are given by u and v, respectively. Finally, gravity, g, acts in the negative y direction.

We are interested in the following equations in the bulk of the fluid: conservation of mass,

$$\frac{\partial u}{\partial x} + \frac{\partial v}{\partial y} = 0, \tag{2.1}$$

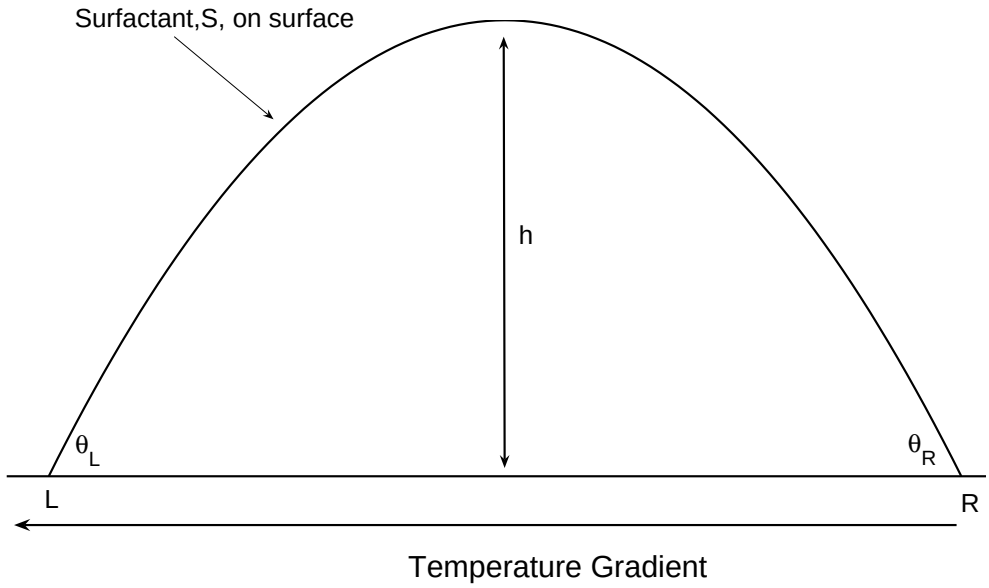

Figure 2.1: Two-dimensional droplet configuration

and conservation of momentum in horizontal, x, and vertical, y, directions,

$$\rho\left(\frac{\partial u}{\partial t}+u\frac{\partial u}{\partial x}+v\frac{\partial u}{\partial y}\right)=\mu\nabla^2 u-\frac{\partial p}{\partial x}, \tag{2.2}$$

$$\rho\left(\frac{\partial v}{\partial t}+u\frac{\partial v}{\partial x}+v\frac{\partial v}{\partial y}\right)=\mu\nabla^2 v-\frac{\partial p}{\partial y}-\rho g, \tag{2.3}$$

where p is the pressure in the drop, ρ is the density of drop's fluid, and μ is the viscosity of the drop. At $y=0$, the conditions are no penetration,

$$v=0, \tag{2.4}$$

and, in order to relax the no-slip condition and relieve the singularity at the contact line (see e.g. Dussan V. and Davis[23]), the Navier slip condition

$$u-\lambda(h)\left(\frac{\partial u}{\partial y}+\frac{\partial v}{\partial x}\right)=0. \tag{2.5}$$

The slip condition is (1.1) evaluated for our two-dimensional coordinates. The slip function is given by

$$\lambda(h)=\frac{\lambda_n}{h^n}. \tag{2.6}$$

The $n = 1$ case was first introduced by Greenspan[35]. This slip function has been studied by Haley and Miksis[37] who found no qualitative differences for $n = 0, 1, 2$. For our analysis, it is assumed that $n = 0$. At the free boundary, $y = h(x,t)$, the governing equations are the kinematic condition

$$\frac{\partial h}{\partial t} + u\frac{\partial h}{\partial x} - v = 0, \tag{2.7}$$

and the jump in normal stress condition

$$p = p_A - \sigma\frac{\partial}{\partial x}\left\{\frac{\partial h}{\partial x}\left[1 + \left(\frac{\partial h}{\partial x}\right)^2\right]^{-\frac{1}{2}}\right\} + 2\mu\left[1 + \left(\frac{\partial h}{\partial x}\right)^{-1}\right]\left[\left(\frac{\partial h}{\partial x}\right)^2\frac{\partial u}{\partial x} - \frac{\partial h}{\partial x}\left(\frac{\partial u}{\partial y} + \frac{\partial v}{\partial x}\right) + \frac{\partial v}{\partial y}\right]. \tag{2.8}$$

Note that here we have assumed that the interface can be written as a function of x. Here p_A is the atmospheric pressure of the surrounding fluid and σ is the surface tension of the droplet. The other condition at the free surface boundary is the continuity of tangential stress condition. The general stress condition along the interface is

$$\hat{n}\cdot\boldsymbol{\tau} = -\sigma\left(\nabla_s\cdot\hat{n}\right)\hat{n} + \nabla_s\sigma \tag{2.9}$$

where the unit normal is

$$\hat{n} = \frac{<-h_x, 1>}{\sqrt{1+h_x^2}}, \tag{2.10}$$

the unit tangent is

$$\hat{t} = \frac{<1, h_x>}{\sqrt{1+h_x^2}}, \tag{2.11}$$

the stress tensor is

$$\tau_{ij} = -p\delta_{ij} + \mu e_{ij}, \tag{2.12}$$

and ∇_s is the surface derivative in the direction of the tangent. The gradient is given by[51]

$$\nabla_s f = \frac{<1, h_x>}{1+(h_x)^2}\frac{\partial f}{\partial x}. \tag{2.13}$$

Now $\hat{t}$ can be dotted into (2.9) to pick out the continuity of tangential stress condition,

$$\hat{n}\cdot\boldsymbol{\tau}\cdot\hat{t} = -\sigma\left(\nabla_s\cdot\hat{n}\right)\hat{n}\cdot\hat{t} + \nabla_s\sigma\cdot\hat{t}. \tag{2.14}$$

Canceling terms leaves:

$$\hat{n} \cdot \boldsymbol{\tau} \cdot \hat{t} = \nabla_s \sigma \cdot \hat{t}. \tag{2.15}$$

Expanding each side of (2.15) gives us:

$$\begin{aligned}
\hat{n} \cdot \boldsymbol{\tau} \cdot \hat{t} &= n_x \tau_{xx} t_x + n_x \tau_{xy} t_y + n_y \tau_{yx} t_x + n_y \tau_{yy} t_y \\
&= \frac{1}{1 + (\frac{\partial h}{\partial x})^2} \Bigg[- \frac{\partial h}{\partial x} \left(-p + \mu \frac{\partial u}{\partial x} \right) - \frac{\partial h}{\partial x} \frac{\mu}{2} \left(\frac{\partial u}{\partial y} + \frac{\partial v}{\partial x} \right) \frac{\partial h}{\partial x} \\
&\quad + \frac{\mu}{2} \left(\frac{\partial u}{\partial y} + \frac{\partial v}{\partial x} \right) + \left(-p + \mu \frac{\partial v}{\partial x} \right) \frac{\partial h}{\partial x} \Bigg] \\
&= \frac{\mu}{1 + (\frac{\partial h}{\partial x})^2} \left[\frac{\partial h}{\partial x} \left(\frac{\partial v}{\partial y} - \frac{\partial u}{\partial x} \right) + \frac{1}{2} \left(1 - \left(\frac{\partial h}{\partial x} \right)^2 \right) \left(\frac{\partial u}{\partial y} + \frac{\partial v}{\partial x} \right) \right] \\
= \nabla_s \sigma \cdot \hat{t} &= \frac{1}{\sqrt{\left(1 + \left(\frac{\partial h}{\partial x} \right)^2 \right)}} \frac{\partial \sigma}{\partial x}.
\end{aligned} \tag{2.16}$$

Now simplifying (2.16) produces the continuity of tangential stress condition:

$$\mu \left\{ \frac{\partial h}{\partial x} \left(\frac{\partial v}{\partial y} - \frac{\partial u}{\partial x} \right) + \frac{1}{2} \left[1 - \left(\frac{\partial h}{\partial x} \right)^2 \right] \left(\frac{\partial u}{\partial y} + \frac{\partial v}{\partial x} \right) \right\} = \sqrt{1 + \left(\frac{\partial h}{\partial x} \right)^2} \frac{\partial \sigma}{\partial x}. \tag{2.17}$$

Boundary conditions at the contact line are still needed. The slip velocity is defined to be the velocity of the contact line. Recalling the discussion in the previous chapter, here we set the slip velocities equal to a general function of the contact angle. The result is our contact angle – slip velocity relationship:

$$u_s \Big|_{x=L} = \frac{dL}{dt} \tag{2.18}$$

$$= f(\theta_L), \tag{2.19}$$

$$u_s \Big|_{x=R} = \frac{dR}{dt} \tag{2.20}$$

$$= f(\theta_R). \tag{2.21}$$

We will be using a contact angle – slip velocity relationship that includes hysteresis effects:

$$f(\theta) = \hat{k} \begin{cases} (\theta - \theta_{Adv}), & \theta > \theta_{Adv} \\ 0, & \theta_{Rec} \leq \theta \leq \theta_{Adv} \\ (\theta - \theta_{Rec}), & \theta < \theta_{Rec}. \end{cases} \tag{2.22}$$

Here $\hat{k}$ is a characteristic unit of velocity. This is the $m = 1$ form of (1.2)–(1.3) extended to allow for hysteresis. It has been used by, among others, Greenspan[35] and Haley and Miksis[37].

Another boundary condition results from the fact that the droplet must remain in contact with the surface at the contact points, so

$$h(L(t), t) = 0, \tag{2.23a}$$

$$h(R(t), t) = 0. \tag{2.23b}$$

Finally, geometric analysis shows that

$$\left.\frac{\partial h}{\partial x}\right|_{x=L(t)} = \tan(\theta_L), \tag{2.24a}$$

$$\left.\frac{\partial h}{\partial x}\right|_{x=R(t)} = -\tan(\theta_R). \tag{2.24b}$$

This basic model can now be generalized to include the effects of a nonuniformly heated substrate. Suppose that the droplet is bounded above by a passive gas at temperature T_∞, and that there is a fixed, linear temperature gradient along the substrate. A similar situation was considered by Smith[72]. The temperature in the droplet is given by $T(x, y, t)$. The energy equation, which governs heat transfer within the droplet, is

$$\rho\, c \left(\frac{\partial T}{\partial t} + \vec{v} \cdot \nabla T \right) = k \nabla^2 T, \tag{2.25}$$

with c being the specific heat of the liquid, k the thermal conductivity of the droplet, and $\vec{v}$ being the full velocity vector: $\vec{v} =< u, v >$. The energy balance on the surface of the droplet, $y = h$, is given by

$$-k \nabla T \cdot \hat{n} = h_g \left(T - T_\infty \right) \tag{2.26}$$

with h_g being the convection heat transfer coefficient for the free survace. Also assume that there is a fixed-temperature-gradient along the substrate surface, $y = 0$, given by:

$$T = T_0 - b\, x, \tag{2.27}$$

where $b = -dT/dx$ is the imposed temperature gradient and T_0, the temperature of the substrate at $x = 0$, is a prescribed value.

The final main component of our model is the inclusion of surfactants. This can be done by introducing a surfactant transport equation along the interface. Assume that the concentration of surfactant on the surface of the droplet is given by $S(x,t)$. The general surfactant transport equation is

$$S_t + \nabla_s \cdot (\vec{u}_s S) - (\nabla_s \cdot \hat{n})\, S\, (\vec{u} \cdot \hat{n}) = D\nabla_s^2 S + J \tag{2.28}$$

where D is the surface diffusivity constant, $\vec{u}_s$ is the surface velocity (velocity in the tangential direction), $\hat{n}$ is the unit normal vector to the surface, and J is the surface absorption term, which is ignored for this analysis[74]. In (2.28), the surface divergence is given by

$$\nabla_s \cdot (\vec{u}_s S) = \frac{1 + h_x}{\sqrt{1 + (h_x)^2}} \frac{\partial}{\partial x} (u_s S) \tag{2.29}$$

where

$$u_s = \vec{v} \cdot \hat{t}. \tag{2.30}$$

Surfactant will be allowed to be adsorbed and desorbed at the contact line. This is done by assuming that the gradient of S is linearly related to the surfactant concentration at the contact point. In particular, the boundary conditions for surfactant transport are given by

$$\left.\frac{\partial S}{\partial x}\right|_{x=L(t)} = S_T \sqrt{1 + \left(\frac{\partial h}{\partial x}\right)^2} \left(S\big|_{x=L(t)} - S_S\right), \tag{2.31a}$$

$$\left.\frac{\partial S}{\partial x}\right|_{x=R(t)} = -S_T \sqrt{1 + \left(\frac{\partial h}{\partial x}\right)^2} \left(S\big|_{x=R(t)} - S_S\right), \tag{2.31b}$$

where S_T is the transfer rate of surfactant onto and off of the substrate, S_S is the steady concentration of surfactant on the substrate. It is assumed that S_T and S_S are constants independent of time. By assuming that these remain constant, it is implied that if surfactant were absorbed by the advancing contact line, the resulting surface surfactant concentration would not affect the receding contact line if it were to transverse the same point twice on the substrate. No-flux at the contact lines can be modeled by taking $S_T = 0$. Equation (2.31) is clearly a modeling assumption on our part, but it appears to be reasonable since the surfactant flux might be expected to increase as the local value of surfactant concentration increases.

We will also need an equation of state, which we take to be

$$\sigma = 1 + \epsilon^2 \Sigma \tag{2.32}$$

where $\epsilon \ll 1$ and Σ is given by

$$\Sigma = -\sigma_T (T - T_0) - \sigma_S S. \tag{2.33}$$

Here σ_T is a constant having units of J/m^2K that represents how strongly temperature affects surface tension while σ_S represents how strongly surfactants affect surface tension and has units of $J/mol\ m$.

Finally, the volume of the fluid droplet and the amount of surfactant on it are both constant in time and can be represented as

$$V_F = \int_{L(t)}^{R(t)} h(x,t)dx, \tag{2.34}$$

$$V_S = \int_{L(t)}^{R(t)} \sqrt{1 + \left(\frac{\partial h}{\partial x}\right)^2}\, S(x,t)dx. \tag{2.35}$$

Equations (2.1)–(2.31) are the full nonlinear model for the motion of a droplet with both thermal and surfactant effects.

2.2 Nondimensionalization

Here we will nondimensionalize the evolution equations. The basic assumption of lubrication theory is that the height of the droplet is much less than its width along the substrate. This assumption will be used to scale the nondimensional variables. The lubrication relationship also implies that the contact angle is small. The dimensional contact angle θ is used to define our small parameter $\epsilon \ll 1$. This parameter is used to scale our nondimensional variables, denoted by tildes:

$$
\begin{aligned}
t &= \frac{\tilde{t} R_c \mu}{\sigma_c \epsilon^3}, & x &= \tilde{x} R_c, & y &= \tilde{y} R_c \epsilon, \\
u &= \tilde{u} \hat{k} \epsilon, & v &= \tilde{v} \hat{k} \epsilon^2, & \theta_R &= \tilde{\theta}_R \epsilon, \\
\theta_L &= \epsilon \tilde{\theta}_L, & \theta_{Adv} &= \epsilon \tilde{\theta}_{Adv}, & \theta_{Rec} &= \epsilon \tilde{\theta}_{Rec}, \\
p &= \frac{\tilde{p} \mu \hat{k}}{R_c \epsilon} + p_A, & R &= \tilde{R} R_c, & L &= \tilde{L} R_C \\
V_F &= \tilde{V}_F 2\pi R_c^3 \epsilon, & \sigma &= \sigma_c \tilde{\sigma}, & h &= \tilde{h} R_c \epsilon \\
V_S &= \tilde{V}_S 2\pi R_c^2 S_c, & \lambda_0 &= \tilde{\lambda}_0 R_c \epsilon, & S &= \tilde{S} S_c, \\
\Sigma &= \sigma_c \tilde{\Sigma}, & S_T &= \tilde{S}_T \frac{R_c}{S_c}, & S_S &= \tilde{S}_S \frac{R_c}{S_c}, \\
f &= \epsilon \hat{k} \tilde{f} & T &= (T_0 - T_\infty)\tilde{T} + T_\infty.
\end{aligned}
$$

Here R_c is taken to be a characteristic length of the droplet, either an initial half width or a steady state half width, for example. The constant σ_c is the surface tension of a clean surface, which occurs when there is no surfactant on the droplet and the substrate is kept isothermal. The constant S_c is a characteristic surfactant concentration. We choose y to be one order of magnitude in ϵ smaller than x since that is consistent with the lubrication approximation that the height of droplet is much less than its width. Scalings for the velocities are chosen by examining the contact angle – slip velocity relationship (2.22) when substituted into (2.19) and (2.21). This gives a scaling for u and, because of (2.1), the vertical direction v is again chosen to be one order of magnitude smaller.

Also introduce the Capillary number, Ca, the Bond number, B, the Reynolds number, Re, the Peclet number, Pe, the Biot number, Bi, the Prandtl number, Pr, the Marangoni numbers for surfactant and temperature effects, M_S and M_T, the parameter δ representing the strength of the effect of temperature on surface tension, the parameter β representing the strength of the surfactant gradient, and

the parameter N is the prescribed temperature gradient:

$$Ca = \frac{\mu\hat{k}}{\sigma_c\epsilon^2}, \qquad B = \frac{\rho g R_c^2}{\sigma_c}, \qquad Re = \frac{\rho R_c \hat{k}}{\mu},$$
$$Pe = \frac{R_c\hat{k}\epsilon}{D}, \qquad Pr = \frac{\epsilon\mu c_p}{k}, \qquad Bi = \frac{\epsilon h_g R_c}{k},$$
$$M_S = \frac{\sigma_c\beta\epsilon^2}{\mu\hat{k}}, \qquad M_T = \frac{\sigma_c\delta\epsilon^2}{\mu\hat{k}}, \qquad \delta = \frac{\sigma_T}{\sigma_c}(T_0 - T_\infty),$$
$$\beta = \frac{S_c\sigma_S}{\sigma_c}, \qquad N = \frac{bR_c}{T_0 - T_\infty}.$$

All of these parameters are assumed to be order one.

Rescaling the conservation of mass equation (2.1) for these new nondimensional variables, we get

$$\frac{\partial\tilde{u}}{\partial\tilde{x}} + \frac{\partial\tilde{v}}{\partial\tilde{y}} = 0. \tag{2.36}$$

Using these scalings and nondimensional parameters in (2.2) gives us

$$Re\,\epsilon^3\left(\frac{1}{Ca}\frac{\partial\tilde{u}}{\partial\tilde{t}} + \tilde{u}\frac{\partial\tilde{u}}{\partial\tilde{x}} + \tilde{v}\frac{\partial\tilde{u}}{\partial\tilde{y}}\right) + \frac{\partial\tilde{p}}{\partial\tilde{x}} = \frac{\partial^2\tilde{u}}{\partial\tilde{y}^2} + \epsilon^2\frac{\partial^2\tilde{u}}{\partial\tilde{x}^2}. \tag{2.37}$$

The conservation of momentum in y equation (2.3) now becomes

$$\frac{\partial\tilde{p}}{\partial\tilde{y}} + \epsilon^5 Re\left(\frac{1}{Ca}\frac{\partial\tilde{v}}{\partial\tilde{t}} + \tilde{u}\frac{\partial\tilde{u}}{\partial\tilde{x}} + \tilde{v}\frac{\partial\tilde{u}}{\partial\tilde{y}}\right) = \epsilon^4\frac{\partial^2\tilde{v}}{\partial\tilde{x}^2} + \epsilon^2\frac{\partial^2\tilde{v}}{\partial\tilde{y}^2} - \frac{B}{Ca}. \tag{2.38}$$

At $\tilde{y} = 0$, the no penetration condition becomes

$$\tilde{v} = 0 \tag{2.39}$$

while the Navier slip law is

$$\tilde{u} - \tilde{\lambda}_0\left(\frac{\partial^2\tilde{u}}{\partial\tilde{y}^2} + \epsilon^2\frac{\partial^2\tilde{v}}{\partial\tilde{x}^2}\right). \tag{2.40}$$

At the boundary of the droplet, $\tilde{y} = \tilde{h}(\tilde{x},\tilde{t})$, the kinematic condition is

$$\frac{1}{Ca}\frac{\partial\tilde{h}}{\partial\tilde{t}} + \tilde{u}\frac{\partial\tilde{h}}{\partial\tilde{x}} - \tilde{v} = 0. \tag{2.41}$$

The jump in normal stress is now

$$\tilde{p} = -\frac{1}{Ca}\frac{\partial}{\partial\tilde{x}}\left[\frac{\frac{\partial\tilde{h}}{\partial\tilde{x}}}{\sqrt{1+\epsilon^2\left(\frac{\partial\tilde{h}}{\partial\tilde{x}}\right)^2}}\right] + \frac{2\epsilon^2}{1+\epsilon^2\left(\frac{\partial\tilde{h}}{\partial\tilde{x}}\right)^2}\left\{\frac{\partial\tilde{v}}{\partial\tilde{y}} - \frac{\partial\tilde{h}}{\partial\tilde{x}}\frac{\partial\tilde{u}}{\partial\tilde{y}} + \epsilon^2\left[\frac{\partial\tilde{u}}{\partial\tilde{x}}\left(\frac{\partial\tilde{h}}{\partial\tilde{x}}\right)^2 - \frac{\partial\tilde{h}}{\partial\tilde{x}}\frac{\partial\tilde{v}}{\partial\tilde{x}}\right]\right\}. \tag{2.42}$$

The equation of state will be used in the continuity of tangential stress condition, so we will nondimensionalize it first:

$$\tilde{\Sigma} = -\delta\left(\tilde{T} - 1\right) - \beta\tilde{S}. \tag{2.43}$$

The continuity of tangential stress condition now becomes

$$\epsilon\frac{\partial\tilde{h}}{\partial\tilde{x}}\left(\epsilon\frac{\partial\tilde{v}}{\partial\tilde{y}} - \epsilon\frac{\partial\tilde{u}}{\partial\tilde{x}}\right) + \frac{1}{2}\left(1 - \left(\epsilon\frac{\partial\tilde{h}}{\partial\tilde{x}}\right)^2\right)\left(\frac{\partial\tilde{u}}{\partial\tilde{y}} + \epsilon^2\frac{\partial\tilde{v}}{\partial\tilde{x}}\right) = \frac{1}{Ca}\sqrt{1 + \epsilon^2(\frac{\partial\tilde{h}}{\partial\tilde{x}})^2}\frac{\partial\tilde{\Sigma}}{\partial\tilde{x}}. \tag{2.44}$$

At the contact line, combining (2.18)–(2.21), the contact angle – slip velocity relationships become

$$\frac{d\tilde{R}}{d\tilde{t}} = Ca\ \tilde{f}(\tilde{\theta}_R) \tag{2.45a}$$

$$\frac{d\tilde{L}}{d\tilde{t}} = Ca\ \tilde{f}(\tilde{\theta}_L) \tag{2.45b}$$

where

$$\tilde{f}(\tilde{\theta}) = \begin{cases} \left(\tilde{\theta} - \tilde{\theta}_{Adv}\right), & \tilde{\theta} > \tilde{\theta}_{Adv} \\ 0, & \tilde{\theta}_{Rec} \le \tilde{\theta} \le \tilde{\theta}_{Adv} \\ \left(\tilde{\theta} - \tilde{\theta}_{Rec}\right), & \tilde{\theta} < \tilde{\theta}_{Rec} \end{cases} \tag{2.46}$$

The contact conditions remain

$$\tilde{h}(\tilde{R}, \tilde{t}) = 0, \tag{2.47a}$$

$$\tilde{h}(\tilde{L}, \tilde{t}) = 0, \tag{2.47b}$$

and the geometric relationships are

$$\left.\frac{\partial\tilde{h}}{\partial\tilde{x}}\right|_{\tilde{x}=\tilde{R}(\tilde{t})} = -\frac{1}{\epsilon}\tan(\epsilon\tilde{\theta}), \tag{2.48a}$$

$$\left.\frac{\partial\tilde{h}}{\partial\tilde{x}}\right|_{\tilde{x}=\tilde{L}(\tilde{t})} = \frac{1}{\epsilon}\tan(\epsilon\tilde{\theta}). \tag{2.48b}$$

Temperature has been nondimensionalized such that $\tilde{T} = 0$ corresponds to temperature of the gas and $\tilde{T} = 1$ represents the temperature of the substrate at $x = 0$. The energy equation for heat transfer (2.25) becomes

$$RePr\left(\frac{1}{Ca}\frac{\partial\tilde{T}}{\partial\tilde{t}} + \frac{\partial\tilde{T}}{\partial\tilde{x}}\tilde{u} + \frac{\partial\tilde{T}}{\partial\tilde{y}}\tilde{v}\right) = \frac{\partial^2\tilde{T}}{\partial\tilde{x}^2} + \frac{1}{\epsilon^2}\frac{\partial^2\tilde{T}}{\partial\tilde{y}^2}. \tag{2.49}$$

At $\tilde{y} = \tilde{h}$

$$\frac{1}{\sqrt{1+\epsilon^2\left(\frac{\partial \tilde{h}}{\partial \tilde{x}}\right)^2}}\left[\epsilon^2\frac{\partial \tilde{h}}{\partial \tilde{x}}\frac{\partial \tilde{T}}{\partial \tilde{x}} - \frac{\partial T}{\partial y}\right] = Bi\ \tilde{T}. \tag{2.50}$$

At $y = 0$ the boundary condition is now

$$\tilde{T} = 1 - N\tilde{x}. \tag{2.51}$$

The surfactant transport equation (2.28) is more involved and it will be nondimensionalized piecewise. The unit vectors become

$$\hat{n} = \frac{< -\epsilon\frac{\partial \tilde{h}}{\partial \tilde{x}}, 1 >}{\sqrt{1+\left(\epsilon\frac{\partial \tilde{h}}{\partial \tilde{x}}\right)^2}}, \tag{2.52}$$

$$\hat{t} = \frac{< 1, \epsilon\frac{\partial \tilde{h}}{\partial \tilde{x}} >}{\sqrt{1+\left(\epsilon\frac{\partial \tilde{h}}{\partial \tilde{x}}\right)^2}}. \tag{2.53}$$

The surface divergence (2.29) is now

$$\nabla_s \cdot (\vec{u}_s S) = \frac{\epsilon\hat{k}S_c}{R_c}\frac{1}{\sqrt{1+\left(\epsilon\frac{\partial \tilde{h}}{\partial \tilde{x}}\right)^2}}\frac{\partial}{\partial \tilde{x}}\left(\frac{\tilde{u}+\epsilon^2\tilde{v}\frac{\partial \tilde{h}}{\partial \tilde{x}}}{\sqrt{1+\left(\epsilon\frac{\partial \tilde{h}}{\partial \tilde{x}}\right)^2}}\tilde{S}\right). \tag{2.54}$$

The surface Laplacian is given by

$$\nabla_s^2 = \frac{S_c}{R_c^2}\frac{1}{\sqrt{1+\left(\epsilon\frac{\partial \tilde{h}}{\partial \tilde{x}}\right)^2}}\frac{\partial}{\partial \tilde{x}}\left(\frac{1}{\sqrt{1+\left(\epsilon\frac{\partial \tilde{h}}{\partial \tilde{x}}\right)^2}}\frac{\partial \tilde{S}}{\partial \tilde{x}}\right). \tag{2.55}$$

Combining (2.52)–(2.55) allows us to nondimensionalize the surfactant transport

equation (2.28):

$$\frac{1}{Ca}\frac{\partial \tilde{S}}{\partial \tilde{t}} + \frac{1}{\sqrt{1+\left(\epsilon\frac{\partial \tilde{h}}{\partial \tilde{x}}\right)^2}}\frac{\partial}{\partial \tilde{x}}\left(\frac{\tilde{u}+\epsilon^2\tilde{v}\frac{\partial \tilde{h}}{\partial \tilde{x}}}{\sqrt{1+\left(\epsilon\frac{\partial \tilde{h}}{\partial \tilde{x}}\right)^2}}\tilde{S}\right)$$
$$- \frac{1}{1+\left(\epsilon\frac{\partial \tilde{h}}{\partial \tilde{x}}\right)^2}\frac{\partial}{\partial \tilde{x}}\left(\frac{\frac{\partial \tilde{h}}{\partial \tilde{x}}}{\sqrt{1+\left(\epsilon\frac{\partial \tilde{h}}{\partial \tilde{x}}\right)^2}}\right)\tilde{S}\left(-\epsilon\tilde{u}\frac{\partial \tilde{h}}{\partial \tilde{x}}+\epsilon\tilde{v}\right) \tag{2.56}$$
$$= \frac{1}{Pe}\frac{1}{\sqrt{1+\left(\epsilon\frac{\partial \tilde{h}}{\partial \tilde{x}}\right)^2}}\frac{\partial}{\partial \tilde{x}}\left(\frac{1}{\sqrt{1+\left(\epsilon\frac{\partial \tilde{h}}{\partial \tilde{x}}\right)^2}}\frac{\partial \tilde{S}}{\partial \tilde{x}}\right).$$

The surfactant boundary conditions are

$$\left.\frac{\partial \tilde{S}}{\partial \tilde{x}}\right|_{\tilde{x}=\tilde{L}(\tilde{t})} = \tilde{S}_T\sqrt{1+\left(\epsilon\frac{\partial h}{\partial x}\right)^2}\left(\tilde{S}\big|_{\tilde{x}=\tilde{L}(\tilde{t})} - \tilde{S}_S\right), \tag{2.57a}$$

$$\left.\frac{\partial \tilde{S}}{\partial \tilde{x}}\right|_{\tilde{x}=\tilde{R}(\tilde{t})} = -\tilde{S}_T\sqrt{1+\left(\epsilon\frac{\partial h}{\partial x}\right)^2}\left(\tilde{S}\big|_{\tilde{x}=\tilde{R}(\tilde{t})} - \tilde{S}_S\right). \tag{2.57b}$$

Finally, the volume of fluid and amount of surfactant become

$$\tilde{V}_F = \int_{\tilde{L}}^{\tilde{R}} \tilde{h}(\tilde{x},\tilde{t})d\tilde{x}, \tag{2.58}$$

$$\tilde{V}_S = \int_{\tilde{L}}^{\tilde{R}} \sqrt{1+\left(\epsilon\frac{\partial h}{\partial x}\right)^2}\tilde{S}(\tilde{x},\tilde{t})d\tilde{x}. \tag{2.59}$$

2.3 Leading Order Equations

Now that we have derived the nondimensional equations for the system, we can go about finding the leading order in ϵ terms. Introduce a regular perturbation expansion of the form $\tilde{h} = \tilde{h}_0 + \epsilon\tilde{h}_1 + \ldots$ for each of the dependent variables. Substitutes this expansion into equations (2.36)–(2.57) and group together terms of like order in ϵ. At leading order, the conservation of mass equation remains unchanged as

$$\frac{\partial \tilde{u}}{\partial \tilde{x}} + \frac{\partial \tilde{v}}{\partial \tilde{y}} = 0. \tag{2.60}$$

and the conservation of momentum in x becomes

$$\frac{\partial \tilde{p}_0}{\partial \tilde{x}} = \frac{\partial^2 \tilde{u}_0}{\partial \tilde{y}^2}. \tag{2.61}$$

while conservation of momentum in y gives

$$\frac{\partial \tilde{p}_0}{\partial \tilde{y}} = -\frac{B}{Ca}. \tag{2.62}$$

At the substrate $\tilde{y} = 0$, the no penetration condition (2.39) remains unchanged as

$$\tilde{v}_0\Big|_{\tilde{y}=0} = 0. \tag{2.63}$$

The slip law (2.40) becomes

$$\tilde{u}_0 - \tilde{\lambda}_0 \frac{\partial \tilde{u}_0}{\partial \tilde{y}} = 0. \tag{2.64}$$

On the free surface, $\tilde{y} = \tilde{h}(\tilde{x}, \tilde{t})$, the kinematic condition (2.7) reduces to

$$\frac{1}{Ca}\frac{\partial \tilde{h}_0}{\partial \tilde{t}} + \tilde{u}_0 \frac{\partial \tilde{h}_0}{\partial \tilde{x}} - \tilde{v}_0 = 0. \tag{2.65}$$

The continuity of tangential stress condition (2.44) reduces to

$$\frac{\partial \tilde{u}_0}{\partial \tilde{y}} = \frac{2}{Ca}\frac{\partial}{\partial \tilde{x}} \tilde{\Sigma}_0 \left(\tilde{S}_c(\tilde{x}), \tilde{T}_0(\tilde{x}) \right). \tag{2.66}$$

The jump in normal stress (2.42) becomes

$$\tilde{p}_0 = -\frac{1}{Ca}\frac{\partial^2 \tilde{h}_0}{\partial \tilde{x}^2} \tag{2.67}$$

Expanding the geometric relation (2.48) for $\epsilon \ll 1$ produces

$$\frac{\partial \tilde{h}_0}{\partial \tilde{x}}\bigg|_{\tilde{x}=\tilde{R}} = -\tilde{\theta_{R0}} \tag{2.68a}$$

$$\frac{\partial \tilde{h}_0}{\partial \tilde{x}}\bigg|_{\tilde{x}=\tilde{L}} = \tilde{\theta_{L0}} \tag{2.68b}$$

Combining this result with (2.45) yields

$$\frac{1}{Ca}\frac{d\tilde{R}_0}{d\tilde{t}} = \tilde{f}\left(-\frac{\partial \tilde{h}_0}{\partial \tilde{x}}\bigg|_{\tilde{x}=\tilde{R}} \right), \tag{2.69a}$$

$$\frac{1}{Ca}\frac{d\tilde{L}_0}{d\tilde{t}} = \tilde{f}\left(\frac{\partial \tilde{h}_0}{\partial \tilde{x}}\bigg|_{\tilde{x}=\tilde{L}} \right). \tag{2.69b}$$

At leading order, the energy equation for heat transfer becomes

$$\frac{\partial^2 \tilde{T}_0}{\partial \tilde{y}^2} = 0, \tag{2.70}$$

the boundary condition at $\tilde{y} = \tilde{h}$ is

$$\frac{\partial \tilde{T}_0}{\partial \tilde{y}} = -Bi\ \tilde{T}_0 \tag{2.71}$$

and (2.51) remains unchanged as the boundary condition at $\tilde{y} = 0$.

The surfactant evolution equation at leading order is

$$\frac{1}{Ca}\frac{\partial \tilde{S}_0}{\partial \tilde{t}} + \frac{\partial}{\partial \tilde{x}}\left(\tilde{u}_0 \tilde{S}_0\right) = \frac{1}{Pe}\frac{\partial^2 \tilde{S}_0}{\partial \tilde{x}^2} \tag{2.72}$$

and the surfactant boundary conditions are

$$\left.\frac{\partial \tilde{S}_0}{\partial \tilde{x}}\right|_{\tilde{x}=\tilde{L}(\tilde{t})} = \tilde{S}_T\left(\tilde{S}_0\big|_{\tilde{x}=\tilde{L}(\tilde{t})} - \tilde{S}_S\right), \tag{2.73a}$$

$$\left.\frac{\partial \tilde{S}_0}{\partial \tilde{x}}\right|_{\tilde{x}=\tilde{R}(\tilde{t})} = -\tilde{S}_T\left(\tilde{S}_0\big|_{\tilde{x}=\tilde{R}(\tilde{t})} - \tilde{S}_S\right). \tag{2.73b}$$

Finally, the volume of surfactant is given by

$$\tilde{V}_S = \int_{\tilde{L}}^{\tilde{R}} \tilde{S}_0(\tilde{x}, \tilde{t}) d\tilde{x}. \tag{2.74}$$

We will now drop the tildes over and subscripts to the nondimensional variables.

2.4 Derivation of Evolution Equations

A set of linked partial differential equations for droplet height, contact line motion, and surfactant concentration will now be derived from the leading order nondimensional equations. Integrating (2.62) with respect to y reveals that

$$p = -\frac{B}{Ca}y + \frac{1}{Ca}q(x,t). \tag{2.75}$$

Using this result in (2.67) gives

$$q(x,t) = Bh - \frac{\partial^2 h}{\partial x^2}. \tag{2.76}$$

Substituting (2.75) and (2.76) in (2.61) produces

$$\frac{1}{Ca}\frac{\partial q}{\partial x} = \frac{\partial^2 u}{\partial y^2}, \tag{2.77}$$

which can be integrated twice to find

$$u = \frac{1}{Ca}\frac{\partial q}{\partial x}\frac{y^2}{2} + A(x,t)y + C(x,t). \tag{2.78}$$

Use this result in (2.66) and see that

$$A(x,t) = \frac{2}{Ca}\frac{\partial \Sigma}{\partial x} - \frac{1}{Ca}\frac{\partial q}{\partial x}h. \tag{2.79}$$

Now, use (2.78) and (2.79) in (2.64) to solve for C:

$$C(x,t) = \lambda_0 A(x,t) = \frac{\lambda_0}{Ca}\left(2\frac{\partial \Sigma}{\partial x} - \frac{\partial q}{\partial x}h\right). \tag{2.80}$$

Substitute (2.78) - (2.80) into (2.60):

$$\frac{\partial u}{\partial x} + \frac{\partial v}{\partial y} = 0. \tag{2.81}$$

Now, integrate this one time with respect to y to solve for v:

$$\begin{aligned} v &= -\frac{\partial}{\partial x}\left(\int u dy\right) + D(x,t) \\ &= -\frac{1}{Ca}\frac{\partial}{\partial x}\left[\frac{\partial q}{\partial x}\frac{y^3}{6} + \left(2\frac{\partial \Sigma}{\partial x} - \frac{\partial q}{\partial x}h\right)\frac{y^2}{2}\right. \\ &\quad \left. + \frac{\lambda_0}{Ca}\left(2\frac{\partial \Sigma}{\partial x} - \frac{\partial q}{\partial x}h\right)y\right] + D(x,t) \end{aligned} \tag{2.82}$$

$$v = \frac{1}{Ca}\frac{\partial}{\partial x}\left[\frac{\partial q}{\partial x}\left(\frac{y^2}{2}h - \frac{y^3}{6} + \lambda_0 y h\right) - 2\frac{\partial \Sigma}{\partial x}\left(\frac{y^2}{2} + \lambda_0 y\right)\right] + D(x,t). \tag{2.83}$$

Use (2.78) - (2.82) in (2.63) and solve for $D(x,t)$:

$$D(x,t) = 0 \tag{2.84}$$

Finally, substitute (2.78) - (2.84) into (2.65) to get a partial differential equation for $h(x,t)$:

$$\frac{\partial h}{\partial t} = \frac{\partial}{\partial x}\left(W\frac{\partial q}{\partial x} - V\frac{\partial \Sigma}{\partial x}\right) \tag{2.85}$$

where

$$W = \left[\frac{h^3}{3} + \lambda_0 h^2\right], \tag{2.86}$$

$$V = 2\left[\frac{h^2}{2} + \lambda_0 h\right]. \tag{2.87}$$

Although there is now an evolution equation for the droplet height, one is still needed for temperature. The first step is to integrate (2.70) twice with respect to y

$$T(x, y, t) = J(x, t)y + K(x, t). \tag{2.88}$$

Now evaluate (2.88) at $y = 0$ to solve for $K(x, t)$ by using (2.51):

$$K(x, t) = 1 - N\ x. \tag{2.89}$$

Use (2.71) to evaluate (2.88) at $y = h$:

$$J(x, t) = -Bi\ T(x, h, t). \tag{2.90}$$

It is possible to construct a solution for the temperature at any point in the droplet, but we are only interested in the temperature on the interface $y = h$. We thus have the temperature profile of

$$T\left(x, y, t\right)\Big|_{y=h} = \frac{1 - N\ x}{1 + Bi\ h}. \tag{2.91}$$

Taken together, (2.85)–(2.87) with boundary conditions (2.47) form the droplet height evolution equation, the contact line is advanced by (2.69), the temperature profile on the surface is given by (2.91), and the surfactant concentration is determined by (2.72) with boundary conditions (2.73).

2.5 Volume Conservation

Volume is automatically conserved in this formulation of the problem. Fluid volume is given by

$$V_F = \int_{L(t)}^{R(t)} h(x, t)dx. \tag{2.92}$$

Volume conservation is proved by showing that the change in volume in time is zero:

$$\frac{dV_F}{dt} = \dot{R}(t)h\Big|_{x=R} - \dot{L}(t)h\Big|_{x=L} + \int_{L(t)}^{R(t)} \frac{\partial h}{\partial t} dx. \tag{2.93}$$

The contact conditions (2.47) are used to reduce this to

$$\begin{aligned} \frac{dV_F}{dt} &= \int_L^R \frac{\partial h}{\partial t} dx & (2.94)\\ &= \int_L^R \frac{\partial}{\partial x}\left(W\frac{\partial q}{\partial x} - V\frac{\partial \Sigma}{\partial x}\right) dx & (2.95)\\ &= \left(W\frac{\partial q}{\partial x} - V\frac{\partial \Sigma}{\partial x}\right)\Big|_{x=L}^{x=R} & (2.96) \end{aligned}$$

W is zero at the contact lines. Similarly, for our choice of $\lambda(h) = \lambda_0$, V is zero at the contact lines. If we had chosen $\lambda = \frac{\lambda_1}{h}$, V is non-zero at the contact lines and thus it is required that $\frac{\partial \Sigma}{\partial x}$ be zero there. This can only happen if there is no heat in the problem ($\delta = 0$) and if there is no flux of surfactant at the ends. This analysis provides an important limitation on the singular slip law; to have a well posed problem we must restrict ourselves to constant slip if we have a temperature gradient or flux of surfactant in the problem. For this reason we will only consider the constant slip case, $\lambda(h) = \lambda_0$, in this analysis. As long as the constant slip model is used, however, volume is conserved:

$$\frac{dV_F}{dt} = 0. \tag{2.97}$$

As with the volume of the droplet, it will now be shown that surfactant is automatically conserved in this formulation of the problem. At leading order, the total amount of surfactant on the drop is given by (2.74). As before, conservation of surfactant will be proved by showing that the change in total surfactant in time is zero.

$$\begin{aligned} \frac{dV_S}{dt} &= \frac{\partial}{\partial t}\int_{L(t)}^{R(t)} S(x,t)\, dx & (2.98)\\ &= \dot{R}\, S\Big|_{x=R} - \dot{L}\, S\Big|_{x=L} + \int_L^R \frac{\partial S}{\partial t} dx & (2.99)\\ &= \dot{R}\, S\Big|_{x=R} - \dot{L}\, S\Big|_{x=L} + Ca\int_{x=L}^{x=R} \frac{\partial}{\partial x}\left(\frac{1}{Pe}\frac{\partial S}{\partial x} - u\, S\right) dx & (2.100)\\ &= \dot{R}\, S\Big|_{x=R} - \dot{L}\, S\Big|_{x=L} + Ca\left(\frac{1}{Pe}\frac{\partial S}{\partial x} - u\, S\right)\Big|_{x=L}^{x=R} & (2.101) \end{aligned}$$

At the contact points, $\dot{R} = Ca\ u\big|_{x=R}$ and $\dot{L} = Ca\ u\big|_{x=L}$, which allow (2.98) to be reduced to

$$\frac{dS}{dt} = \frac{Ca}{Pe}\frac{\partial S}{\partial x}\bigg|_L^R. \tag{2.102}$$

If there are no-flux conditions at the boundaries, $S_T = 0$, then

$$\frac{dS}{dt} = 0. \tag{2.103}$$

If, however, there is a non-zero flux, then (2.102) represents how much surfactant transfers to or from the surface onto the substrate and demonstrates that the amount of surfactant on the droplet is time dependent.

2.6 Summary

We will now summarize the governing equations. The droplet evolution equation is given by:

$$\frac{\partial h}{\partial t} = \frac{\partial}{\partial x}\left(W\frac{\partial q}{\partial x} - V\frac{\partial \Sigma}{\partial x}\right) \tag{2.104}$$

where

$$W = \left[\frac{h^3}{3} + \lambda_0 h^2\right], \tag{2.105}$$

$$V = 2\left[\frac{h^2}{2} + \lambda_0 h\right], \tag{2.106}$$

$$q(x,t) = Bh - \frac{\partial^2 h}{\partial x^2}, \tag{2.107}$$

$$\Sigma = -\delta\,(T-1) - \beta S, \tag{2.108}$$

$$T\,(x,y,t)\Big|_{y=h} = \frac{1 - N\ x}{1 + Bi\ h}. \tag{2.109}$$

The boundary conditions on height are

$$h(R,t) = 0, \tag{2.110a}$$

$$h(L,t) = 0, \tag{2.110b}$$

The surfactant evolution equation is:

$$\frac{1}{Ca}\frac{\partial S}{\partial t} + \frac{\partial}{\partial x}\,(uS) = \frac{1}{Pe}\frac{\partial^2 S}{\partial x^2} \tag{2.111}$$

where

$$u = -\frac{1}{Ca}\frac{\partial q}{\partial x}\frac{h^2}{2} + \frac{2}{Ca}\frac{\partial \Sigma}{\partial x}h + \frac{\lambda_0}{Ca}\left(2\frac{\partial \Sigma}{\partial x} - \frac{\partial q}{\partial x}h\right), \tag{2.112}$$

and the surfactant boundary conditions are

$$\left.\frac{\partial S}{\partial x}\right|_{x=L(t)} = S_T\left(S\big|_{x=L(t)} - S_S\right), \tag{2.113a}$$

$$\left.\frac{\partial S}{\partial x}\right|_{x=R(t)} = -S_T\left(S\big|_{x=R(t)} - S_S\right). \tag{2.113b}$$

Finally, the contact lines are advanced by

$$\frac{1}{Ca}\frac{dR}{dt} = f\left(-\left.\frac{\partial h}{\partial x}\right|_{x=R}\right), \tag{2.114a}$$

$$\frac{1}{Ca}\frac{dL}{dt} = f\left(\left.\frac{\partial h}{\partial x}\right|_{x=L}\right) \tag{2.114b}$$

where

$$f(\theta) = \begin{cases} (\theta - \theta_{Adv}), & \theta > \theta_{Adv} \\ 0, & \theta_{Rec} \le \theta \le \theta_{Adv} \\ (\theta - \theta_{Rec}), & \theta < \theta_{Rec} \end{cases}. \tag{2.115}$$

2.7 Steady State Solution

Here the steady state solutions of the problems are derived under the $M_S = 0, M_T = 0$ limit, so there is no interaction between the surfactant and the droplet. By evaluating the steady state version of (2.104), it is seen that

$$0 = \frac{\partial}{\partial x}\left(W\frac{\partial q}{\partial x}\right). \tag{2.116}$$

This is a fourth order ordinary differential equation for h. The solution must satisfy the boundary conditions given by (2.110). Setting $W = 0$ would only produce constant solutions. A solution of (2.116) can be obtained by setting

$$\frac{\partial q}{\partial x} = 0. \tag{2.117}$$

Integrating once gives:

$$Bh - \frac{\partial^2 h}{\partial x^2} = A, \tag{2.118}$$

where A is some constant.

For the $B = 0$ limit, the solution to this problem, with the appropriate boundary conditions, is

$$h = \theta_S \left(\frac{R+L}{R-L} x - \frac{x^2}{R-L} - \frac{RL}{R-L} \right) \tag{2.119}$$

with θ_S being the steady state contact angle. A symmetric result is easily achieved by setting $L = -R$.

For $B \neq 0$, the solution is

$$h = \frac{\theta_S}{\exp\left[\sqrt{B}L\right] - \exp\left[\sqrt{B}R\right]} \sqrt{\frac{1}{B}} \Bigg\{ \exp\left[-\sqrt{B}\,(x - R - L)\right] - \exp\left[\sqrt{B}L\right] - \exp\left[\sqrt{B}R\right] + \exp\left[\sqrt{B}x\right] \Bigg\}. \tag{2.120}$$

Once again, a symmetric result is gained by setting $L = -R$.

For any value of Bond number, the only steady state solution for surfactant is a constant.

2.8 Substrate Surfactant Gradient

The case of a substrate that has been doped with a gradient of surfactant is also considered. In particular, the situation envisioned here is where one side of the substrate is hydrophobic, resulting in a large static contact angle, while the other side is hydrophilic with a smaller static angle. Such a situation is studied by Daniel *et al.*[14]. They formed gradients of this sort by evaporating a drop of surface tension lowering compound over the substrate. Large amounts of the compound condensed in the neighborhood of the evaporating drop, resulting in a hydrophobic surface, while away from it the surface was hydrophilic. Since this gradient affects the static contact angle; it also affects the dynamics of the droplet spreading. In particular, this gradient will allow the droplet to translate along the substrate.

A simple model of how the surfactant gradient along the substrate affects the static contact angle is chosen:

$$\theta_{Rec} = \theta_{Rec_S} + G_A \exp\left[-G_B\, x\right], \tag{2.121a}$$

$$\theta_{Adv} = \theta_{Adv_S} + G_A \exp\left[-G_B\, x\right], \tag{2.121b}$$

where G_A and G_B are constants that depend upon the properties of the surfactant gradient laid down and θ_{Rec_S} and θ_{Adv_S} are the static receding and advancing contact angles that would exist if the substrate had no surface tension gradient. Implicit in this model is the assumption that surfactant absorbed onto or desorbed from the droplet interface does not change (2.121). A related model was studied by Greenspan[35].

2.9 Variable Static Contact Angle

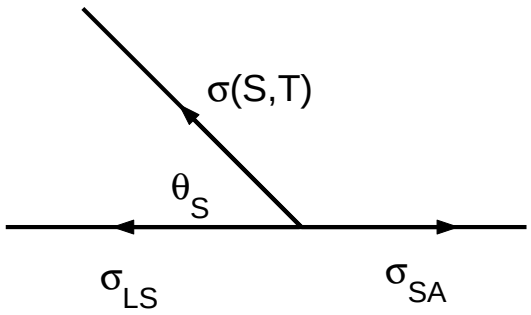

Figure 2.2: Illustration of Young's Law

Young's Law is a balance of the horizontal forces at the contact point and states that

$$\sigma_{SA} = \sigma_{LS} + \sigma \cos(\theta) \tag{2.122}$$

(see Fig. 2.2). Dimensional coordinates are used here and, for the moment, there is no restriction on the magnitude of θ. Only the case of a single static contact angle, θ_S, at one contact line is considered; a generalization to allow for hysteresis follows in a straight-forward way.

For constant values of θ_{LS} and θ_{SA}, equation (2.122) can be rearranged to show that

$$\sigma_{SA} - \sigma_{LS} = constant = \sigma(S,T)\cos(\theta_S) = \sigma_c \cos(\theta_C), \tag{2.123}$$

where θ_C is what θ_S would be without the presence of surfactant and at $T = T_\infty$ (i.e., at the reference temperature). Let $\theta = \epsilon\tilde{\theta}$ where $\epsilon \ll 1$, i.e., consider the lubrication

limit where the droplet is thin. Equation (2.123) for small ϵ gives

$$\sigma\left(1-\frac{1}{2}\epsilon^2\theta_S^2\right) \sim \sigma_c\left(1-\frac{1}{2}\epsilon^2\theta_C^2\right). \tag{2.124}$$

Suppose one, as follows from (2.32), sets

$$\sigma(S,T) = \sigma_c\left[1+\epsilon^2\tilde{\Sigma}(S,T)\right], \tag{2.125}$$

where the nondimensional $\tilde{\Sigma}(S,T)$ is given by (2.43). Equation (2.125) ensures that the surface tension is maximal when no surfactant is present. Using (2.125) in the equation of state (2.124) leads to

$$\theta_S^2 \sim \theta_C^2 + 2\tilde{\Sigma}(S,T)\Big|_{x=R}. \tag{2.126}$$

This relationship implies that the surfactant will lower the static contact angle since adding surfactant lowers surface tension, which requires a smaller θ_S in order to balance the horizontal force in (2.123). It is assumed that if $\theta_C^2 + 2\tilde{\Sigma}(S,T) < 0$, then θ_S simply becomes zero. One important implication of this assumption is that this formula has no effect on θ_S if $\theta_C = 0$ since $\tilde{\Sigma}(S,T) \leq 0$.

Chapter 3

Two-Dimensional Numerical Method

The droplet evolution equation, (2.104), subject to boundary conditions (2.110), the surfactant transport equation, (2.111), subject to boundary conditions (2.113), and the radii evolution equations (2.114) are solved using a numerical method employing backward Euler time stepping and Chebyshev pseudo-spectral special derivatives. The Chebyshev scheme has the advantage that it bunches points near the contact lines, where the dynamics are the most sensitive. The resulting nonlinear system is then solved by Newton's method. Although the method is only first order in time, it is extremely robust.

3.1 Singularity Removal

In order to get accurate numerical results when surfactants and temperature coexist in the problem, it is necessary to account for the contact lines' singularity in the numerical method. This is accomplished by first analytically identifying the singularity then removing it from the numerical calculations.

A Frobenius analysis of the droplet in the neighborhood of the contact line reveals that the leading order form of the droplet height and surfactant concentrations at the right end point are

$$\begin{aligned} h &\sim -\frac{\theta_R}{2R}x^2 + \frac{R\,\theta_R}{2} \\ &+ \epsilon^2\left\{\frac{2\lambda_0\left[\beta\, g_1 + \delta\left(N - Bi\;\theta_R\left(1 - NR\right)\right)\right] - \dot{R}}{2\theta_R\lambda_0}\xi^2\ln(\xi)\right. \\ &+ \left. b\xi^2 + O(\xi^3)\right\} \end{aligned} \tag{3.1}$$

and

$$S \sim S_0 + \epsilon \left[g_1 \xi + O(\xi^2) \right], \tag{3.2}$$

where

$$\xi = \frac{R - x}{\epsilon} \tag{3.3}$$

and

$$g_1 = \left. \frac{\partial S}{\partial x} \right|_{x=R}. \tag{3.4}$$

For full details of the Frobenius analysis, see Appendix A.

The Frobenius analysis, and a similar one at the left end point, is used to re-scale the height as

$$h(x,t) = H(x,t) + a_R(t)(R-x)^2 \ln(R-x) + a_L(t)(x-L)^2 \ln(x-L), \tag{3.5}$$

where a_R and a_L are the following time dependent variables

$$a_R = \left\{ 2\lambda_0 \left[\beta \, g_{1R} + \delta \left(N - Bi \, \theta_R \left(1 - N \, R \right) \right) \right] - \dot{R} \right\} \left(2\theta_R \lambda_0 \right)^{-1}, \tag{3.6a}$$

$$a_L = \left\{ 2\lambda_0 \left[\beta \, g_{1L} - \delta \left(N + Bi \, \theta_L \left(1 - N \, L \right) \right) \right] + \dot{L} \right\} \left(2\theta_L \lambda_0 \right)^{-1}, \tag{3.6b}$$

and

$$g_{1R} = \left. \frac{\partial S}{\partial x} \right|_{x=R}, \tag{3.7a}$$

$$g_{1L} = \left. \frac{\partial S}{\partial x} \right|_{x=L}. \tag{3.7b}$$

This change of variables from h to H allows derivatives to be calculated more accurately because the leading form of the contact lines' singularity is known and thus the third derivative of H can be made finite in the neighborhood of the contact lines whereas h itself is singular. The new formulation of the problem is formally given by

$$\begin{aligned} \frac{\partial H}{\partial t} = & -\frac{\partial}{\partial t} \left[a_R \left(R - x \right)^2 \ln(R-x) + a_L (x-L)^2 \ln(x-L) \right] \\ & + \frac{\partial}{\partial x} \left(W \frac{\partial q}{\partial x} - V \frac{\partial \Sigma}{\partial x} \right), \end{aligned} \tag{3.8}$$

where W and V are given by (2.105)–(2.106), q is given by (2.107), and Σ is given by (2.108). The new boundary conditions on H are

$$H(R,t) = -a_L (R-L)^2 \ln(R-L), \tag{3.9}$$

$$H(L,t) = -a_R (R-L)^2 \ln(R-L). \tag{3.10}$$

Surfactant is still transported via (2.111) with boundary conditions (2.57). The temperature on the droplet surface is also still given by (2.109).

3.2 Conversion into Chebyshev Space

In order to use Chebyshev derivatives, we must convert our problem from real space into Chebyshev space. The first step in rescaling the variables is to map the domain of the problem from $x \in [L, R]$ onto $\xi \in [-1, 1]$.

$$x = \frac{R(t) - L(t)}{2}\xi + \frac{R(t) + L(t)}{2}, \tag{3.11}$$

$$H(x,t) = (R(t) - L(t))\,\tilde{H}(\xi, t), \tag{3.12}$$

Since x is now a function of t, derivatives with respect to t are now taken as

$$\frac{\partial}{\partial t} = \frac{\partial}{\partial \tau} - \frac{\frac{dR}{d\tau} + \frac{dL}{d\tau} + \xi\left(\frac{dR}{d\tau} - \frac{dL}{d\tau}\right)}{R - L}\frac{\partial}{\partial \xi} \tag{3.13}$$

where $\tau = t$. Derivatives with respect to x now become

$$\frac{\partial}{\partial x} = \frac{2}{R - L}\frac{\partial}{\partial \xi}. \tag{3.14}$$

The problem once again needs to be reformulated. This time the droplet evolution equation is formally written as

$$\begin{aligned}
(R-L)\frac{\partial \tilde{H}}{\partial \tau} = &-\left(\frac{\partial R}{\partial \tau} - \frac{\partial L}{\partial \tau}\right)\tilde{H} + \left[\frac{dR}{d\tau} + \frac{dL}{d\tau} + \xi\left(\frac{dR}{d\tau} - \frac{dL}{d\tau}\right)\right]\frac{\partial \tilde{H}}{\partial \xi} \\
&- \frac{\partial}{\partial \tau}\left[a_R\left(\frac{R-L}{2} - \frac{R-L}{2}\xi\right)^2 \ln\left(\frac{R-L}{2} - \frac{R-L}{2}\xi\right)\right. \\
&\left. + a_L\left(\frac{R-L}{2}\xi + \frac{R-L}{2}\right)^2 \ln\left(\frac{R-L}{2}\xi + \frac{R-L}{2}\right)\right] \\
&+ \frac{\frac{dR}{d\tau} + \frac{dL}{d\tau} + \xi\left(\frac{dR}{d\tau} - \frac{dL}{d\tau}\right)}{R-L}\frac{\partial}{\partial \xi}\left[a_R\left(\frac{R-L}{2} - \frac{R-L}{2}\xi\right)^2 \ln\left(\frac{R-L}{2} - \frac{R-L}{2}\xi\right)\right. \\
&\left. + a_L\left(\frac{R-L}{2}\xi + \frac{R-L}{2}\right)^2 \ln\left(\frac{R-L}{2}\xi + \frac{R-L}{2}\right)\right] \\
&+ \frac{4}{(R-L)^2}\frac{\partial}{\partial \xi}\left(W\frac{\partial q}{\partial \xi} - V\frac{\partial \Sigma}{\partial \xi}\right),
\end{aligned} \tag{3.15}$$

where W and V are given by (2.105)–(2.106), q is given by (2.107), and Σ is given by (2.108), all having been transformed via (3.5) and (3.11)–(3.12). The new boundary conditions on $\tilde{H}$ are

$$\tilde{H}(1,t) = -a_L(R-L)\ln(R-L), \tag{3.16}$$

$$\tilde{H}(-1,t) = -a_R(R-L)\ln(R-L). \tag{3.17}$$

The surfactant transport equation becomes

$$\begin{aligned}\frac{1}{Ca}\frac{\partial S}{\partial \tau} - \frac{1}{Ca}\frac{\frac{dR}{d\tau}+\frac{dL}{d\tau}+\xi\left(\frac{dR}{d\tau}-\frac{dL}{d\tau}\right)}{R-L}\frac{\partial S}{\partial \xi} + \frac{2}{R-L}\frac{\partial}{\partial \xi}(uS) \\ = \frac{1}{Pe}\frac{4}{(R-L)^2}\frac{\partial^2 S}{\partial \xi^2}\end{aligned} \tag{3.18}$$

where the boundary conditions are

$$\left.\frac{\partial S}{\partial \xi}\right|_{\xi=-1} = \frac{R-L}{2}S_T\left[S(-1,t)-S_S\right], \tag{3.19}$$

$$\left.\frac{\partial S}{\partial \xi}\right|_{\xi=1} = -\frac{R-L}{2}S_T\left[S(1,t)-S_S\right]. \tag{3.20}$$

Details of the Chebyshev pseudo-spectral method that is used to take the derivatives are given in Appendix B. One result of the distribution of Chebyshev collocation points is that it bunches points near the ends of the domain. This is fortuitous since it results in extra points near the contact line, where the dynamics occur on the shortest spatial scales.

3.3 Time Derivatives

We use a backward Euler method to advance the scheme in time. The backward Euler scheme is given by

$$\frac{\partial h}{\partial \tau} = \frac{h^{n+1}-h^n}{\Delta \tau}. \tag{3.21}$$

For all purposes other than taking derivatives, $t=\tau$ and so we will be using the more common t designation for time and Δt for timesteps. We march forward from timestep t^n to $t^{n+1}=t^n+\Delta t$. A series of nonlinear equations for $H_i^{n+1}=H(\xi_i,t^{n+1},t^n)$, $S_i^{n+1}=S(\xi_i,t^{n+1},t^n)$, $R^{n+1}=R(t^{n+1},t^n)$, $L^{n+1}=L(t^{n+1},t^n)$, $a_R^{n+1}=a_R(t^{n+1},t^n)$,

and $a_L^{n+1} = a_L(t^{n+1}, t^n)$ are constructed, where ξ_i represents the value of ξ at the i^{th} Chebyshev collocation point. The resulting nonlinear system is then solved via Newton's method. The resulting matrix is full. Using finite differences rather than a Chebyshev pseudo-spectral method to compute spatial derivatives would result in a sparse matrix, which would result in significant time savings when solving the nonlinear system. Unfortunately, in order to maintain a given level of accuracy, we would have to drastically increase the number of spatial gridpoints, which would result in a much larger matrix to invert, more than negating any time savings bought by using finite differences.

To compute the actual numerical scheme, the original h is reconstructed from $\tilde{H}$ by (3.5) and (3.12). Derivatives of h with respect to x are also reconstructed by (3.14). The Newton method used to advance the scheme is employed to satisfy the original evolution equations at each point. For more details on Newton's method, please see Press *et al.*[67]. The advantage of this formulation is that it is much easier to code than it would be to directly apply backward Euler to (3.15). Although the original evolution equation is used, the Frobenius analysis and the associated transformation from h to H is still quite useful as it allows the derivatives of h to be reconstructed from H more accurately than if the derivatives had been computed directly from h. The numerical scheme for (2.104) that is employed is given by

$$\begin{aligned}(R^{n+1}-L^{n+1})\frac{\tilde{h}^{n+1}-\tilde{h}^n}{\Delta t} &= \left(-\frac{R^{n+1}-R^n}{\Delta t}+\frac{L^{n+1}-L^n}{\Delta t}\right)\tilde{h}^{n+1} \\ +\frac{1}{\Delta t}\left[R^{n+1}-R^n+L^{n+1}-L^n+\xi\left(R^{n+1}-R^n-L^{n+1}+L^n\right)\right]\frac{\partial\tilde{h}^{n+1}}{\partial\xi} &\\ +\frac{4}{R^{n+1}-L^{n+1}}\frac{\partial}{\partial\xi}\left(W^{n+1}\frac{\partial q^{n+1}}{\partial\xi}-V^{n+1}\frac{\partial\Sigma^{n+1}}{\partial\xi}\right) &\end{aligned} \tag{3.22}$$

where

$$h = (R-L)\tilde{h}. \tag{3.23}$$

The surfactant transport equation, (2.111), is advanced by

$$\begin{aligned}\frac{1}{Ca}\frac{S^{n+1}-S^n}{\Delta t}-\frac{R^{n+1}-R^n+L^{n+1}-L^n+\xi\left(R^{n+1}-R^n-L^{n+1}+L^n\right)}{\Delta t(R^{n+1}-L^{n+1})}\frac{\partial S^{n+1}}{\partial\xi} &\\ +\frac{2}{R^{n+1}-L^{n+1}}\frac{\partial}{\partial\xi}\left(u^{n+1}S^{n+1}\right)=\frac{1}{Pe}\frac{4}{\left(R^{n+1}-L^{n+1}\right)^2}\frac{\partial^2 S^{n+1}}{\partial\xi^2} &\end{aligned} \tag{3.24}$$

Finally, the contact lines, (2.114), are updated by

$$\frac{1}{Ca}\frac{R^{n+1}-R^n}{\Delta t} = f\left(-2\frac{\partial\tilde{h}}{\partial\xi}\bigg|_{\xi=1}\right), \tag{3.25}$$

$$\frac{1}{Ca}\frac{L^{n+1}-L^n}{\Delta t} = f\left(2\frac{\partial\tilde{h}}{\partial\xi}\bigg|_{\xi=-1}\right). \tag{3.26}$$

3.4 Convergence

Spatial convergence checks were performed for a droplet in the near steady state case that is investigated in Sec. 4.3. The results of this convergence check are shown in Table 3.1. For this computation, we select $\beta = 0.25$. The timestep is $\Delta t = 10^{-5}$, and the results are presented at $t = 10$. Each row of the table corresponds to a rough doubling in the number of Chebyshev collocation points. The convergence checks do not use exactly double the number of points for each successive grid refinement because there must be $2^n + 1$ collocation points, where n is a positive integer, for the chosen derivative scheme to work. The columns indicate the difference between successive values of the numerically computed fluid volume, surfactant volume, surfactant concentration at the right endpoint, and the location of the right endpoint. Table 3.2 shows the results of a convergence check where the timestep is varied. These computations used 33 spatial collocation points and had a base timestep of $\Delta t = 10^{-5}$. This timestep equals 1 in the Timestep Change column in Table 3.2. We varied the timestep from 256 times larger than the base timestep to one quarter of the base timestep.

Gridpoints	V_F Difference	V_S Difference	S_R Difference	R Difference
$9 \rightarrow 17$	$1.09 \cdot 10^{-2}$	$2.61 \cdot 10^{-1}$	$1.42 \cdot 10^{-1}$	$8.56 \cdot 10^{-3}$
$17 \rightarrow 33$	$5.21 \cdot 10^{-4}$	$3.17 \cdot 10^{-2}$	$1.64 \cdot 10^{-2}$	$5.13 \cdot 10^{-4}$
$33 \rightarrow 65$	$1.35 \cdot 10^{-5}$	$2.36 \cdot 10^{-3}$	$1.23 \cdot 10^{-3}$	$2.17 \cdot 10^{-5}$

Table 3.1: Two-dimensional spatial convergence for near steady state droplet

The R Difference column in Table 3.1 gives the difference between the location of the right endpoint, depending on the spatial resolution. Examining the convergence of the location of the right endpoint allows us to examine the spatial

Timestep Change	V_F Difference	V_S Difference	S_R Difference	R Difference
$256 \rightarrow 128$	$2.59 \cdot 10^{-7}$	$1.67 \cdot 10^{-7}$	$1.67 \cdot 10^{-7}$	$3.94 \cdot 10^{-6}$
$128 \rightarrow 64$	$1.34 \cdot 10^{-7}$	$9.46 \cdot 10^{-8}$	$9.46 \cdot 10^{-8}$	$1.97 \cdot 10^{-6}$
$64 \rightarrow 32$	$8.51 \cdot 10^{-8}$	$2.42 \cdot 10^{-8}$	$2.42 \cdot 10^{-8}$	$2.54 \cdot 10^{-6}$
$32 \rightarrow 16$	$4.18 \cdot 10^{-8}$	$1.34 \cdot 10^{-8}$	$1.34 \cdot 10^{-8}$	$1.28 \cdot 10^{-6}$
$16 \rightarrow 8$	$2.14 \cdot 10^{-8}$	$5.86 \cdot 10^{-9}$	$3.41 \cdot 10^{-8}$	$6.40 \cdot 10^{-7}$
$8 \rightarrow 4$	$1.39 \cdot 10^{-8}$	$8.46 \cdot 10^{-10}$	$1.50 \cdot 10^{-8}$	$3.24 \cdot 10^{-7}$
$4 \rightarrow 2$	$1.03 \cdot 10^{-8}$	$4.40 \cdot 10^{-9}$	$5.26 \cdot 10^{-9}$	$1.56 \cdot 10^{-7}$
$2 \rightarrow 1$	$1.25 \cdot 10^{-8}$	$1.09 \cdot 10^{-8}$	$2.28 \cdot 10^{-9}$	$8.96 \cdot 10^{-8}$
$1 \rightarrow 1/2$	$7.41 \cdot 10^{-9}$	$7.12 \cdot 10^{-9}$	$2.04 \cdot 10^{-9}$	$4.39 \cdot 10^{-8}$
$1/2 \rightarrow 1/4$	$2.27 \cdot 10^{-9}$	$3.40 \cdot 10^{-9}$	$2.96 \cdot 10^{-9}$	$1.59 \cdot 10^{-8}$

Table 3.2: Two-dimensional time convergence for near steady state droplet

convergence of the method. As shown in Table 3.1, effectively doubling the number of points from 9 to 17 results in a difference of $8.56 \cdot 10^{-3}$ in the location of the right endpoint. Doubling the number of gridpoints again to 33 points results in a difference of $5.13 \cdot 10^{-4}$. The change in the location of the endpoint is 16 times smaller in the second case. Doubling the number of points again from 33 to 65 yields a change of $2.17 \cdot 10^{-5}$. This change in the location of the endpoint is 23 times smaller than in the previous case with 17 and 33 gridpoints. Having the difference continually shrink by a greater factor each time the points are doubled is characteristic of spectral methods. Note that the difference in the calculated volume of the fluid shrinks by a factor of nearly 40 when the cases with 17 and 33 gridpoints and the cases with 33 and 65 gridpoints are compared. Similar reductions in differences are found when the other columns are examined. The Chebyshev pseudo-spectral method was employed to achieve this extreme accuracy without the need for large number of collocation points.

Looking at the temporal convergence presented in Table 3.2, we see that each doubling of points roughly halves the difference of each computed column. For example, the amount of surfactant at the right endpoint, the S_R Difference column, is reduced from $1.67 \cdot 10^{-7}$ for the case with the largest timesteps, to $9.46 \cdot 10^{-8}$ (for

Timestep Change	V_F Difference	V_S Difference	S_R Difference	R Difference
$16 \rightarrow 32$	$4.53 \cdot 10^{-3}$	$9.21 \cdot 10^{-2}$	$5.83 \cdot 10^{-2}$	$7.96 \cdot 10^{-2}$
$32 \rightarrow 64$	$1.42 \cdot 10^{-5}$	$1.50 \cdot 10^{-2}$	$1.01 \cdot 10^{-2}$	$1.13 \cdot 10^{-2}$
$64 \rightarrow 128$	$3.07 \cdot 10^{-8}$	$3.00 \cdot 10^{-3}$	$2.43 \cdot 10^{-3}$	$2.86 \cdot 10^{-3}$

Table 3.3: Two-dimensional space convergence for wetting droplet

timesteps of 128 and 64 times the base timestep), to $2.42 \cdot 10^{-8}$ (for timesteps of 64 and 32 times the base timestep). This behavior shows that the method is first order accurate in time. There are some aberrant values in the table where one of the metrics increases when the timestep is halved (such as in the V_S column for the 8 to 4 and 4 to 2 cases). We do not find this worrying since it is not accompanied by increases in the other metrics and the general progression of halving of the differences for each halving of the timestep continues after these aberrations.

Tables 3.3 and 3.4 examine the spatial and temporal convergence of a wetting droplet, where $\theta_{Adv} = \theta_{Rec} = 0$. Here the droplet is initialized as in Sec. 4.2, with $\beta = 4$ and $Pe = 25$. In this formulation, the droplet will spread to coat the entire substrate. Examining the V_F Difference column in Table 3.3, we see that the difference in the calculated volume of fluid is reduced by 319 times between the first and second doubling of spatial points, and 460 times for the second halving of points. In this case, the accuracy is even higher than it was in the near steady state case. Table 3.4 shows that, for each of the four columns, each halving of the timestep corresponds to a halving of the difference in the computed metric. Contrary to the results for the near steady state case, here there are no aberrant results where the difference increases.

Timestep Change	V_F Difference	V_S Difference	S_R Difference	R Difference
$256 \rightarrow 128$	$3.79 \cdot 10^{-3}$	$1.31 \cdot 10^{-3}$	$8.49 \cdot 10^{-4}$	$4.17 \cdot 10^{-3}$
$128 \rightarrow 64$	$1.93 \cdot 10^{-3}$	$6.61 \cdot 10^{-4}$	$4.28 \cdot 10^{-4}$	$2.11 \cdot 10^{-3}$
$64 \rightarrow 32$	$9.72 \cdot 10^{-4}$	$3.36 \cdot 10^{-4}$	$2.17 \cdot 10^{-4}$	$1.07 \cdot 10^{-3}$
$32 \rightarrow 16$	$4.88 \cdot 10^{-4}$	$1.68 \cdot 10^{-4}$	$1.09 \cdot 10^{-4}$	$5.39 \cdot 10^{-4}$
$16 \rightarrow 8$	$2.45 \cdot 10^{-4}$	$8.41 \cdot 10^{-5}$	$5.44 \cdot 10^{-5}$	$2.70 \cdot 10^{-4}$
$8 \rightarrow 4$	$1.22 \cdot 10^{-4}$	$4.21 \cdot 10^{-5}$	$2.72 \cdot 10^{-5}$	$1.35 \cdot 10^{-4}$
$4 \rightarrow 2$	$6.12 \cdot 10^{-5}$	$2.10 \cdot 10^{-5}$	$1.36 \cdot 10^{-5}$	$6.76 \cdot 10^{-5}$
$2 \rightarrow 1$	$3.06 \cdot 10^{-5}$	$1.05 \cdot 10^{-5}$	$6.80 \cdot 10^{-6}$	$3.38 \cdot 10^{-5}$
$1 \rightarrow 1/2$	$1.53 \cdot 10^{-5}$	$5.26 \cdot 10^{-6}$	$3.40 \cdot 10^{-6}$	$1.69 \cdot 10^{-5}$
$1/2 \rightarrow 1/4$	$7.66 \cdot 10^{-6}$	$2.64 \cdot 10^{-6}$	$1.71 \cdot 10^{-6}$	$8.47 \cdot 10^{-6}$

Table 3.4: Two-dimensional time convergence for wetting droplet

Chapter 4

Two-Dimensional Results

4.1 Introduction

Initial conditions for the majority of the runs are assumed to be the steady state solution of the isothermal problem when gravitational effects are ignored. In parametric terms, this is the steady state of the problem when $B = 0$, $\delta = 0$, and $\beta = 0$ and is given by (2.119). Here, instead of the steady contact angle θ_S, we will be using an initial contact angle, θ_I, and introduce an initial radius, R_I, where the initial left endpoint is given by $-R_I$. The new formulation is thus

$$h = \frac{\theta_I}{2R_I}\left(R_I^2 - x^2\right) \tag{4.1}$$

and the initial droplet profile is a parabola. Note that the initial area of this droplet is $V_I = (2/3)\theta_I R_I^2$. In Sec. 4.3 the droplet is initialized to the steady state for $B \neq 0, \delta = 0$ and $\beta = 0$. In this case, the solution, rewriting (2.120) for symmetry ($L = -R$), is

$$h = \frac{\theta_I}{\sqrt{B}\left[\exp\left(-\sqrt{B}R_I\right) - \exp\left(\sqrt{B}R_I\right)\right]}\Big[\exp\left(-\sqrt{B}x\right) + \exp\left(\sqrt{B}x\right) - \exp\left(-\sqrt{B}R_I\right) - \exp\left(\sqrt{B}R_I\right)\Big].$$

We will now use our model equations to determine the motion of a droplet with surfactant on a heated substrate. Unless otherwise noted, all of the following results are assumed to have $R_I = 1, \beta = 1, Ca = 0.1, B = 1, Pe = 1, \lambda = 0.01, N = 0.05$, and $Bi = 0.1$. The value of δ is different in Secs. 4.2 and 4.3 and will be specified separately in each. A no-flux surfactant boundary condition at the contact lines will be used unless otherwise specified. We will refer to this as our base parameter set.

The values of the static contact angles will be given for each subsection. A uniform initial distribution of surfactant is used, with the concentration of surfactant being initialized to $S(0,x) = 1/2$ for $-R_I \leq x \leq R_I$. Other surfactant distributions have been considered and qualitatively similar dynamics have been observed. We should note that the value of the slip coefficient should be small in order to simulate a flow where slip is only important in the neighborhood of the contact line. Smaller values than the value selected here have been considered and found to give qualitatively similar computational results[37] but require significantly more computational effort.

The majority of the figures in this chapter are presented at $t = 10$. This time is chosen to be illustrative of the phenomena that the droplet experiences. At longer times, the surfactant tends to reach a uniform distribution. In the completely wetting case ($\theta_{Adv} = \theta_{Rec} = 0$), for long time we see the surfactant concentration approaching zero uniformly along the interface. Initial conditions are selected to illustrate the relevant phenomena and we have found that varying the initial conditions from those used here gives similar results.

4.2 Isothermal wetting droplets

First, consider the case where the droplet completely wets the substrate, i.e., $\theta_{Adv} = \theta_{Rec} = 0$. Assume that $\theta_I = 3$, that the initial position of the right endpoint is $x = 1$, and the left endpoint is at $x = -1$. There is no heating for this section, i.e., $\delta = 0$, so the results presented here are symmetric. Thermal effects and translating droplets will be presented in Sec. 4.3.

The effects of surfactant on droplet spreading can be seen in Fig. 4.1. Here the drop radius $R(t)$ at $t = 10$ is plotted as a function of β for different values of Peclet number. We find that increasing β (i.e., increasing the surfactant Marangoni number) decreases the spreading rate. Increasing Pe also decreases the spreading rate. As the droplet spreads outward, surfactant is convected along the surface to the contact lines. This transport lowers the concentration of surfactant on the center of the droplet and increases it at the endpoints. The resulting positive surfactant gradient leads to a negative surface tension gradient and a Marangoni flow that opposes

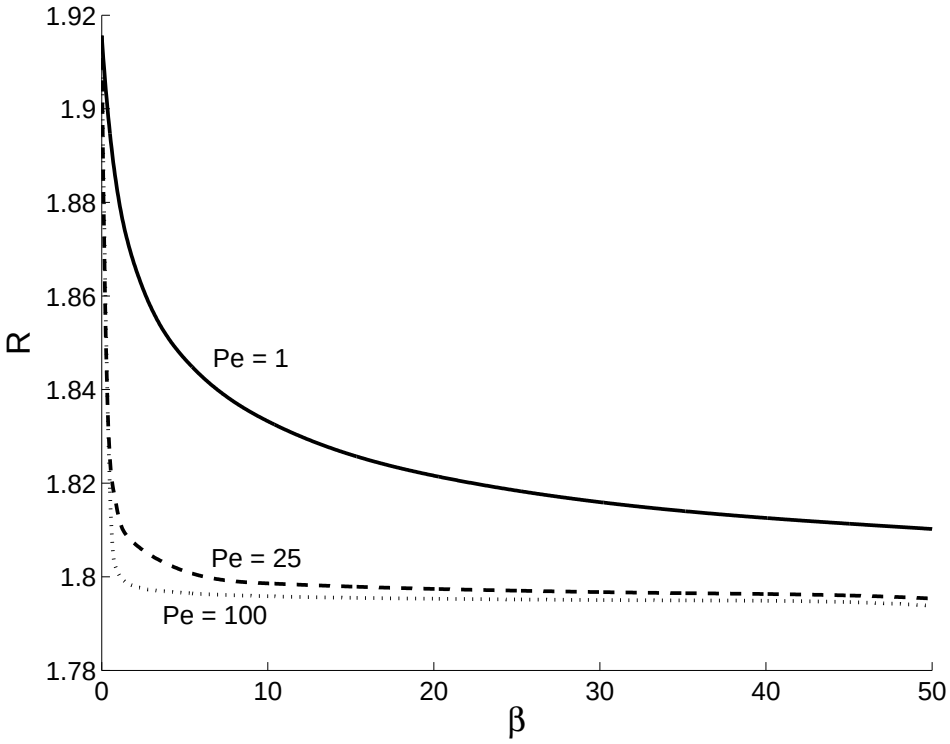

Figure 4.1: Effects of surfactant strength on spreading. Spreading distance versus β at $t = 10$. Note that increasing the strength of the surfactant reduces the spreading distance of the droplet.

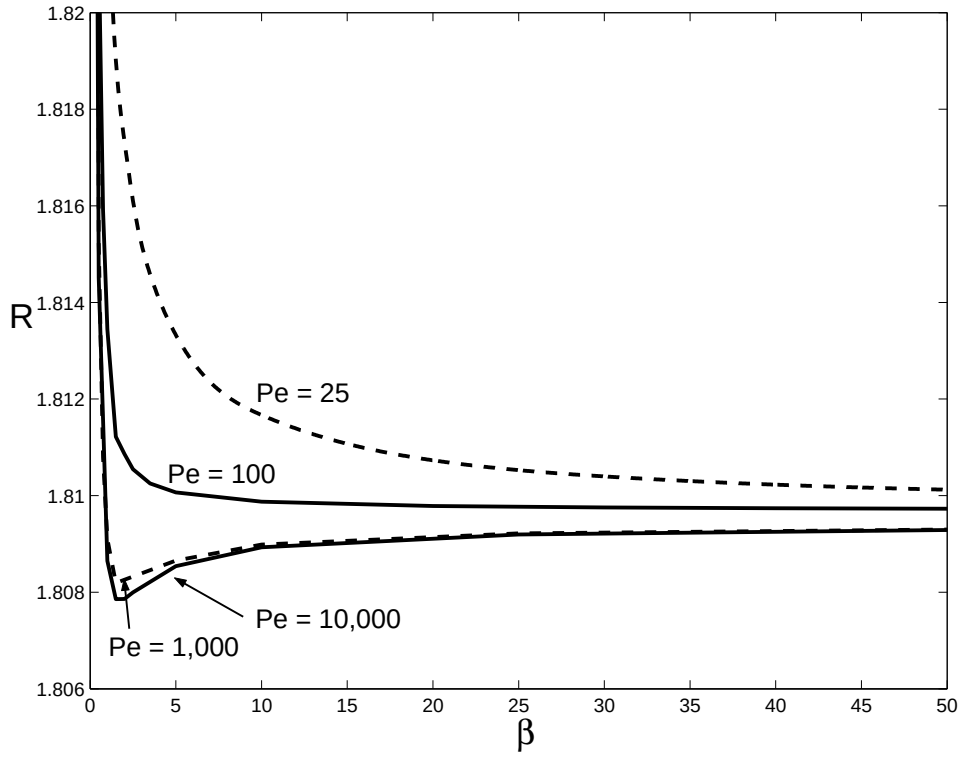

Figure 4.2: Effects of surfactant strength on spreading. Spreading distance versus β at $t = 10$. Close-up of Fig. 4.1 with results for higher Peclet numbers included. Note the minimum spreading distance.

droplet spreading. Thus the spreading rate decreases with increasing β. Higher Peclet numbers allow the surfactant to form sharper gradients, intensifying the Marangoni counterflow, and thus reducing the spreading rate. As time progresses and the droplet continues to spread, the concentration of the surfactant will decrease as it covers an ever increasing droplet wetting area. The resulting surfactant gradients and resulting Marangoni flows are thus reduced and the retardant effect of the surfactant decreases as the droplet expands. Similar results were found for three-dimensional axisymmetric spreading and are presented in Chapter 7.

Note that Fig. 4.1 is a snapshot in time. Our computations imply that if a similar plot were drawn at a later time and / or for larger Peclet numbers the

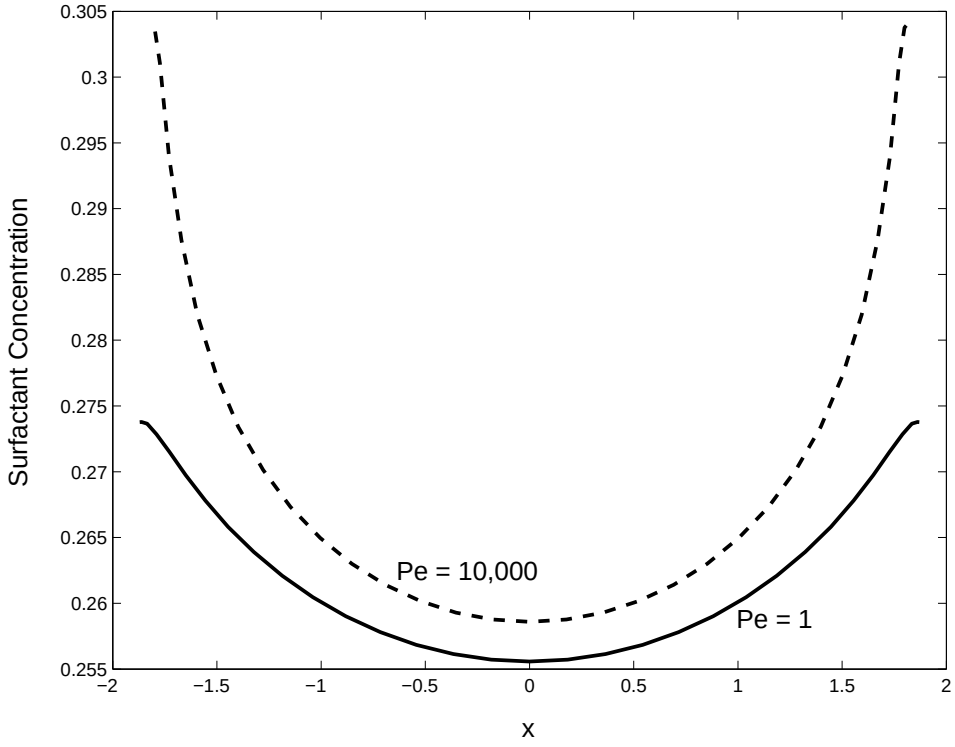

Figure 4.3: Surfactant profiles at $t = 10$ for large and small Peclet numbers. Surfactant strength is given by $\beta = 2$.

curves may have a minimum at a finite value of β and then asymptotically increase to a steady value of the spreading distance R; see Fig. 4.2 for a close-up figure where we have added additional curves for higher Peclet numbers. At shorter times, even for large Peclet numbers, the spreading distance decreases monotonically with surfactant strength. This non-monotonic spreading behavior with β is related to how the surfactant concentration varies along the surface as time increases, especially for large Peclet numbers where a boundary layer in surfactant concentration can occur near the contact line.

Example surfactant profiles can be seen in Fig. 4.3. Surfactant strength is given by $\beta = 2$ for both results. This figure shows how a large Peclet number allows large surfactant gradients to be maintained even at relatively long times. These larger surfactant gradients in the $Pe = 10,000$ case have retarded the droplet spreading, so the surfactant concentration on the droplet is, on average, higher than in the $Pe = 1$

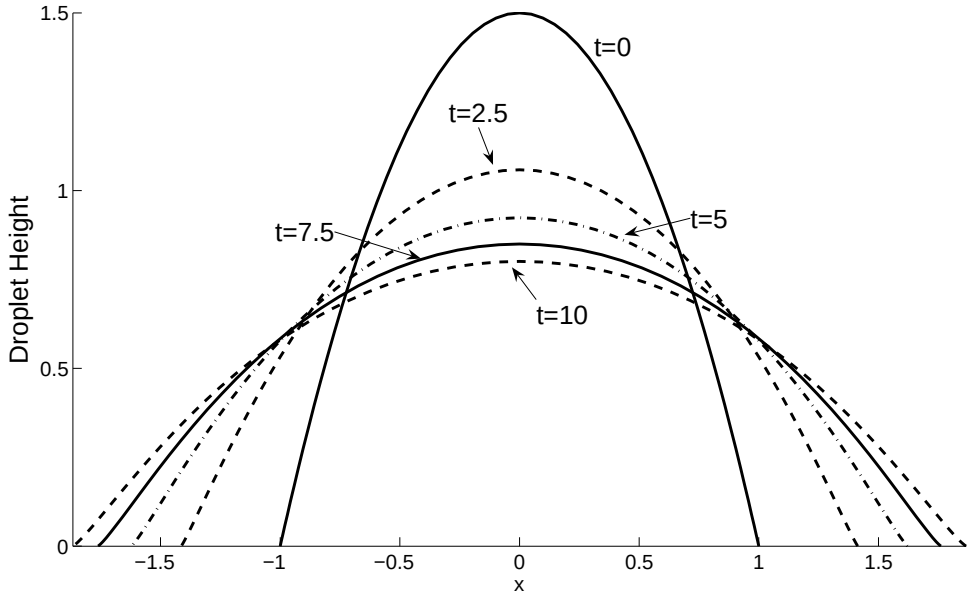

Figure 4.4: Two-dimensional droplet profiles for $\beta = 2, Pe = 1$.

case.

Example droplet profiles are shown in Fig. 4.4 for $\beta = 2, Pe = 1$. This figure shows the spreading behavior of the drop. As expected, the spreading is fastest when the droplet first begins to spread; as it spreads, the contact angle decreases, bringing it closer to the steady contact angle and thus slowing spreading. Since it is a wetting droplet, spreading will never stop, but it will continually slow. Figure 4.5 is the companion to Fig. 4.3 but showing the droplet profiles instead of surfactant concentrations. It compares the final profile for the $Pe = 1$ case to that of the $Pe = 10,000$ case. As previously described, the higher Peclet number retards the droplet spreading.

Figure 4.6 shows results when the no-flux condition at the contact line is relaxed and the flux condition (2.113) is used instead. Spreading rates for various values of S_T are shown. The no-flux, $S_T = 0$, spreading rates are also shown for comparison. In Fig. 4.6 we see that droplet spreading slows as the concentration of

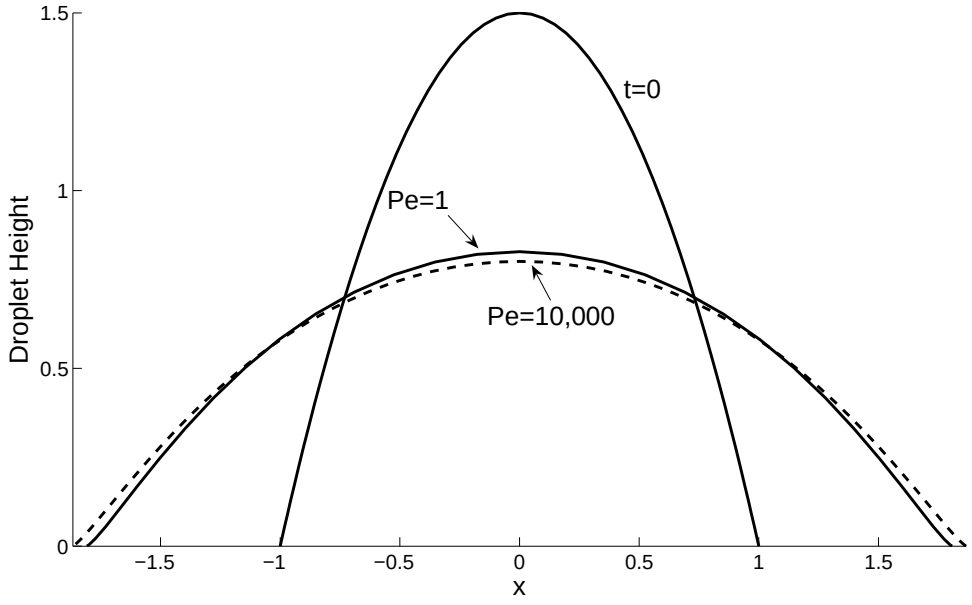

Figure 4.5: Droplet profiles at $t = 10$ for large and small Peclet numbers. Surfactant strength is given by $\beta = 2$.

surfactant on the substrate, S_S, is increased. In the cases studied here, allowing flux of surfactant off of the droplet, low S_S, increases spreading rates compared to the no-flux case. This process is easily understood; since the surfactant is leaving the droplet surface, there is a negative surfactant gradient in the neighborhood of the contact line, resulting in a reinforcing Marangoni flow in the direction of spreading and hence increasing the overall droplet spreading rate. Once all the surfactant has been drained from the surface, then the surface tension gradients are immaterial and the droplet reverts to an effective $\beta = 0$ spreading rate. For higher values of S_S this process is reversed. Surfactant absorbs from the substrate onto the surface of the droplet, creating positive local surfactant gradients and opposing Marangoni flows which slow the spreading. At sufficiently long times, allowing surfactant transfer, for $S_S \neq 0$, will always slow the droplet. The droplet will be continuously spreading, lowering the surfactant concentration on its surface. At some point, the concentration of surfactant at the contact line will fall below S_S, creating a positive surfactant gradient there as surfactant is absorbed from the substrate, and hence slowing spreading.

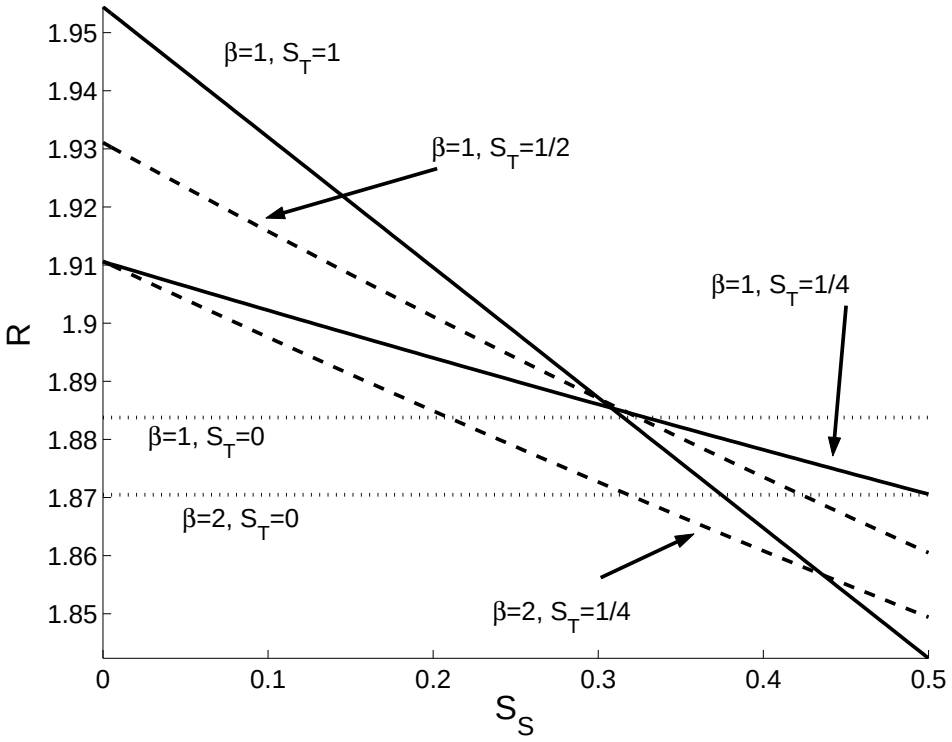

Figure 4.6: Effects of surfactant flux on spreading. Position of the right endpoint as a function of S_S at $t = 10$ for various β and S_T.

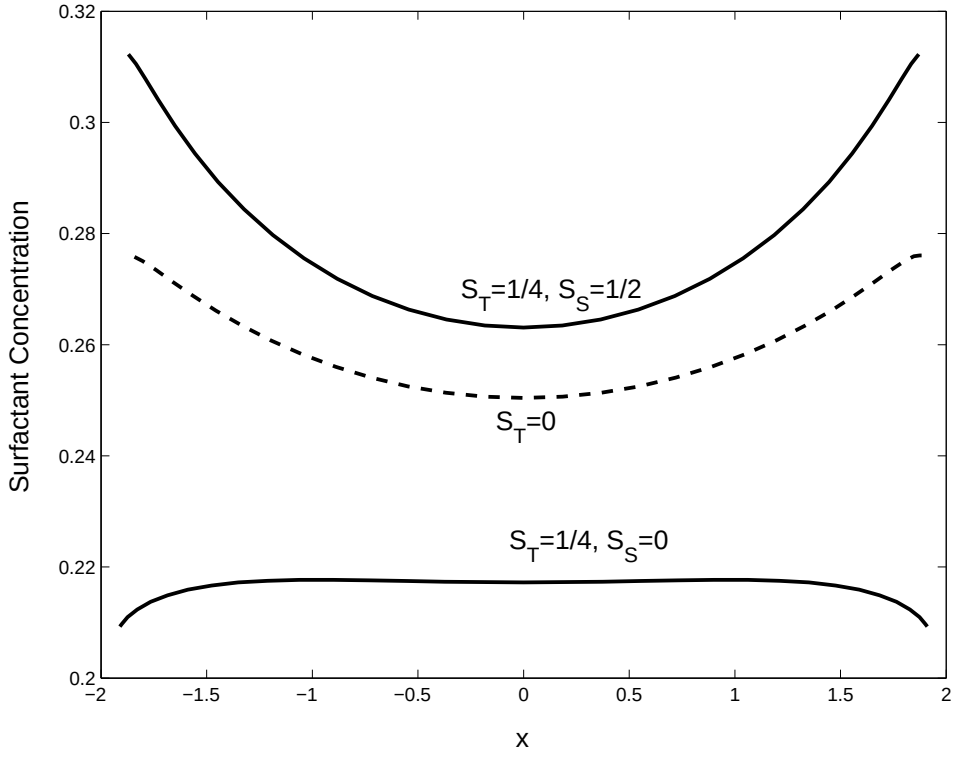

Figure 4.7: Effects of surfactant flux on spreading. Surfactant profiles at $t = 10$ with $\beta = 1$ and where flux of surfactant is allowed.

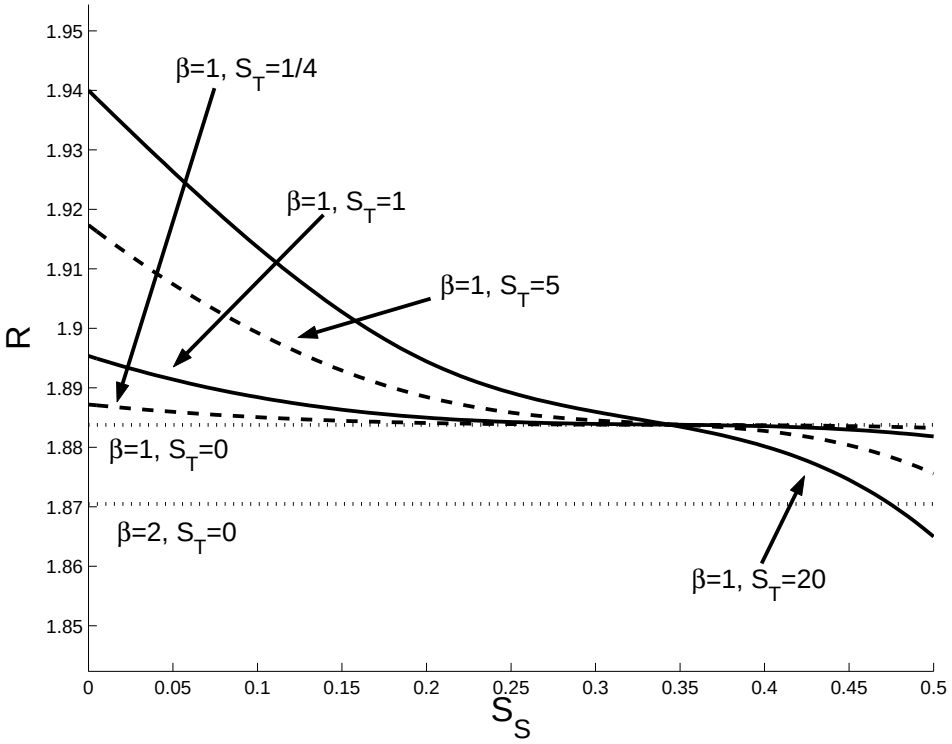

Figure 4.8: Effects of surfactant flux on spreading where a cubic flux boundary condition is used. Position of the right endpoint as a function of S_S at $t = 10$ for various β and S_T.

The effects of flux on the surfactant profiles can be seen in Fig. 4.7. The flux of surfactant from the droplet is clearly seen in the $S_S = 0$ case. The downward profile in the surfactant concentration is indicative of the surfactant leaving the droplet at the edges while remaining in the middle. As one would also expect, the overall surfactant concentration is lower in this case than in the base case with no flux. These effects are reversed when surfactant is absorbed by the droplet. In the $S_S = 1/2$ case, the surfactant is absorbed at the contact lines and increases the overall surfactant concentration on the droplet.

It is interesting to note the linear or nearly linear effect of many of the parameters on the spreading rates. For example, our computations imply that the linear dependence of the spreading rate on the steady surfactant concentration S_S, as shown in Fig. 4.6, is due to the linear form of (2.113). When this is changed to a cubic of the form $\partial S/\partial x|_{x=R} = S_T(S|_{x=R} - S_S)^3$ there is a nonlinear dependence

of R on S_S. The nonlinear behavior is shown in Fig. 4.8. We should also note that for the values of the parameters we have considered, varying the Bond and capillary numbers results in the greatest change in the spreading rate of the droplet. The Bond and capillary number comparisons are reported by Haley and Miksis[37] for droplets without surfactants. The qualitative dependence on droplet spreading on Bond and capillary numbers remains the same even in the presence of surfactants.

4.3 Near steady state comparisons

This section investigates hysteresis effects. We consider the case where $\theta_I = 3, \theta_{Adv} = 3$, and $\theta_{Rec} = 2.8$. The droplet is initialized to the steady state for the case of no surfactant or temperature gradients. Thus surfactant and temperature gradients drive the droplet spreading, and if $\delta = \beta = 0$ then the droplet will not move. Here we allow a large temperature gradient, $\delta = 4$, which causes the droplet to translate to the right in the absence of surfactant. More data on translating droplets will be presented in Sec. 4.5.

First consider the zero Marangoni number case, i.e., $\beta = 0$. This situation corresponds to passive surfactant transport along the droplet surface with no effect of surfactant on the interface shape. In this case, heating is driving the droplet motion. The droplet does not move initially since it is stuck in the hysteresis region (see Fig. 4.9). As time increases, the contact angle at the right end decreases initially, but remains larger than $\theta_{Rec} = 2.8$. Eventually, the temperature gradient forces the droplet to steepen the right contact angle until it is greater than θ_{Adv} at which point the droplet begins translating to the right and does not stop. A similar effect happens at the left contact line. Hence the heating forces the droplet to move out of its hysteresis regime and to begin translating.

More revealing is the case with both heating and surfactant. Given the results in Sec. 4.2, one would expect that, for a spreading droplet, the surfactant gradients would quickly reorient themselves to oppose droplet spreading. For the wetting droplet it is found that the concentration of surfactant, and therefore the strength of the gradients, decreases as the droplet spreads. Thus the presence of surfactant has the largest effect at short to intermediate times; at long times its

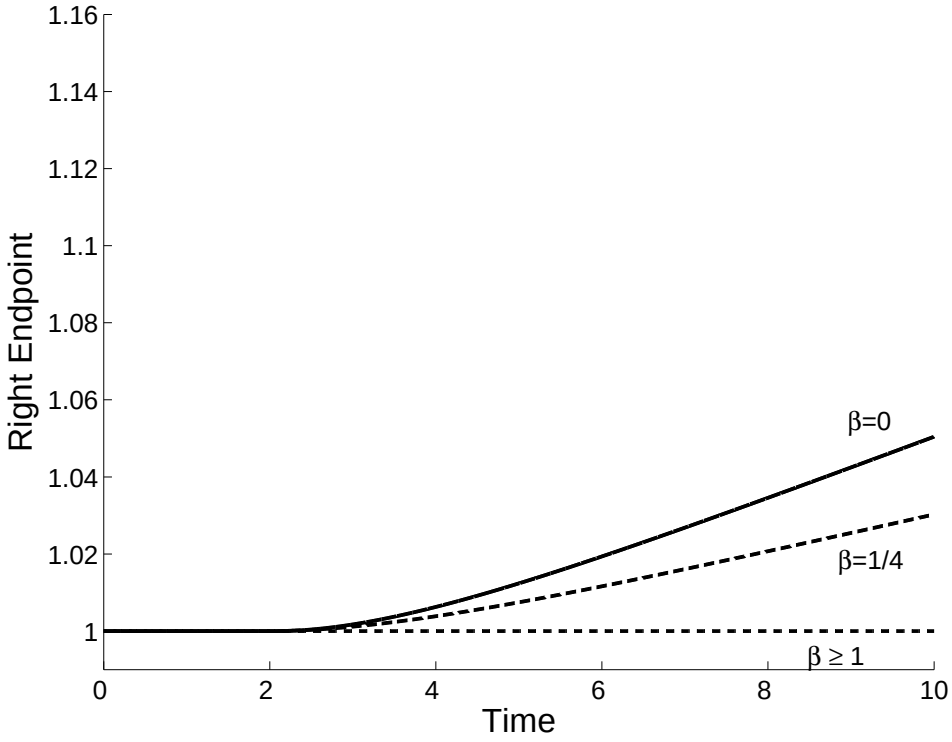

Figure 4.9: Position of the right endpoint for a near steady state droplet with heating along the surface. The droplet can become stuck for large β, i.e., large Marangoni numbers.

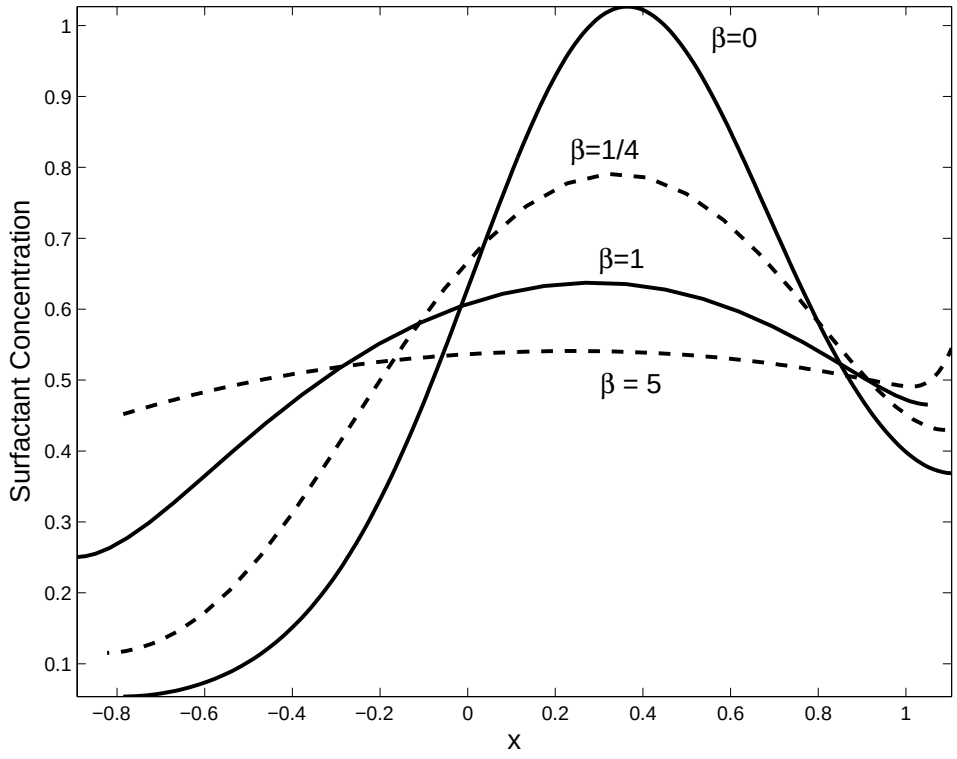

Figure 4.10: Surfactant profiles at $t = 10$ for a near steady state droplet with heating along the surface.

presence is largely irrelevant to the spreading rate. Since the droplets in this regime translate and do not change dramatically in width, one would expect the effect of the surfactant gradients to remain relatively constant; thus as the strength (β) of the surfactant increases, the droplet spreading rate should decrease as well until the droplet is barely moving. What is actually seen is that at a certain critical value of β the droplet halts completely due to hysteresis. The critical value of β is approximately one and this phenomenon can be seen in Fig. 4.9 for values of $\beta \geq 1$. Computationally we find that this behavior is not qualitatively dependent upon the value of the slip coefficient, λ. Note that if a non-uniform distribution of surfactant were present, short time surfactant driven spreading would occur, but the droplet would still become trapped for $\beta \geq 1$ after this initial spreading, even though there is still a temperature gradient on the substrate.

Surfactant profiles at $t = 10$ for the droplets are given in 4.10. Since the droplet is travelling, there is a nonsymmetric surface velocity that causes nonsymmet-

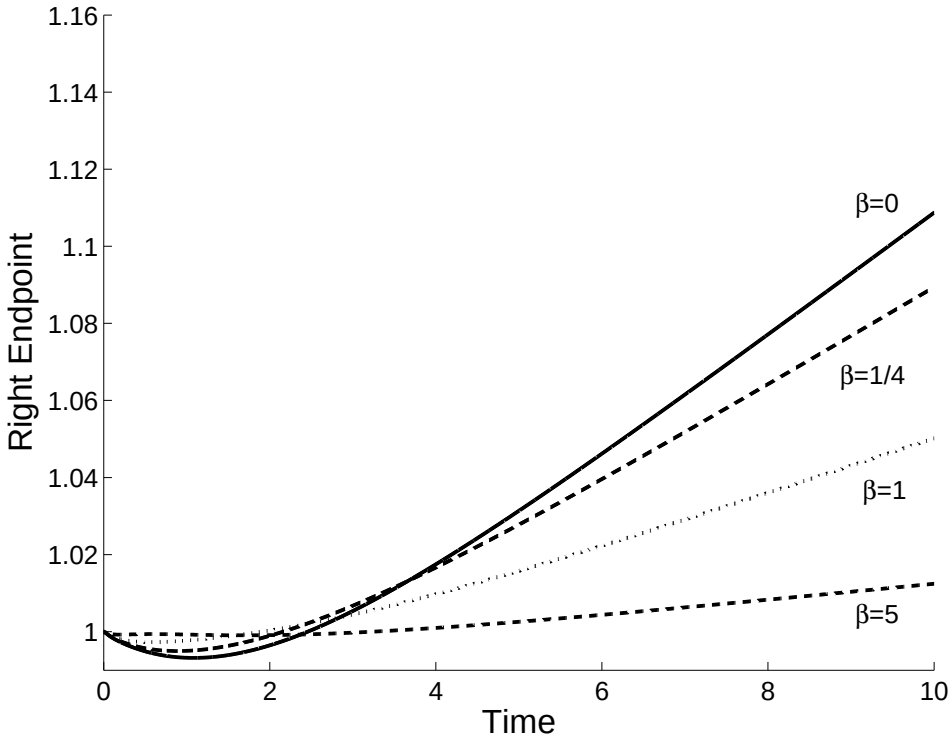

Figure 4.11: Radius of right endpoint for near steady state droplet without hysteresis. Without hysteresis to allow for the droplet to become stuck, the spreading is merely slowed by the presence of surfactant. Note that large β can cause a faster initial spreading rate while lowering spreading rates over longer times.

ric surfactant profiles. At $\beta = 0$, the surfactant is being passively carried along by the fluid. At $\beta = 1$, the surfactant is fully opposing droplet motion and has prevented the droplet from moving. As the surfactant strength increases, the surfactant gradient needed to oppose the droplet motion decreases. Thus the $\beta = 5$ surfactant profile is much flatter than the $\beta = 1$ profile, even though both of them prevent any droplet motion.

This process of stopping a droplet disappears if hysteresis is eliminated. In this case, surfactant simply slows the spreading of the droplet (see Fig. 4.11). At short times, since the droplet wants to contract, the presence of surfactant slows down the contraction rate because the flow causes a surface tension gradient toward the contact line which produces a flow opposing the contracting motion. It is only at longer times, after the droplet begins to spread outward, that surfactants act to limit

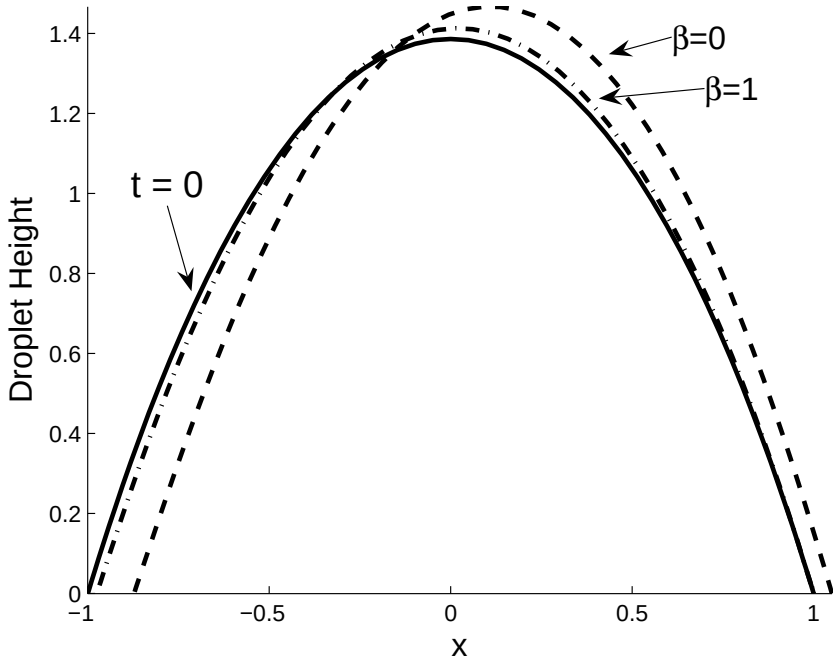

Figure 4.12: Droplet profiles at $t = 10$ for a near steady state droplet with heating along the surface.

the spreading rate of the droplet. In this partial wetting case ($\theta_{Adv} \neq 0$, $\theta_{Rec} \neq 0$), if there were a non-uniform surfactant distribution in the absence of temperature gradients or hysteresis, the droplet would undergo a short time spreading and then slowly return to its initial, steady shape. We note that similar results as found here can also be obtained for other initial data as long as θ_I is in the hysteresis region.

Droplet profiles for the near steady state droplet are seen in Fig. 4.12. The clean droplet, $\beta = 0$, is translating to the right, driven by the temperature gradient. The pinned right endpoint is clearly seen for the $\beta = 1$ case. This is contrasted with the droplet profiles presented in Fig. 4.13. Without hysteresis to allow the right endpoint to become pinned, surfactants merely slow the droplet's spreading. In this case both droplets, with and without surfactants, are translating to the right.

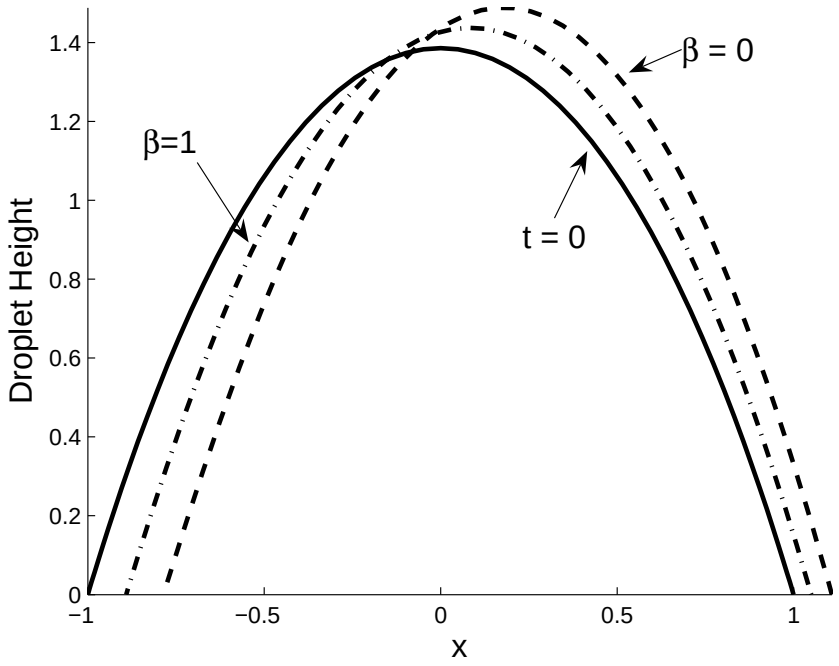

Figure 4.13: Droplet profiles at $t = 10$ for a near steady state droplet with heating along the surface without hysteresis.

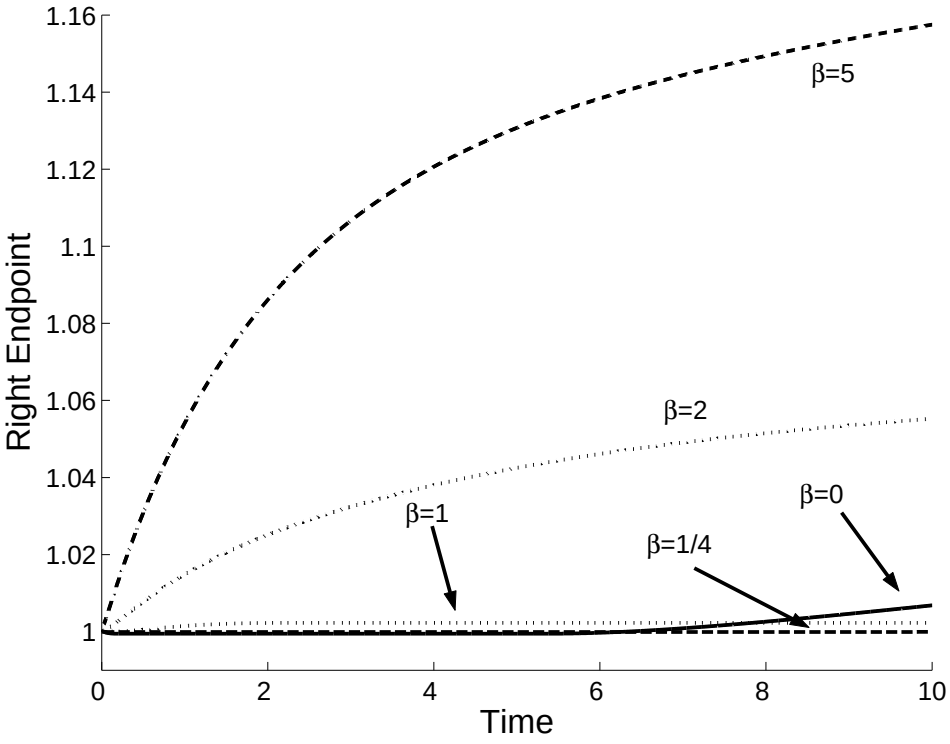

Figure 4.14: Radius of right endpoint when variable static contact angles are used. Large values of β can drastically increase droplet spreading rates.

4.4 Variable static contact angle

If the static contact angles θ_{Adv} and θ_{Rec} depend upon the local surfactant concentrations and temperatures as is described in Sec. 2.9, then different dynamics from those presented in Sec. 4.3 are observed. Suppose that the droplet is initialized exactly as it is in Sec. 4.3, aside from (2.126) being used instead of constant θ_{Adv} and θ_{Rec}.

For small surfactant Marangoni numbers, $\beta \leq 1$, the spreading rates are similar to those that use constant static contact angles. This can be observed by comparing Fig. 4.14 to Fig. 4.9. We see in Fig. 4.14 that for $\beta = 0$ and $1/4$ the droplet does not initially advance because of the hysteresis, but as time increases, the right contact angle does reach the value of θ_{Adv} and it begins to advance. This takes longer to occur than for a similar case in Fig. 4.9. For $\beta = 1$, the droplet initially spreads slightly but then becomes stuck by hysteresis and our computations do not

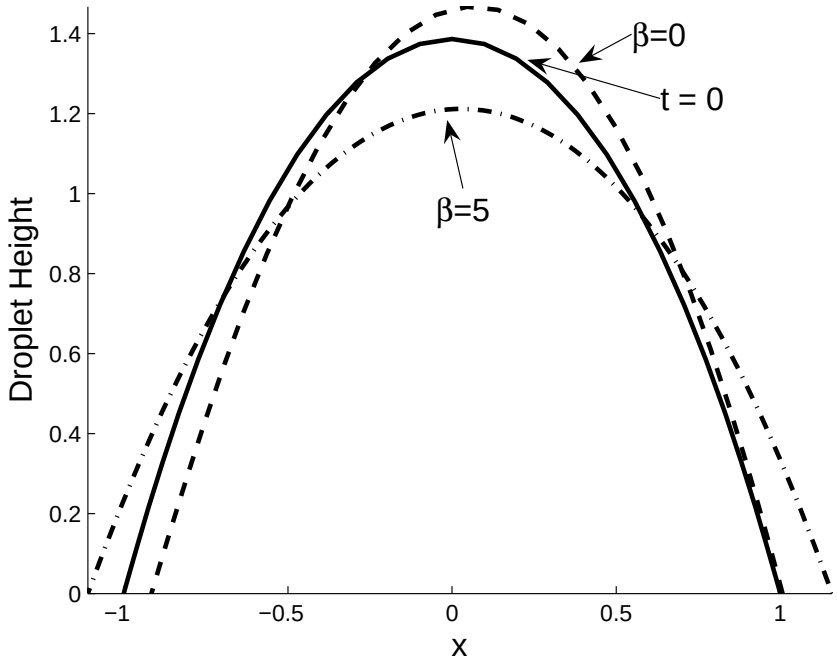

Figure 4.15: Droplet profiles at $t = 10$ for a near steady state droplet with heating along the surface when variable static contact angles are used.

imply any advance of the contact line even for large times. The $\beta = 2$ and 5 cases have a drastically different result than seen in Fig. 4.9. In particular, the droplet spreads. Here the effect of β on the variable static contact angles is much greater than its direct effect on spreading rate. The result is that the static contact angles are reduced, and allow for non-zero spreading rates. Droplet profiles contrasting the $\beta = 0$ and $\beta = 5$ cases are seen in Fig. 4.15. For $\beta \leq 1/4$ the static contact angles actually increase due to the temperature gradient, causing the droplet to initially shrink for a very short time before entering the hysteresis regime. This effect is tiny and not easily visible in Fig. 4.14.

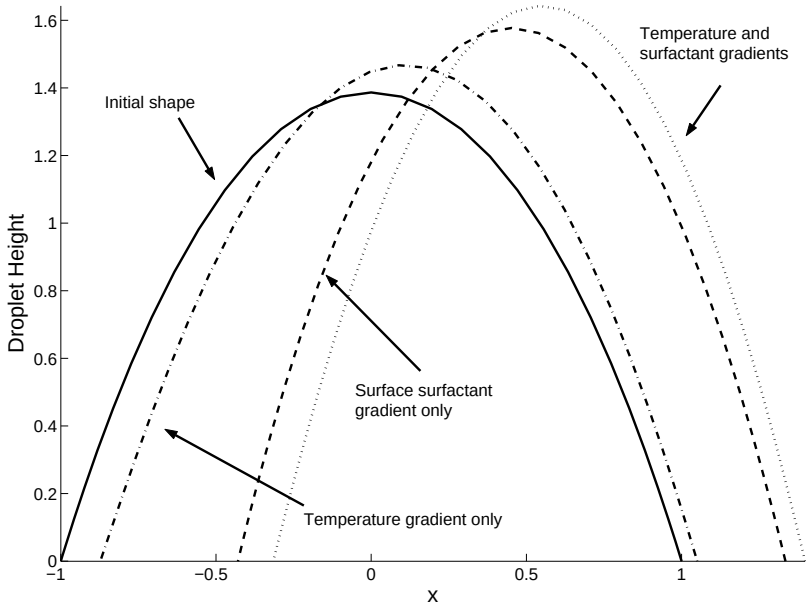

Figure 4.16: Droplets spreading on normal vs. gradient substrate at time 10.

4.5 Substrate surfactant gradient

The drop spreading case studied in Sec. 4.3 is now extended by applying a surfactant gradient to the substrate as described in Sec. 2.8. For these calculations, we set $G_A = 1$ and $G_B = 3/4$ in (2.121). As is expected, the droplet is propelled along the substrate. This effect can be combined with temperature gradients on the surface to increase spreading rates even further. The results of this can be seen in Fig. 4.16, which shows the profiles of the droplets at $t = 10$ on clean substrates versus those that have been doped with a substrate surfactant gradient.

As discussed by Wasan *et al.*[83], one reason for the rapid translation of the droplet in the substrate surfactant gradient case is that capillary flows are going in the same direction as droplet propagation. This is indicated by the fact that the leading contact angle is less than the receding contact angle. While it is only slightly less than the receding contact angle here, this contrasts sharply with the case of Sec. 4.3, where the leading contact angle is significantly greater than the receding contact angle.

Chapter 5

Three-Dimensional Axisymmetric Problem Formulation

In this chapter we will extend the previous two-dimensional analysis of a surfactant-coated droplet into three dimensions. This analysis will remain axisymmetric; full three-dimensional work will be presented in Chapters 8–10. We will not be including heat effects as the heat distribution we assumed in Chapter 2 causes translation, which would break the assumed symmetry in our formulation. Similar work, although without surfactants and surface energy dependent static contact angles, has been performed by Haley and Miksis[37].

5.1 Formulation

The problem will be formulated in cylindrical coordinates. Let r be the radial variable and z be the vertical variable. The distance from the substrate to the free surface is denoted $h(r,t)$, and $R(t)$ is the radius of the drop, which makes an angle θ with the substrate (see Fig. 5.1). Gravity, g, acts in the negative z direction. The radial and vertical components of velocity are given by u and w.

We are interested in the following equations in the bulk of the fluid: conservation of mass,

$$\frac{1}{r}\frac{\partial}{\partial r}(ru) + \frac{\partial w}{\partial z} = 0, \tag{5.1}$$

and conservation of momentum in radial and vertical directions,

$$\rho\left(\frac{\partial u}{\partial t} + u\frac{\partial u}{\partial r} + w\frac{\partial u}{\partial z}\right) = \mu\left(\nabla^2 u - \frac{u}{r^2}\right) - \frac{\partial p}{\partial r}, \tag{5.2}$$

$$\rho\left(\frac{\partial w}{\partial t} + u\frac{\partial w}{\partial r} + w\frac{\partial w}{\partial z}\right) = \mu\nabla^2 w - \frac{\partial p}{\partial z} - \rho g, \tag{5.3}$$

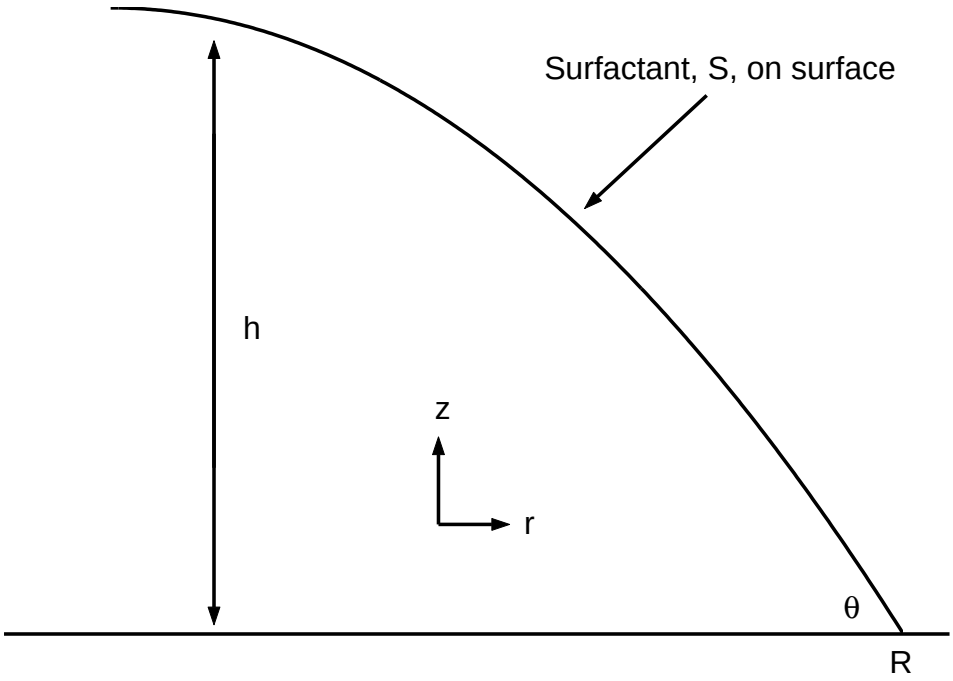

Figure 5.1: Three-dimensional axisymmetric droplet configuration

where p is the pressure in the drop, ρ is the density of drop's fluid, and μ is the viscosity of the drop.

At $z = 0$, the conditions are no penetration,

$$w = 0, \tag{5.4}$$

and, in order to relax the no-slip condition and relieve the singularity at the contact line (see e.g. Dussan V. and Davis[23]), the Navier slip condition

$$u - \lambda(h)\left(\frac{\partial u}{\partial z} + \frac{\partial w}{\partial r}\right) = 0. \tag{5.5}$$

The slip condition is (1.1) evaluated for the three-dimensional axisymmetric coordinates and has been used by others, including Greenspan[35] and Haley and Miksis[37]. Our slip function is

$$\lambda(h) = \frac{\lambda_1}{h}, \tag{5.6}$$

which was first introduced by Greenspan[35].

At the free boundary, $z = h(r, t)$, the governing equations are the kinematic condition

$$\frac{\partial h}{\partial t} + u\frac{\partial h}{\partial r} - w = 0, \tag{5.7}$$

and the jump in normal stress condition

$$p = p_a - \sigma \frac{1}{r}\frac{\partial}{\partial r}\left\{ r\frac{\partial h}{\partial r}\left[1+\left(\frac{\partial h}{\partial r}\right)^2\right]^{-\frac{1}{2}}\right\} + 2\mu\left[1+\left(\frac{\partial h}{\partial r}\right)^{-1}\right]\left[\left(\frac{\partial h}{\partial r}\right)^2\frac{\partial u}{\partial r} - \frac{\partial h}{\partial r}\left(\frac{\partial u}{\partial z}+\frac{\partial w}{\partial r}\right)+\frac{\partial w}{\partial z}\right]. \quad (5.8)$$

Here p_a is the atmospheric pressure of the surrounding fluid and σ is the surface tension of the droplet. The other condition at the free surface boundary is the continuity of tangential stress condition. The general stress condition is

$$\hat{n}\cdot\boldsymbol{\tau} = -\sigma\left(\nabla_s\cdot\hat{n}\right)\hat{n} + \nabla_s\sigma \quad (5.9)$$

where the unit normal is

$$\hat{n} = \frac{<-h_r, 0, 1>}{\sqrt{1+h_r^2}}, \quad (5.10)$$

the unit tangent is

$$\hat{t} = \frac{<1, 0, h_r>}{\sqrt{1+h_r^2}}, \quad (5.11)$$

the stress tensor is

$$\tau_{ij} = -p\delta_{ij} + \mu e_{ij}, \quad (5.12)$$

and ∇_s is the surface derivative in the direction of the tangent. The gradient is given by[51]

$$\nabla_s f = \frac{<1, 0, h_r>}{1+(h_r)^2}\frac{\partial f}{\partial r}. \quad (5.13)$$

Now $\hat{t}$ can be dotted into (5.9) to pick out the continuity of tangential stress condition,

$$\hat{n}\cdot\boldsymbol{\tau}\cdot\hat{t} = -\sigma\left(\nabla_s\cdot\hat{n}\right)\hat{n}\cdot\hat{t} + \nabla_s\sigma\cdot\hat{t}. \quad (5.14)$$

Simplifying and then expanding terms gives us:

$$\hat{n}\cdot\boldsymbol{\tau}\cdot\hat{t} = \nabla_s\sigma\cdot\hat{t} \quad (5.15)$$

$$\begin{aligned}
\hat{n}\cdot\boldsymbol{\tau}\cdot\hat{t} &= n_r\tau_{rr}t_r + n_r\tau_{rz}t_z + n_z\tau_{zr}t_r + n_z\tau_{zz}t_z \\
&= \frac{1}{1+(\frac{\partial h}{\partial r})^2}\Bigg[-\frac{\partial h}{\partial r}\left(-p+\mu\frac{\partial u}{\partial r}\right) - \frac{\partial h}{\partial r}\frac{\mu}{2}\left(\frac{\partial u}{\partial z}+\frac{\partial w}{\partial r}\right)\frac{\partial h}{\partial r} \\
&\quad + \frac{\mu}{2}\left(\frac{\partial u}{\partial z}+\frac{\partial w}{\partial r}\right) + \left(-p+\mu\frac{\partial w}{\partial r}\right)\frac{\partial h}{\partial r}\Bigg] \\
&= \frac{\mu}{1+(\frac{\partial h}{\partial r})^2}\Bigg[\frac{\partial h}{\partial r}\left(\frac{\partial w}{\partial z}-\frac{\partial u}{\partial r}\right) \\
&\quad + \frac{1}{2}\left(1-\left(\frac{\partial h}{\partial r}\right)^2\right)\left(\frac{\partial u}{\partial z}+\frac{\partial w}{\partial r}\right)\Bigg] \\
= \nabla_s\sigma\cdot\hat{t} &= \frac{\partial\sigma}{\partial r}\frac{1}{\sqrt{1+(\frac{\partial h}{\partial r})^2}}
\end{aligned} \tag{5.16}$$

Simplifying once again leads us to the continuity of tangential stress condition:

$$\mu\left[\frac{\partial h}{\partial r}\left(\frac{\partial w}{\partial z}-\frac{\partial u}{\partial r}\right)+\frac{1}{2}\left(1-\left(\frac{\partial h}{\partial r}\right)^2\right)\left(\frac{\partial u}{\partial z}+\frac{\partial w}{\partial r}\right)\right] = \sqrt{1+(\frac{\partial h}{\partial r})^2}\frac{\partial\sigma}{\partial r}. \tag{5.17}$$

Boundary conditions for the contact line are still needed. The slip velocity is defined to be the velocity of the contact line:

$$u_s = \frac{dR}{dt}. \tag{5.18}$$

The slip velocity is set equal to a general function of the contact angle, which is the contact angle – slip velocity relationship,

$$u_s = f(\theta). \tag{5.19}$$

A contact angle – slip velocity relationship that includes hysteresis effects is given by:

$$f(\theta) = \hat{k}\begin{cases} (\theta-\theta_{Adv}), & \theta > \theta_{Adv} \\ 0, & \theta_{Rec} \le \theta \le \theta_{Adv} \\ (\theta-\theta_{Rec}), & \theta < \theta_{Rec}. \end{cases} \tag{5.20}$$

Here $\hat{k}$ is a characteristic unit of velocity. This is the $m = 1$ form of (1.2)–(1.3) extended to allow for hysteresis. It has been used by, among others, Greenspan[35] and Haley and Miksis[37].

The droplet must remain in contact with the surface at the contact line and thus requires that

$$h(R(t),t) = 0. \tag{5.21}$$

Geometric analysis shows that

$$\left.\frac{\partial h}{\partial r}\right|_{r=R(t)} = -\tan(\theta). \tag{5.22}$$

The other main component of our model is the inclusion of surfactants. The concentration of surfactant on the surface of the droplet is given by $S(r,t)$. The general surfactant transport equation is

$$S_t + \nabla_s \cdot (\vec{u}_s S) - (\nabla_s \cdot \hat{n})\, S\, (\vec{u} \cdot \hat{n}) = D\nabla_s^2 S + J \tag{5.23}$$

where D is the surface diffusivity constant, $\vec{u}_s$ is the surface velocity (velocity in the tangential direction), $\hat{n}$ is the unit normal vector to the surface, and J is the surface absorption term, which will be ignored for this analysis. The surface divergence is given by

$$\nabla_s \cdot (\vec{u}_s S) = \frac{1}{r\sqrt{1+\left(\frac{\partial h}{\partial r}\right)^2}} \frac{\partial}{\partial r}\left(r u_s S\right) \tag{5.24}$$

where

$$u_s = \vec{v} \cdot \hat{t}. \tag{5.25}$$

One boundary condition for surfactant is that it must maintain symmetry at the origin:

$$\left.\frac{\partial S}{\partial r}\right|_{r=0} = 0. \tag{5.26}$$

Surfactant is allowed to be adsorbed and desorbed at the contact line. This is done by assuming that the gradient of S is linearly related to the surfactant concentration at the contact point. In particular, the boundary condition for surfactant transport is given by

$$\left.\frac{\partial S}{\partial r}\right|_{r=R} = -S_T\sqrt{1+\left(\frac{\partial h}{\partial r}\right)^2}\left(S\big|_{r=R} - S_S\right), \tag{5.27}$$

where S_T is the transfer rate of surfactant onto and off of the substrate and S_S is the steady concentration of surfactant on the substrate. It is assumed that S_T and S_S are constants independent of time. Remaining constant implies that if surfactant were absorbed by the advancing contact line, the resulting surface surfactant concentration would not affect the receding contact line if it were to transverse the same point on the substrate. No-flux at the contact lines can be modeled by taking $S_T = 0$. Equation

(5.27) is clearly a modeling assumption on our part, but it appears to be reasonable since the surfactant flux might be expected to increase as the local value of surfactant concentration increases.

We will also need an equation of state, which we take to be

$$\sigma = 1 + \epsilon^2 \Sigma \tag{5.28}$$

where $\epsilon \ll 1$ and Σ is given by

$$\Sigma = -\sigma_S S. \tag{5.29}$$

Here σ_S is a constant representing how strongly surfactants affect surface tension and has units of $J/mol\ m$.

Finally, the volume of the fluid droplet and the amount of surfactant on it are both constant in time and can be represented as

$$V_F = 2\pi \int_0^{R(t)} rh(r,t)dr, \tag{5.30}$$

$$V_S = 2\pi \int_0^{R(t)} rS(r,t)\sqrt{1 + \left(\frac{\partial h}{\partial r}\right)^2}\, dr. \tag{5.31}$$

5.2 Nondimensionalization

Here will nondimensionalize the evolution equations. The basic assumption of lubrication theory is that the height of the droplet is much less than its height. This assumption will be used to scale the nondimensional variables. The lubrication relationship also implies that the contact angle is small. The dimensional contact angle θ is used to define our small parameter $\epsilon \ll 1$. This scaling is used to scale our nondimensional variables, denoted by tildes:

$$
\begin{aligned}
t &= \frac{\tilde{t} R_c \mu}{\sigma_c \epsilon^3}, & r &= \tilde{r} R_c, & z &= \tilde{z} R_c \epsilon, \\
u &= \tilde{u} \hat{k} \epsilon, & w &= \tilde{w} \hat{k} \epsilon^2, & \theta &= \tilde{\theta} \epsilon, \\
\theta_{Adv} &= \epsilon \tilde{\theta}_{Adv}, & \theta_{Rec} &= \epsilon \tilde{\theta}_{Rec}, & \lambda &= R_c \epsilon \tilde{\lambda} \\
p &= \frac{\tilde{p} \mu \hat{k}}{R_c \epsilon} + p_A, & R &= \tilde{R} R_c, & \lambda_1 &= R_c^2 \epsilon^2 \tilde{\lambda}_1 \\
V_F &= \tilde{V}_F 2\pi R_c^3 \epsilon, & \sigma &= \sigma_c \tilde{\sigma}, & h &= \tilde{h} R_c \epsilon \\
V_S &= \tilde{V}_S 2\pi R_c^2 S_c, & \lambda_0 &= \tilde{\lambda}_0 R_c \epsilon, & S &= \tilde{S} S_c, \\
\Sigma &= \sigma_c \tilde{\Sigma}, & S_T &= \tilde{S}_T \frac{R_c}{S_c}, & S_S &= \tilde{S}_S \frac{R_c}{S_c}, \\
f &= \epsilon \hat{k} \tilde{f}.
\end{aligned}
$$

Here R_c is taken to be a characteristic length of the droplet, either an initial radius or a steady state radius, for example. The constant σ_c is the surface tension of a clean surface, which occurs when there is no surfactant on the droplet. The constant S_c is a characteristic surfactant concentration. We choose z to be one order of magnitude in ϵ smaller than r since that is consistent with the lubrication approximation that the height of droplet is much less than its width. Scalings for the velocities are chosen by examining the contact angle – slip velocity relationship (5.20) when substituted into (5.19). This gives a scaling for u and, because of (5.1), the vertical direction z is again chosen to be one order of magnitude smaller.

Also introduce the Capillary number, Ca, the Bond number, B, the Reynolds number, Re, the Peclet number, Pe, the Marangoni number for surfactant, M_S, and the parameter β representing the strength of the effect of surfactant gradients on surface tension:

$$
\begin{aligned}
Ca &= \frac{\mu \hat{k}}{\sigma_c \epsilon^2}, & B &= \frac{\rho g R_c^2}{\sigma_c}, & Re &= \frac{\rho R_c \hat{k}}{\mu}, \\
Pe &= \frac{R_c \hat{k} \epsilon}{D}, & M_S &= \frac{\sigma_c \beta \epsilon^2}{\mu \hat{k}}, & \beta &= \frac{S_c \sigma_S}{\sigma_c}.
\end{aligned}
$$

All of these parameters are assumed to be order one.

Rescaling the conservation of mass equation (5.1) for these new nondimen-

sional variables, we get

$$\frac{1}{\tilde{r}}\frac{\partial}{\partial\tilde{r}}(\tilde{r}\tilde{u}) + \frac{\partial\tilde{w}}{\partial\tilde{z}} = 0. \tag{5.32}$$

Using these scalings and nondimensional parameters in (5.2) gives us

$$Re\,\epsilon^3\left(\frac{1}{Ca}\frac{\partial\tilde{u}}{\partial\tilde{t}} + \tilde{u}\frac{\partial\tilde{u}}{\partial\tilde{r}} + \tilde{w}\frac{\partial\tilde{u}}{\partial\tilde{z}}\right) + \frac{\partial\tilde{p}}{\partial\tilde{r}} = \frac{\partial^2\tilde{u}}{\partial\tilde{z}^2} + \epsilon^2\left[\frac{1}{r}\frac{\partial}{\partial\tilde{r}}\left(\tilde{r}\frac{\partial\tilde{u}}{\partial\tilde{r}}\right) - \frac{\tilde{u}}{\tilde{r}^2}\right]. \tag{5.33}$$

The conservation of momentum in z equation (5.3) now becomes

$$\frac{\partial\tilde{p}}{\partial\tilde{z}} + \epsilon^5 Re\left(\frac{1}{Ca}\frac{\partial\tilde{w}}{\partial\tilde{t}} + \tilde{u}\frac{\partial\tilde{u}}{\partial\tilde{r}} + \tilde{w}\frac{\partial\tilde{u}}{\partial\tilde{z}}\right) = \epsilon^4\frac{1}{\tilde{r}}\frac{\partial}{\partial\tilde{r}}\left(\tilde{r}\frac{\partial\tilde{w}}{\partial\tilde{r}}\right) + \epsilon^2\frac{\partial^2\tilde{w}}{\partial\tilde{z}^2} - \frac{B}{Ca}. \tag{5.34}$$

At $\tilde{z} = 0$, the no penetration condition becomes

$$\tilde{w} = 0 \tag{5.35}$$

while the Navier slip law is

$$\tilde{u} - \tilde{\lambda}(\tilde{h})\left(\frac{\partial^2\tilde{u}}{\partial\tilde{z}^2} + \epsilon^2\frac{\partial^2\tilde{w}}{\partial\tilde{r}^2}\right), \tag{5.36}$$

with

$$\tilde{\lambda}(\tilde{h}) = \frac{\tilde{\lambda}_1}{\tilde{h}}. \tag{5.37}$$

At the boundary of the droplet, $\tilde{z} = \tilde{h}(\tilde{r},\tilde{t})$, the kinematic condition is

$$\frac{1}{Ca}\frac{\partial\tilde{h}}{\partial\tilde{t}} + \tilde{u}\frac{\partial\tilde{h}}{\partial\tilde{r}} - \tilde{w} = 0. \tag{5.38}$$

The jump in normal stress is now

$$\tilde{p} = -\frac{1}{Ca}\frac{1}{\tilde{r}}\frac{\partial}{\partial\tilde{r}}\left[\frac{\tilde{r}\frac{\partial\tilde{h}}{\partial\tilde{r}}}{\sqrt{1+\epsilon^2\left(\frac{\partial\tilde{h}}{\partial\tilde{r}}\right)^2}}\right] + \frac{2\epsilon^2}{1+\epsilon^2\left(\frac{\partial\tilde{h}}{\partial\tilde{r}}\right)^2}\left\{\frac{\partial\tilde{w}}{\partial\tilde{z}} - \frac{\partial\tilde{h}}{\partial\tilde{r}}\frac{\partial\tilde{u}}{\partial\tilde{z}} + \epsilon^2\left[\frac{\partial\tilde{u}}{\partial\tilde{r}}\left(\frac{\partial\tilde{h}}{\partial\tilde{r}}\right)^2 - \frac{\partial\tilde{h}}{\partial\tilde{r}}\frac{\partial\tilde{w}}{\partial\tilde{r}}\right]\right\}. \tag{5.39}$$

The equation of state will be used in the continuity of tangential stress condition, so we will nondimensionalize it first:

$$\tilde{\Sigma} = -\beta\tilde{S}. \tag{5.40}$$

The continuity of tangential stress condition now becomes

$$\epsilon\frac{\partial\tilde{h}}{\partial\tilde{r}}\left(\epsilon\frac{\partial\tilde{w}}{\partial\tilde{z}}-\epsilon\frac{\partial\tilde{u}}{\partial\tilde{r}}\right)+\frac{1}{2}\left(1-\left(\epsilon\frac{\partial\tilde{h}}{\partial\tilde{r}}\right)^2\right)\left(\frac{\partial\tilde{u}}{\partial\tilde{z}}+\epsilon^2\frac{\partial\tilde{w}}{\partial\tilde{r}}\right)=\frac{1}{Ca}\sqrt{1+\epsilon^2(\frac{\partial\tilde{h}}{\partial\tilde{r}})^2}\frac{\partial\tilde{\Sigma}}{\partial\tilde{r}}. \tag{5.41}$$

At the contact line, combining (5.18) and (5.19), the contact angle – slip velocity relationship becomes

$$\frac{d\tilde{R}}{d\tilde{t}}=Ca\ \tilde{f}(\tilde{\theta}) \tag{5.42}$$

where

$$\tilde{f}(\tilde{\theta})=\begin{cases}\left(\tilde{\theta}-\tilde{\theta}_{Adv}\right), & \tilde{\theta}>\tilde{\theta}_{Adv}\\ 0, & \tilde{\theta}_{Rec}\le\tilde{\theta}\le\tilde{\theta}_{Adv}\\ \left(\tilde{\theta}-\tilde{\theta}_{Rec}\right), & \tilde{\theta}<\tilde{\theta}_{Rec}\end{cases} \tag{5.43}$$

The contact condition remains

$$\tilde{h}(\tilde{R},\tilde{t})=0 \tag{5.44}$$

and the geometric relationship is

$$\left.\frac{\partial\tilde{h}}{\partial\tilde{r}}\right|_{\tilde{r}=\tilde{R}(\tilde{t})}=-\frac{1}{\epsilon}\tan(\epsilon\tilde{\theta}). \tag{5.45}$$

The surfactant transport equation (5.23) is more involved will be nondimensionalized piecewise. First, the surfactant concentration is nondimensionalized as

$$S=S_c\tilde{S} \tag{5.46}$$

where S_c is a characteristic surfactant concentration. The unit vectors become

$$\hat{n}=\frac{<-\epsilon\tilde{h}_{\tilde{r}},0,1>}{\sqrt{1+\epsilon^2\tilde{h}_{\tilde{r}}^2}}, \tag{5.47}$$

$$\hat{t}=\frac{<1,0,\epsilon\tilde{h}_{\tilde{r}}>}{\sqrt{1+\epsilon^2\tilde{h}_{\tilde{r}}^2}}. \tag{5.48}$$

The surface divergence (5.24) is now

$$\nabla_s\cdot(\vec{u}_sS)=\frac{\epsilon\hat{k}S_c}{R_c}\frac{1}{\tilde{r}\sqrt{1+\left(\epsilon\frac{\partial\tilde{h}}{\partial\tilde{r}}\right)^2}}\frac{\partial}{\partial\tilde{r}}\left(\frac{\tilde{u}+\epsilon^2\tilde{w}\frac{\partial\tilde{h}}{\partial\tilde{r}}}{\sqrt{1+\left(\epsilon\frac{\partial\tilde{h}}{\partial\tilde{r}}\right)^2}}\tilde{r}\tilde{S}\right). \tag{5.49}$$

The surface Laplacian is given by

$$\nabla_s^2 = \frac{S_c}{R_c^2}\frac{1}{r\sqrt{1+\left(\epsilon\frac{\partial\tilde{h}}{\partial\tilde{r}}\right)^2}}\frac{\partial}{\partial\tilde{r}}\left(\frac{r}{\sqrt{1+\left(\epsilon\frac{\partial\tilde{h}}{\partial\tilde{r}}\right)^2}}\frac{\partial\tilde{S}}{\partial\tilde{r}}\right) \tag{5.50}$$

The surfactant transport equation (5.23) now becomes

$$\begin{aligned}\frac{1}{Ca}\frac{\partial\tilde{S}}{\partial\tilde{t}} &+ \frac{1}{\tilde{r}\sqrt{1+\left(\epsilon\frac{\partial\tilde{h}}{\partial\tilde{r}}\right)^2}}\frac{\partial}{\partial\tilde{r}}\left(\frac{\tilde{u}+\epsilon^2\tilde{w}\frac{\partial\tilde{h}}{\partial\tilde{r}}}{\sqrt{1+\left(\epsilon\frac{\partial\tilde{h}}{\partial\tilde{r}}\right)^2}}\tilde{r}\tilde{S}\right)\\ &- \frac{1}{1+\left(\epsilon\frac{\partial\tilde{h}}{\partial\tilde{r}}\right)^2}\frac{1}{r}\frac{\partial}{\partial\tilde{r}}\left(\frac{\tilde{r}\frac{\partial\tilde{h}}{\partial\tilde{r}}}{\sqrt{1+\left(\epsilon\frac{\partial\tilde{h}}{\partial\tilde{r}}\right)^2}}\right)\tilde{S}\left(-\epsilon\tilde{u}\frac{\partial\tilde{h}}{\partial\tilde{r}}+\epsilon\tilde{w}\right)\\ &= \frac{1}{Pe}\frac{1}{\tilde{r}\sqrt{1+\left(\epsilon\frac{\partial\tilde{h}}{\partial\tilde{r}}\right)^2}}\frac{\partial}{\partial\tilde{r}}\left(\frac{\tilde{r}}{\sqrt{1+\left(\epsilon\frac{\partial\tilde{h}}{\partial\tilde{r}}\right)^2}}\frac{\partial\tilde{S}}{\partial\tilde{r}}\right).\end{aligned} \tag{5.51}$$

The boundary conditions are the flux condition,

$$\left.\frac{\partial\tilde{S}}{\partial\tilde{r}}\right|_{\tilde{r}=\tilde{R}} = -\tilde{S}_T\sqrt{1+\left(\epsilon\frac{\partial\tilde{h}}{\partial\tilde{r}}\right)^2}\left(\tilde{S}\big|_{\tilde{r}=\tilde{R}}-\tilde{S}_S\right), \tag{5.52}$$

and the symmetry condition at the origin

$$\left.\frac{\partial\tilde{S}}{\partial\tilde{r}}\right|_{\tilde{r}=0} = 0. \tag{5.53}$$

Finally, the volume of fluid and amount of surfactant become

$$\tilde{V}_F = \int_0^{\tilde{R}}\tilde{r}\tilde{h}(\tilde{r},\tilde{t})d\tilde{r}, \tag{5.54}$$

$$\tilde{V}_S = \int_0^{\tilde{R}}\tilde{r}\tilde{S}(\tilde{r},\tilde{t})\sqrt{1+\left(\epsilon\frac{\partial\tilde{h}}{\partial\tilde{r}}\right)^2}d\tilde{r}. \tag{5.55}$$

5.3 Leading Order Equations

Now that we have derived the nondimensional equations for the system, we can go about finding the leading order in ϵ terms. Introduce a regular perturbation

expansion of the form $\tilde{h} = \tilde{h}_0 + \epsilon\tilde{h}_1 + \ldots$ for each of the dependent variables. Substitutes this expansion into equations (5.32)–(5.53) and group together terms of like order in ϵ. At leading order, the conservation of mass equation remains unchanged as

$$\frac{1}{\tilde{r}}\frac{\partial}{\partial\tilde{r}}(\tilde{r}\tilde{u}_0) + \frac{\partial\tilde{w}_0}{\partial\tilde{z}} = 0. \tag{5.56}$$

The leading order of conservation of momentum leading in r is

$$\frac{\partial\tilde{p}_0}{\partial\tilde{r}} = \frac{\partial^2\tilde{u}_0}{\partial\tilde{z}^2}. \tag{5.57}$$

while in conservation of momentum in z it is

$$\frac{\partial\tilde{p}_0}{\partial\tilde{z}} = -\frac{B}{Ca}. \tag{5.58}$$

At the substrate $\tilde{z} = 0$, the no penetration condition (5.35) remains unchanged as

$$\tilde{w}_0\Big|_{\tilde{z}=0} = 0. \tag{5.59}$$

The slip law (5.36) becomes

$$\tilde{u}_0 - \tilde{\lambda}(\tilde{h}_0)\frac{\partial\tilde{u}_0}{\partial\tilde{z}} = 0. \tag{5.60}$$

On the free surface, $\tilde{z} = \tilde{h}_0(\tilde{r},\tilde{t})$, the kinematic condition (5.7) reduces to

$$\frac{1}{Ca}\frac{\partial\tilde{h}_0}{\partial\tilde{t}} + \tilde{u}_0\frac{\partial\tilde{h}_0}{\partial\tilde{r}} - \tilde{w}_0 = 0. \tag{5.61}$$

The continuity of tangential stress condition (5.41) reduces to

$$\frac{\partial\tilde{u}_0}{\partial\tilde{z}} = \frac{2}{Ca}\frac{\partial}{\partial\tilde{r}}\tilde{\Sigma}_0. \tag{5.62}$$

The jump in normal stress (5.39) becomes

$$\tilde{p}_0 = -\frac{1}{Ca}\frac{1}{\tilde{r}}\frac{\partial}{\partial\tilde{r}}\left(\tilde{r}\frac{\partial\tilde{h}_0}{\partial\tilde{r}}\right). \tag{5.63}$$

Expanding the geometric relation (5.45) for $\epsilon \ll 1$ produces

$$\frac{\partial\tilde{h}_0}{\partial\tilde{r}}\Big|_{\tilde{r}=\tilde{R}} = -\tilde{\theta}_0. \tag{5.64}$$

Combining this result with (5.42) yields

$$\frac{1}{Ca}\frac{d\tilde{R}_0}{d\tilde{t}} = \tilde{f}\left(-\frac{\partial \tilde{h}_0}{\partial \tilde{r}}\bigg|_{\tilde{r}=\tilde{R}}\right). \tag{5.65}$$

The surfactant evolution equation at leading order is

$$\frac{1}{Ca}\frac{\partial \tilde{S}_0}{\partial \tilde{t}} + \frac{1}{\tilde{r}}\frac{\partial}{\partial \tilde{r}}\left(\tilde{r}\tilde{u}_0\tilde{S}_0\right) = \frac{1}{Pe}\frac{1}{\tilde{r}}\frac{\partial}{\partial \tilde{r}}\left(\tilde{r}\frac{\partial \tilde{S}_0}{\partial \tilde{r}}\right) \tag{5.66}$$

while the boundary conditions become The boundary conditions are the flux condition,

$$\frac{\partial \tilde{S}_0}{\partial \tilde{r}}\bigg|_{\tilde{r}=\tilde{R}} = -\tilde{S}_T\left(\tilde{S}_0\big|_{\tilde{r}=\tilde{R}} - \tilde{S}_S\right), \tag{5.67}$$

and the symmetry condition at the origin

$$\frac{\partial \tilde{S}_0}{\partial \tilde{r}}\bigg|_{\tilde{r}=0} = 0. \tag{5.68}$$

Finally, the amount of surfactant on the drop is given by

$$\tilde{V}_S = \int_0^{\tilde{R}} \tilde{r}\tilde{S}_0(\tilde{r},\tilde{t})d\tilde{r}. \tag{5.69}$$

We will now drop the tildes over and subscripts to the nondimensional variables.

5.4 Derivation of Evolution Equations

A set of linked partial differential equations for droplet height, contact line motion, and surfactant concentration will now be derived from the leading order nondimensional equations. Integrating (5.58) with respect to z reveals that

$$p = -\frac{B}{Ca}z + \frac{1}{Ca}q(r,t). \tag{5.70}$$

Using this result in (5.63) gives

$$q(r,t) = Bh - \frac{1}{r}\frac{\partial}{\partial r}\left(r\frac{\partial h}{\partial r}\right). \tag{5.71}$$

Substituting (5.70) and (5.71) in (5.57) produces

$$\frac{1}{Ca}\frac{\partial q}{\partial r} = \frac{\partial^2 u}{\partial z^2}, \tag{5.72}$$

which can be integrated twice to find

$$u = \frac{1}{Ca}\frac{\partial q}{\partial r}\frac{z^2}{2} + A(r,t)z + C(r,t). \tag{5.73}$$

Use this result in (5.62) and see that

$$A(r,t) = \frac{2}{Ca}\frac{\partial \Sigma}{\partial r} - \frac{1}{Ca}\frac{\partial q}{\partial r}h. \tag{5.74}$$

Now, use (5.73) and (5.74) in (5.60) to solve for C:

$$C(r,t) = \lambda(h)A(r,t) = \frac{1}{Ca}\lambda(h)\left(2\frac{\partial \Sigma}{\partial r} - \frac{\partial q}{\partial r}h\right). \tag{5.75}$$

Substitute (5.73) - (5.75) into (5.56):

$$\frac{1}{r}\frac{\partial}{\partial r}(ru) + \frac{\partial w}{\partial z} = 0. \tag{5.76}$$

Now, integrate this one time with respect to z to solve for w:

$$\begin{aligned} w &= -\frac{1}{r}\frac{\partial}{\partial r}\left(r\int u dz\right) + D(r,t) \\ &= -\frac{1}{Ca}\frac{1}{r}\frac{\partial}{\partial r}\Bigg\{r\Bigg[\frac{\partial q}{\partial r}\frac{z^3}{6} + \left(2\frac{\partial \Sigma}{\partial r} - \frac{\partial q}{\partial r}h\right)\frac{z^2}{2} \\ &\qquad + \lambda(h)\left(2\frac{\partial \Sigma}{\partial r} - \frac{\partial q}{\partial r}h\right)z\Bigg]\Bigg\} + D(r,t) \end{aligned} \tag{5.77}$$

$$\begin{aligned} w = \frac{1}{Ca}\frac{1}{r}\frac{\partial}{\partial r}\left[r\frac{\partial q}{\partial r}\left(\frac{z^2}{2}h - \frac{z^3}{6} + \lambda(h)zh\right) - 2r\frac{\partial \Sigma}{\partial r}\left(\frac{z^2}{2} + \lambda(h)z\right)\right] \\ + D(r,t). \end{aligned} \tag{5.78}$$

Use (5.73) - (5.77) in (5.59) and solve for $D(r,t)$:

$$D(r,t) = 0 \tag{5.79}$$

Finally, substitute (5.73) - (5.79) into (5.61) to get a partial differential equation for $h(r,t)$:

$$\begin{aligned}
&\left(\frac{1}{Ca}\frac{\partial h}{\partial t}+u\frac{\partial h}{\partial r}-w\right)\Bigg|_{z=h}=0\\
&\frac{1}{Ca}\frac{\partial h}{\partial t}+\frac{r}{Ca}\left[\frac{\partial q}{\partial r}\frac{h^2}{2}+\left(2\frac{\partial \Sigma}{\partial r}-\frac{\partial q}{\partial r}h\right)(h+\lambda(h))\right]\frac{\partial h}{\partial r}\\
&\quad-\frac{1}{r}\frac{\partial}{\partial r}\left(\frac{r}{Ca}\frac{\partial q}{\partial r}\right)\left[\frac{h}{3}+\lambda(h)h^2\right]-\frac{1}{Ca}\frac{\partial q}{\partial r}\left[\frac{h^2}{2}\frac{\partial h}{\partial r}+\frac{\partial}{\partial r}(h\lambda(h))\,h\right]\\
&\quad+\frac{2}{Ca}\frac{1}{r}\frac{\partial \Sigma}{\partial r}\left[\frac{h^2}{2}+\lambda(h)h\right]+\frac{2}{Ca}\frac{\partial^2\Sigma}{\partial r^2}\left[\frac{h^2}{2}+\lambda(h)h\right]\\
&\quad+\frac{2}{Ca}\frac{\partial \Sigma}{\partial r}\frac{\partial}{\partial r}(\lambda(h))\,h=0
\end{aligned}\tag{5.80}$$

which simplifies down to

$$\frac{\partial h}{\partial t}=\frac{1}{r}\frac{\partial}{\partial r}\left(W\frac{\partial q}{\partial r}-V\frac{\partial \Sigma}{\partial r}\right)\tag{5.81}$$

where

$$W=r\left[\frac{h^3}{3}+\lambda(h)h^2\right],\tag{5.82}$$

$$V=2r\left[\frac{h^2}{2}+\lambda(h)h\right].\tag{5.83}$$

It should be noted that h still needs boundary conditions at the origin. Smoothness at the origin requires that

$$\left.\frac{\partial h}{\partial r}\right|_{r=0}=0.\tag{5.84}$$

One more boundary condition is still needed. This is found via a local analysis of (5.98). In order for the height to remain bounded at the origin, we require that

$$\left.\frac{\partial^3 h}{\partial r^3}\right|_{r=0}=0.\tag{5.85}$$

Taken together, (5.81)–(5.83) with boundary conditions (5.44) and (5.84)–(5.85) form the droplet height evolution equation, the contact line is advanced by (5.65), and the surfactant concentration is determined by (5.66) with boundary conditions (5.67) and (5.68).

5.5 Volume Conservation

Volume is automatically conserved in this formulation of the problem. Fluid volume is given by

$$V_F = \int_0^{R(t)} h(r,t)\ r\ dr. \tag{5.86}$$

Volume conservation is proved by showing that the change in volume in time is zero:

$$\frac{dV_F}{dt} = \dot{R}(t) h\ r\Big|_{r=R} + \int_0^{R(t)} \frac{\partial h}{\partial t} r dr. \tag{5.87}$$

The contact condition (5.44) is used to reduce this to

$$\begin{aligned}
\frac{dV_F}{dt} &= \int_0^R \frac{\partial h}{\partial t} r dr && (5.88)\\
&= \int_0^R \frac{\partial}{\partial r}\left(W\frac{\partial q}{\partial r} - V\frac{\partial \Sigma}{\partial r}\right) dr && (5.89)\\
&= \left(W\frac{\partial q}{\partial r} - V\frac{\partial \Sigma}{\partial r}\right)\Big|_{r=0}^{r=R} && (5.90)
\end{aligned}$$

It can be shown that $\frac{\partial q}{\partial r}\big|_0 = 0$ and that W is zero at the contact line. This means that

$$\frac{dV_F}{dt} = 0. \tag{5.91}$$

As with the volume of the droplet, it will now be shown that surfactant is automatically conserved in this formulation of the problem. At leading order, the total amount of surfactant on the drop is given by (5.69). As before, conservation of surfactant will be proved by showing that the change in total surfactant in time is zero.

$$\begin{aligned}
\frac{dV_S}{dt} &= \frac{\partial}{\partial t}\int_0^{R(t)} S(r,t)\ r\ dr && (5.92)\\
&= \dot{R} S\ r\Big|_{r=R} + \int_0^R \frac{\partial S}{\partial t} r dr && (5.93)\\
&= \dot{R} S\ r\Big|_{r=R} + Ca\int_{r=0}^{r=R} \frac{\partial}{\partial r}\left(\frac{r}{Pe}\frac{\partial S}{\partial r} - r\ u\ S\right) dr && (5.94)\\
&= \dot{R}\ S\ r\Big|_{r=R} + Ca\left(\frac{r}{Pe}\frac{\partial S}{\partial r} - r\ u\ S\right)\Big|_{r=0}^{r=R} && (5.95)
\end{aligned}$$

Now, $\frac{\partial S}{\partial r}\big|_{r=0} = 0$ by (5.53) and symmetry requires that $u\big|_{r=0} = 0$ and $\dot{R} = Ca\ u\big|_{r=R}$. This allows the formulation to be reduced to

$$\frac{dS}{dt} = R\frac{Ca}{Pe}\frac{\partial S}{\partial r}\Big|_R. \tag{5.96}$$

If there is a no-flux condition at the boundary, $S_T = 0$, then

$$\frac{dS}{dt} = 0. \tag{5.97}$$

If, however, there is a non-zero flux, then (5.96) represents how much surfactant transfers to or from the surface onto the substrate and demonstrates that the amount of surfactant on the droplet is time dependent.

5.6 Summary

We will now summarize the governing equations. The droplet evolution equation is given by:

$$\frac{\partial h}{\partial t} = \frac{1}{r}\frac{\partial}{\partial r}\left(W\frac{\partial q}{\partial r} - V\frac{\partial \Sigma}{\partial r}\right) \tag{5.98}$$

where

$$W = r\left[\frac{h^3}{3} + \lambda(h)h^2\right], \tag{5.99}$$

$$V = 2r\left[\frac{h^2}{2} + \lambda(h)h\right], \tag{5.100}$$

$$q(r,t) = Bh - \frac{1}{r}\frac{\partial}{\partial r}\left(r\frac{\partial h}{\partial r}\right), \tag{5.101}$$

$$\Sigma = -\beta S \tag{5.102}$$

$$\lambda(h) = \frac{\lambda_1}{h}. \tag{5.103}$$

The boundary conditions on height are:

$$\tilde{h}(\tilde{R},\tilde{t}) = 0, \tag{5.104}$$

$$\left.\frac{\partial h}{\partial r}\right|_{r=0} = 0, \tag{5.105}$$

$$\left.\frac{\partial^3 h}{\partial r^3}\right|_{r=0} = 0. \tag{5.106}$$

The surfactant evolution equation is:

$$\frac{1}{Ca}\frac{\partial S}{\partial t} + \frac{1}{r}\frac{\partial}{\partial r}(ruS) = \frac{1}{Pe}\frac{1}{r}\frac{\partial}{\partial r}\left(r\frac{\partial S}{\partial r}\right). \tag{5.107}$$

where

$$u = -\frac{1}{Ca}\frac{\partial q}{\partial r}\frac{h^2}{2} + \frac{2}{Ca}\frac{\partial \Sigma}{\partial r}h + \frac{1}{Ca}\lambda(h)\left(2\frac{\partial \Sigma}{\partial r} - \frac{\partial q}{\partial r}h\right) \tag{5.108}$$

and the surfactant boundary conditions are

$$\left.\frac{\partial S}{\partial r}\right|_{r=R} = -S_T\left(S\big|_{r=R} - S_S\right), \tag{5.109}$$

$$\left.\frac{\partial S}{\partial r}\right|_{r=0} = 0. \tag{5.110}$$

Finally, the contact line is advanced by

$$\frac{1}{Ca}\frac{dR}{dt} = f\left(-\left.\frac{\partial h}{\partial r}\right|_{r=R}\right) \tag{5.111}$$

with

$$f(\theta) = \begin{cases} (\theta - \theta_{Adv}), & \theta > \theta_{Adv} \\ 0, & \theta_{Rec} \leq \theta \leq \theta_{Adv} \\ (\theta - \theta_{Rec}), & \theta < \theta_{Rec} \end{cases}. \tag{5.112}$$

5.7 Steady State Solution

Here the steady state solutions of the problems are derived under the $\beta = 0$ limit, so there is no interaction between the surfactant and the droplet. By evaluating the steady state version of (5.98), it is seen that

$$0 = \frac{\partial}{\partial r}\left(W\frac{\partial q}{\partial r}\right). \tag{5.113}$$

We can not set $W = 0$ for an arbitrary slip law λ, thus the steady state equation reduces to

$$\begin{aligned} &\frac{\partial q}{\partial r} = 0, \\ &Bh - \frac{\sigma}{r}\frac{\partial}{\partial r}\left(r\frac{\partial h}{\partial r}\right) = A, \end{aligned} \tag{5.114}$$

where A is some constant.

For the $B = 0$ limit, the solution to this problem, with the appropriate boundary conditions, is

$$h = \frac{\theta_S R_S}{2}\left(1 - \left(\frac{r}{R_s}\right)^2\right), \tag{5.115}$$

with θ_S and R_S being the static contact angle and radius.

If $B \neq 0$, then the solution is

$$h = \frac{\theta_S}{\sqrt{B} I_1(\sqrt{B} R_S)} \left[I_0(\sqrt{B} R_S) - I_0(\sqrt{B} r) \right] \tag{5.116}$$

where I_0 and I_1 are the modified Bessel functions of order 0 and 1.

For any value of Bond number, the only steady state solution for surfactant is a constant.

Chapter 6

Three-Dimensional Axisymmetric Numerical Method

The droplet evolution equation, (5.98), subject to boundary conditions (5.104) and (5.105)–(5.106), the surfactant transport equation, (5.107), subject to boundary conditions (5.109) and (5.110), and the radii evolution equation (5.111) are solved using a numerical method employing backward Euler time stepping and Chebyshev pseudo-spectral spatial derivatives. The Chebyshev scheme has the advantage that it bunches points near the contact lines, where the dynamics are the most sensitive. The resulting nonlinear system is then solved by Newton's method. Although the method is only first order in time, it is extremely robust. Unlike the two-dimensional results, we do not need to analytically remove the singularity that exists near the contact line because we are not dealing with temperature effects. Also, unlike the two-dimensional method, we use a singular slip coefficient of the form λ_1/h instead of constant slip.

6.1 Conversion into Chebyshev Space

In order to use Chebyshev derivatives, we must convert our problem from real space into Chebyshev space. We start with a rescaling of the parameters. We need to map the domain of the problem from $r \in [0, R]$ onto $\xi \in [-1, 1]$.

$$r = \frac{R}{2}(\xi + 1), \tag{6.1}$$

$$h(r,t) = R(t)H(\xi,t), \tag{6.2}$$

$$S(r,t) = R(t)\tilde{S}(\xi,t), \tag{6.3}$$

Since r is now a function of t, we need to redefine derivatives with respect to t as

$$\frac{\partial}{\partial t} = \frac{\partial}{\partial \tau} - \frac{\xi+1}{R}\frac{dR}{d\tau}\frac{\partial}{\partial \xi} \tag{6.4}$$

where $\tau = t$. We also need to redefine derivatives with respect to r as

$$\frac{\partial}{\partial r} = \frac{2}{R}\frac{\partial}{\partial \xi} \tag{6.5}$$

Combining (6.2) and (6.4) yields

$$\frac{\partial h}{\partial t} = \frac{dR}{d\tau}H + R\frac{\partial H}{\partial \tau} - (\xi+1)\frac{dR}{d\tau}\frac{\partial H}{\partial \xi}. \tag{6.6}$$

The droplet evolution equation, (5.98), now becomes

$$R\frac{\partial H}{\partial \tau} = -\frac{dR}{d\tau}H + (\xi+1)\frac{dR}{d\tau}\frac{\partial H}{\partial \xi} + \frac{4}{R(\xi+1)}\frac{\partial}{\partial \xi}\left(W\frac{\partial q}{\partial \xi} - V\frac{\partial \Sigma}{\partial \xi}\right) \tag{6.7}$$

where

$$W = R(\xi+1)\left(\frac{R}{3}H^3 + H^2\lambda(RH)\right) \tag{6.8}$$

$$V = 2(\xi+1)\left(\frac{R}{2}H^2 + \lambda(RH)H\right), \tag{6.9}$$

$$q = BRH - \frac{4}{R(\xi+1)}\frac{\partial}{\partial \xi}\left((\xi+1)\frac{\partial H}{\partial \xi}\right). \tag{6.10}$$

The surfactant transport equation, (5.107), becomes

$$\frac{1}{Ca}\frac{\partial \tilde{S}}{\partial \tau} + \frac{\partial R}{\partial \tau}\tilde{S} - \frac{\xi+1}{Ca}\frac{dR}{d\tau}\frac{\partial \tilde{S}}{\partial \xi} + \frac{2}{\xi+1}\frac{\partial}{\partial \xi}\left((\xi+1)u\tilde{S}\right) = \frac{4}{RPe(\xi+1)}\frac{\partial}{\partial \xi}\left((\xi+1)\frac{\partial \tilde{S}}{\partial \xi}\right) \tag{6.11}$$

where

$$u = -\frac{R}{Ca}\frac{\partial q}{\partial \xi}H^2 + \frac{4}{Ca}\frac{\partial \Sigma}{\partial \xi}H + \frac{2}{Ca}\lambda(RH)\left(\frac{1}{R}\frac{\partial \Sigma}{\partial \xi} - \frac{\partial q}{\partial \xi}H\right) \tag{6.12}$$

and

$$\Sigma = -\beta R\tilde{S}. \tag{6.13}$$

Finally, the contact line evolution equation, (5.111), is

$$\frac{\partial R}{\partial \tau} = Caf\left(-2\frac{\partial H}{\partial \xi}\bigg|_{\xi=1}\right). \tag{6.14}$$

Details of the Chebyshev pseudo-spectral method that is used to take the derivatives are given in Appendix B. One result of the distribution of Chebyshev collocation points is that it bunches points near the ends of the domain. This is fortuitous since it results in extra points near the contact line, where the dynamics occur on the shortest spatial scales.

6.2 Time Derivatives

We use a backward Euler method to advance the scheme in time. We march forward from timestep t^n to $t^{n+1} = t^n + \Delta t$. We construct a series of nonlinear equations for $H_i^{n+1} = H(\xi_i, t^{n+1}, t^n)$, $S_i^{n+1} = S(\xi_i, t^{n+1}, t^n)$, and $R^{n+1} = R(t^{n+1}, t^n)$ where ξ_i represents the value of ξ at the i^{th} Chebyshev collocation point. We then solve the resulting system via Newton's method. The resulting matrix is full. Using finite differences rather than a Chebyshev pseudo-spectral method to compute spatial derivatives would result in a sparse matrix, which would result in significant time savings when solving the nonlinear system. Unfortunately, in order to maintain a given level of accuracy, we would have to drastically increase the number of spatial gridpoints, which would result in a much larger matrix to invert, more than negating any time savings bought by using finite differences. The numerical scheme is give by

$$\begin{aligned} R^{n+1}\frac{H^{n+1}-H^n}{\Delta t} = &-\frac{R^{n+1}-R^n}{\Delta t}H^{n+1} + (\xi+1)\frac{R^{n+1}-R^n}{\Delta t}\frac{\partial H^{n+1}}{\partial \xi} \\ &+\frac{4}{R^{n+1}(\xi+1)}\frac{\partial}{\partial \xi}\left(W^{n+1}\frac{\partial q^{n+1}}{\partial \xi} - V^{n+1}\frac{\partial \Sigma^{n+1}}{\partial \xi}\right), \end{aligned} \tag{6.15}$$

$$\begin{aligned} &\frac{1}{Ca}\frac{\tilde{S}^{n+1}-\tilde{S}^n}{\Delta t} + \frac{R^{n+1}-R^n}{\Delta t}\tilde{S}^{n+1} - \frac{\xi+1}{Ca}\frac{R^{n+1}-R^n}{\Delta t}\frac{\partial \tilde{S}^{n+1}}{\partial \xi} \\ &\quad + \frac{2}{\xi+1}\frac{\partial}{\partial \xi}\left((\xi+1)u^{n+1}\tilde{S}^{n+1}\right) = \frac{4}{R^{n+1}Pe(\xi+1)}\frac{\partial}{\partial \xi}\left((\xi+1)\frac{\partial \tilde{S}^{n+1}}{\partial \xi}\right), \end{aligned} \tag{6.16}$$

and

$$\frac{R^{n+1}-R^n}{\Delta t} = Caf\left(-2\frac{\partial H^{n+1}}{\partial \xi}\bigg|_{\xi=1}\right). \tag{6.17}$$

6.3 Convergence Checks

The results of a spatial convergence check are given in Table 6.1. The same droplet configuration as in Chapter 7 is used, with no flux of surfactant allowed at the contact line. The simulation results are evaluated at $t = 10$ where $\Delta t = 10^{-4}$. As in the two-dimensional results, the number of spatial points is given by $2^n + 1$ and each "doubling" of the spatial points is performed by incrementing n by one each time. This does not give a perfect doubling, but it is consistent with the actual numerical scheme that is used to evaluate the derivatives. The columns give the difference in the volume of fluid, amount of surfactant, the concentration of surfactant at the contact line, and the location of the contact line. A similar convergence check for temporal convergence is given in Table 6.2. Here the timestep is varied from its base state of $\Delta t = 10^{-4}$ while a constant 33 collocation points are used.

Gridpoints	V_F Difference	V_S Difference	S_R Difference	R Difference
$9 \rightarrow 17$	$2.92 \cdot 10^{-1}$	$3.97 \cdot 10^{-1}$	$7.24 \cdot 10^{-2}$	$7.60 \cdot 10^{-2}$
$17 \rightarrow 33$	$8.86 \cdot 10^{-2}$	$9.52 \cdot 10^{-2}$	$1.56 \cdot 10^{-2}$	$2.20 \cdot 10^{-2}$
$33 \rightarrow 65$	$3.94 \cdot 10^{-3}$	$1.26 \cdot 10^{-2}$	$2.94 \cdot 10^{-3}$	$1.32 \cdot 10^{-4}$

Table 6.1: Three-dimensional axisymmetric spatial convergence

Timestep Change	V_F Difference	V_S Difference	S_R Difference	R Difference
$2 \rightarrow 1$	$3.58 \cdot 10^{-5}$	$2.98 \cdot 10^{-5}$	$3.16 \cdot 10^{-6}$	$1.13 \cdot 10^{-5}$
$1 \rightarrow 1/2$	$1.79 \cdot 10^{-5}$	$1.49 \cdot 10^{-5}$	$1.58 \cdot 10^{-6}$	$5.65 \cdot 10^{-6}$
$1/2 \rightarrow 1/4$	$8.95 \cdot 10^{-6}$	$7.44 \cdot 10^{-6}$	$7.91 \cdot 10^{-7}$	$2.83 \cdot 10^{-6}$
$1/4 \rightarrow 1/8$	$4.48 \cdot 10^{-6}$	$3.72 \cdot 10^{-6}$	$3.96 \cdot 10^{-7}$	$1.41 \cdot 10^{-6}$

Table 6.2: Three-dimensional axisymmetric time convergence

These convergence checks show that this three-dimensional axisymmetric numerical scheme is first order in time and spectrally accurate in space. Halving the timestep reduces the differences in all the measured quantities by half, as expected for a first order method. As shown in the first column of Table 6.2, the difference in the volume of fluid when the timestep is halved from twice the base value to the base

value is $3.58 \cdot 10^{-5}$. The difference in V_f when the timestep is halved again to half the base value is $1.79 \cdot 10^{-5}$, approximately half of the difference in the previous case.

In contrast, doubling the number of collocation points causes the differences in the quantities listed in Table 6.1 to decrease by increasing amounts, as expected with a spectrally accurate method. Doubling the number of gridpoints from 9 to 17 and from 17 to 33 resulted in differences in fluid volume V_F of 0.292 and 0.0886. The ratio between those two differences is 3.3. Doubling the number of gridpoints again from 33 to 65 resulted in a fluid volume difference of 0.00394. The ratio between the fluid volume differences for the 17 to 33 and 33 to 65 gridpoint cases is 22.5, significantly greater than the previous case. Comparing these ratios yields increasing differences, even in the case of the concentration of surfactant at the contact line, S_R. In this case, the ratio of the S_R differences for the 9 to 17 and 17 to 33 cases is 4.6. The ratio of the S_R differences for the 17 to 33 and 33 to 65 cases is 5.3.

Chapter 7

Three-Dimensional Axisymmetric Results

7.1 Introduction

Initial conditions for these runs are the same as in Chapter 4 as we will be comparing the two. The droplet is initialized the to steady state solution when gravitational effects are ignored, $B = 0$ and $\beta = 0$. The result is given by (5.115) and is reproduced here with the modification that instead of a steady state radius and steady contact angle, it includes an initial radius and contact angle, R_I and θ_I,

$$h = \frac{\theta_I R_I}{2}\left(1 - \left(\frac{r}{R_I}\right)^2\right). \tag{7.1}$$

The initial volume of this droplet is $V_I = (\pi/4)\theta_I R_I^3$. The following parameters are used unless otherwise noted: $R_I = 1, \beta = 1, Ca = 0.1, B = 1, Pe = 1$, and $\lambda = 0.01$. A wetting droplet is considered, where $\theta_{Adv} = \theta_{Rec} = 0$ and $\theta_I = 3$. The surfactant is initialized to a constant value of $S = 1/2$. All the figures are presented at $t = 10$. At longer times, the surfactant tends to reach a zero average concentration as the droplet wets the surface.

7.2 Results

Figure 7.1 shows the effect of surfactant on droplet spreading. For these runs, a no-flux condition ($S_T = 0$) has been used for surfactant at the contact line. The radius $R(t)$ at $t = 10$ is plotted versus β for different Peclet numbers. This graph is the analogue of Fig. 4.1 but in three dimensions. As one would hope, the

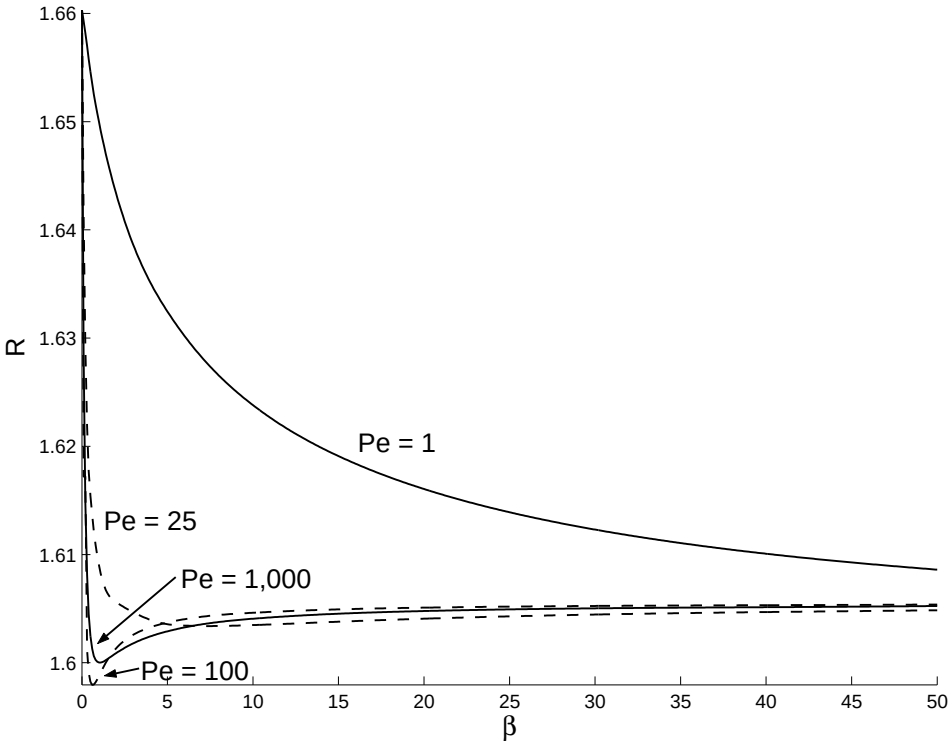

Figure 7.1: Effects of surfactant strength on spreading. Spreading distance versus β at $t = 10$. Note that increasing the strength of the surfactant reduces the spreading distance of the droplet.

results are quite similar. The same qualitative behavior persists from two to three dimensions. Overall, it is found that surfactants act to retard droplet spreading by forming negative surface tension gradients and opposing Marangoni flows. Higher Peclet numbers intensify these results by decreasing surfactant diffusion and allowing sharper gradients to persist. The minimum spreading distance that was discussed in Chapter 4 is also encountered in three dimensions. The minimum, while still small, is quite apparent for Peclet numbers of 100 or greater.

Surfactant profiles are shown in 7.2. This figure shows the surfactant concentration for both large and small Peclet numbers at $t = 10$ for a surfactant strength of $\beta = 2$. Contrary to visual inspection, both the no-flux condition and the symmetry condition at the origin are fulfilled. The Chebyshev derivatives use the values of the surfactant concentration over the entire domain to compute a derivative and do not

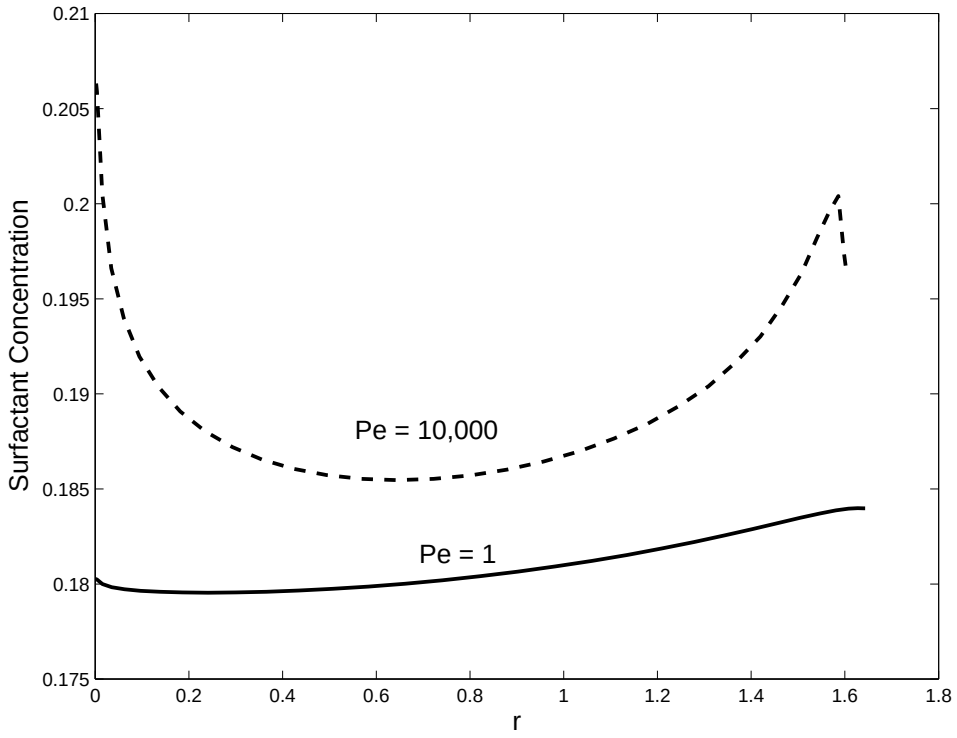

Figure 7.2: Surfactant profiles at $t = 10$ for large and small Peclet numbers. Surfactant strength is given by $\beta = 2$.

require a simple flat interface to produce a zero derivative. It is quite apparent that a boundary layer is forming near the contact line in the $Pe = 10,000$ case as there is an extremely rapid decrease in the surfactant concentration over a very short distance. The droplet profiles for these two cases are seen in Fig. 7.3. As was previously seen, the higher Peclet number retards droplet spreading. While the effect is small, it correlates with what was seen in the two-dimensional case.

Profiles of the droplet shape as it spreads are seen in Fig. 7.4. As was the case in two dimensions, the droplet spreads fastest at the beginning, when the $\theta - \theta_{Adv}$ quantity in (5.112) is greatest. As the droplet spreads and the contact angle decreases, the spread rate will decrease. Since we are dealing with wetting droplets, the spreading will never actually end, but it will continue to slow as the contact angle gets closer and closer to zero.

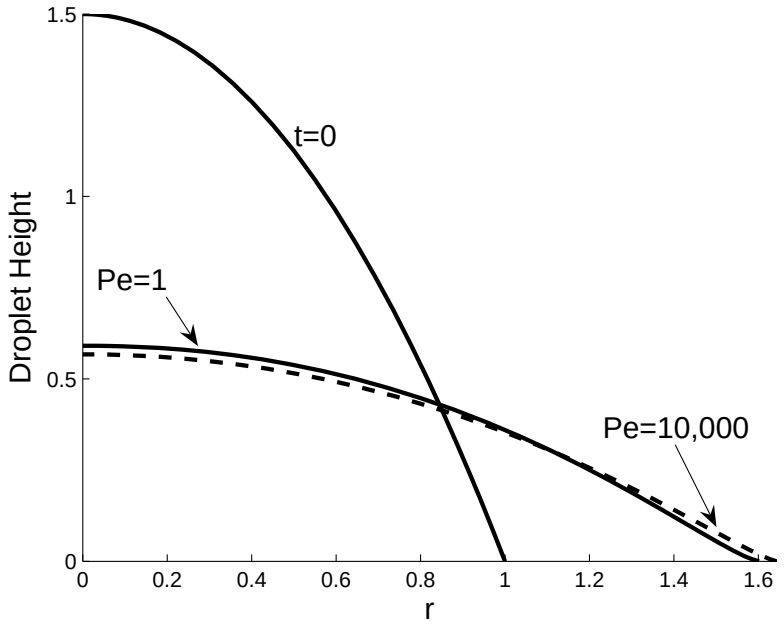

Figure 7.3: Droplet profiles at $t = 10$ for large and small Peclet numbers. Surfactant strength is given by $\beta = 2$.

The effects of flux are shown in Fig. 7.5. Here the no-flux condition on surfactant at the contact line has been removed and surfactant transport to and from the surface is governed by (5.52). Spreading rates for different concentrations of surfactant on the substrate (S_S) are plotted for various values of the transport parameter S_T. No-flux results ($S_T = 0$) are also included for comparison. The comparison graph from the two-dimensional results is Fig. 4.6. The same qualitative behavior exhibits itself in three dimensions as was seen in two dimensions. A strong flux of surfactant from the surface of the droplet speeds up the droplet while absorbing surfactant from the substrate further retards the droplet's spreading.

Surfactant profiles when flux is allowed are shown in Fig. 7.6. While the same qualitative behavior as seen in Fig. 4.7 is observed in three dimensions, the effects are more muted. There is still a downturn in surfactant concentration near the contact line when surfactant is leaving the droplet ($S_S = 0$) and an upturn when

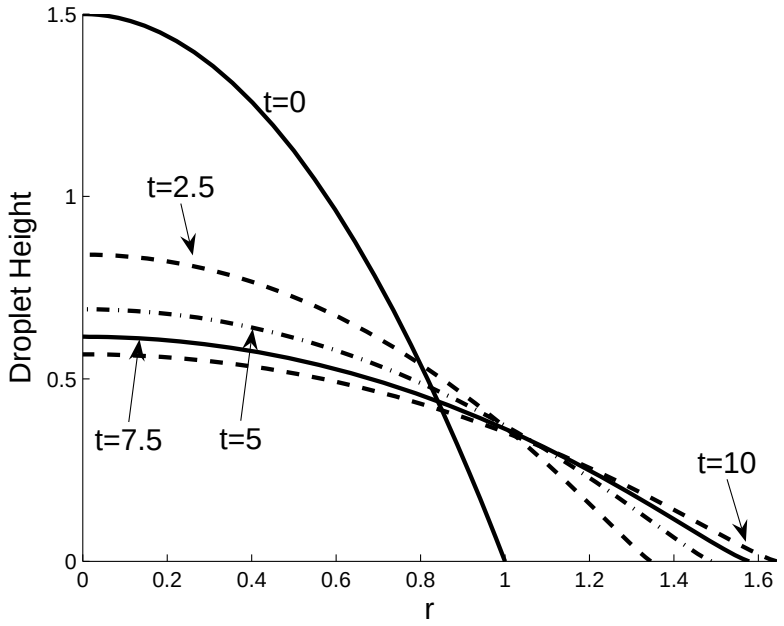

Figure 7.4: Three-dimensional axisymmetric droplet profiles for $\beta = 2, Pe = 1$.

surfactant is being absorbed ($S_S = 1/2$) but these effects are not as prominent as they were in two dimensions.

We have found that the three-dimensional axisymmetric results provide very good qualitative agreement with the two-dimensional results. This shows that the simplifications of the two-dimensional model do not change the droplet dynamics over the more physical three-dimensional model. While the effects of temperature could not be captured in three dimensions while maintaining symmetry, given the high correlation between the two- and three-dimensional models in the absence of temperature effects, it is quite likely that the temperature dependent observations of Chapter 4. The three-dimensional axisymmetric computations have thus been very useful to check the accuracy of the prior two-dimensional results and to ensure that they do, in fact, adequately capture the droplet's behavior.

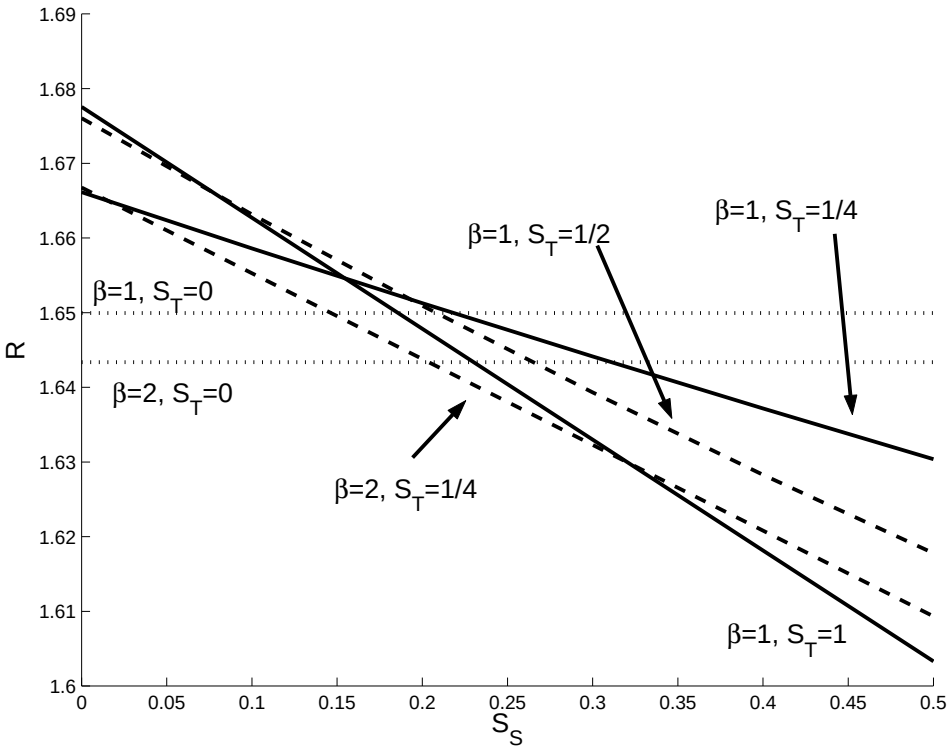

Figure 7.5: Effects of surfactant flux on spreading. Position of the right endpoint as a function of S_S at $t = 10$ for various β and S_T.

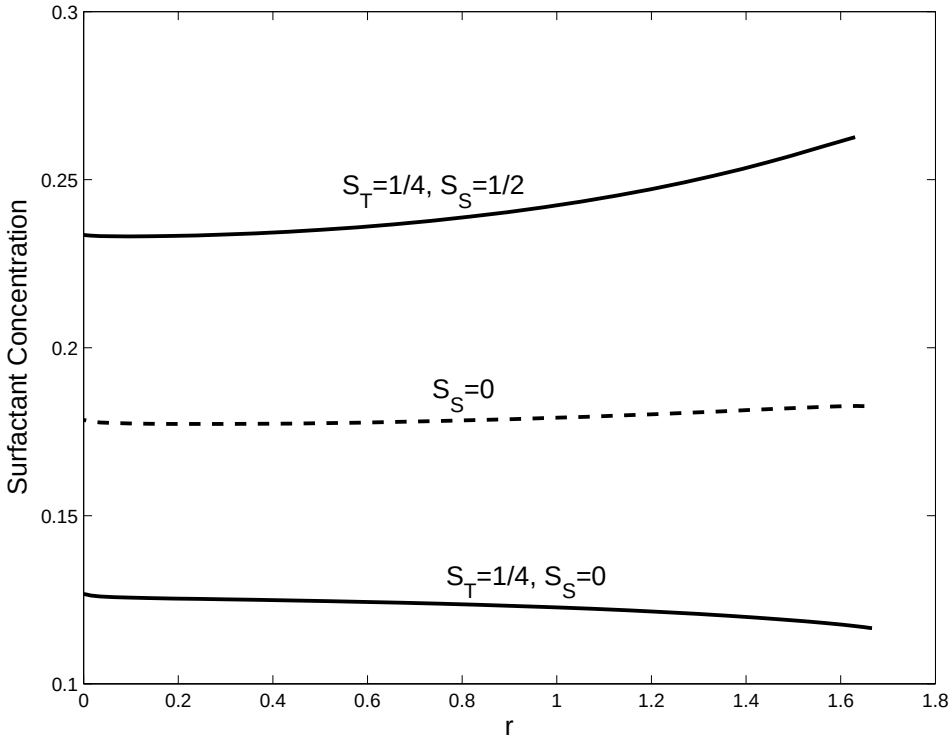

Figure 7.6: Effects of surfactant flux on spreading. Surfactant profiles at $t = 10$ with $\beta = 1$ and where flux of surfactant is allowed.

Chapter 8

Three-Dimensional Problem Formulation

We will now construct a fully three-dimensional formulation for the motion of a drop on a solid inclined plane. The motion of the drop is driven by the force of gravity. Surfactant and temperature effects are not included in the investigation here.

8.1 Formulation

We will be formulating our problem using cylindrical coordinates. Let r be the radial variable, ϕ be the angle from the origin, and z be the vertical variable, as measured from the substrate (see Fig. 8.1). The substrate itself is inclined by an angle α from the horizontal (see Fig. 8.2). The distance from the substrate the free surface is denoted $h(r,t)$ and $R(\phi,t)$ is the radius of the drop for a given angle ϕ. We define the contact angle θ as the angle the interface makes with the substrate in a plane perpendicular to the substrate and normal to the contact line. Gravity, g, acts in $-z\cos(\alpha)$. The velocity vector is given by $\vec{u} =< u, v, w >$.

We are interested in the following equations in the bulk of the fluid: conservation of mass,

$$\frac{1}{r}\frac{\partial}{\partial r}(ru) + \frac{1}{r}\frac{\partial v}{\partial \phi} + \frac{\partial w}{\partial z} = 0 \tag{8.1}$$

and conservation of momentum in the radial,

$$\begin{aligned}&\rho\left(\frac{\partial u}{\partial t} + u\frac{\partial u}{\partial r} + \frac{v}{r}\frac{\partial v}{\partial \phi} + w\frac{\partial u}{\partial z} - \frac{v^2}{r}\right)\\ &= -\frac{\partial P}{\partial r} + \mu\left(\frac{\partial^2 u}{\partial r^2} + \frac{1}{r}\frac{\partial u}{\partial r} - \frac{u}{r^2} + \frac{\partial^2 u}{\partial z^2} + \frac{1}{r^2}\frac{\partial^2 u}{\partial \phi^2} - \frac{2}{r^2}\frac{\partial v}{\partial \phi}\right) + \rho g\cos(\phi)\sin(\alpha),\end{aligned} \tag{8.2}$$

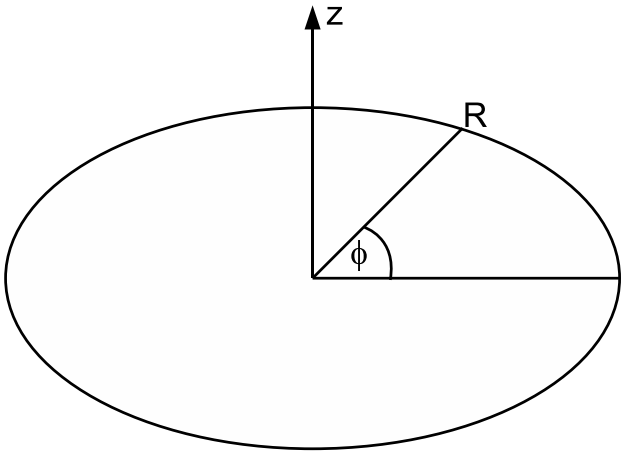

Figure 8.1: Illustrative figure of cylindrical coordinates

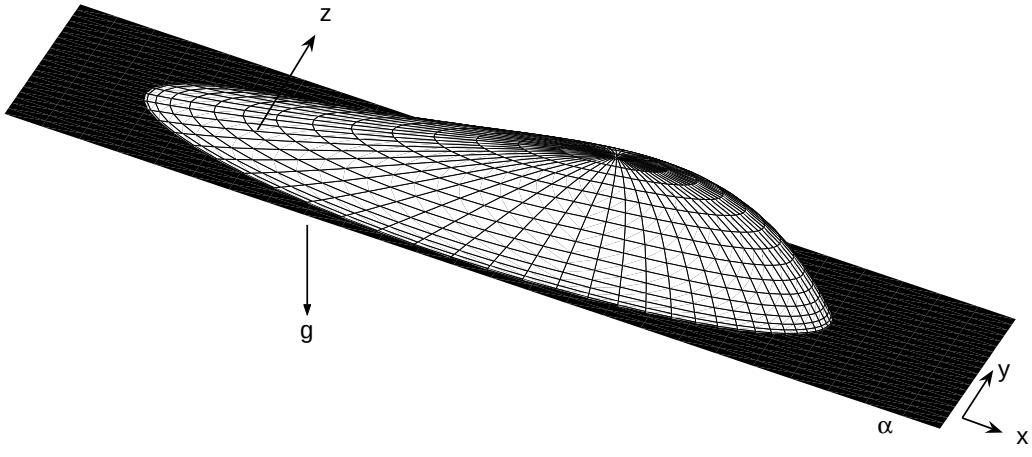

Figure 8.2: Three-dimensional droplet configuration

angular,

$$\rho\left(\frac{\partial v}{\partial t}+u\frac{\partial v}{\partial r}+\frac{uv}{r}+\frac{v}{r}\frac{\partial v}{\partial \phi}+w\frac{\partial v}{\partial z}\right)$$
$$=-\frac{1}{r}\frac{\partial P}{\partial \phi}+\mu\left(\frac{\partial^2 v}{\partial r^2}+\frac{1}{r}\frac{\partial v}{\partial r}-\frac{v}{r^2}+\frac{1}{r^2}\frac{\partial^2 v}{\partial \phi^2}+\frac{\partial^2 v}{\partial z^2}+\frac{2}{r^2}\frac{\partial u}{\partial \phi}\right)-\rho g\sin(\phi)\sin(\alpha), \tag{8.3}$$

and vertical directions

$$\rho\left(\frac{\partial w}{\partial t}+u\frac{\partial w}{\partial r}+\frac{v}{r}\frac{\partial w}{\partial \phi}+w\frac{\partial w}{\partial z}\right)$$
$$=-\frac{\partial P}{\partial z}+\mu\left(\frac{\partial^2 w}{\partial r^2}+\frac{1}{r}\frac{\partial w}{\partial r}+\frac{1}{r^2}\frac{\partial^2 w}{\partial \phi^2}+\frac{\partial^2 w}{\partial z^2}\right)-\rho g\cos(\alpha). \tag{8.4}$$

In these equations, ρ is the density of the fluid in the droplet, μ is the droplet's viscosity, and P is the pressure in the droplet. At $z=0$, no penetration of fluid through the interface implies:

$$w\Big|_{z=0}=0, \tag{8.5}$$

and, in order to relax the no-slip condition and relieve the singularity at the contact line (see e.g. Dussan V. and Davis[23]) we enforce the Navier slip condition

$$\vec{u}\cdot\hat{t}_s=\lambda(h)\mu\,\hat{n}_s\cdot\boldsymbol{S}\cdot\hat{t}_s, \tag{8.6}$$

where

$$\hat{n}_s=<0,0,1> \tag{8.7}$$

is the unit normal vector to the substrate and

$$\hat{t}_{s_1} = <1,0,0>, \tag{8.8a}$$
$$\hat{t}_{s_2} = <0,1,0> \tag{8.8b}$$

are the unit tangent vectors on the substrate. Since we have two unit tangent vectors, we will have two Navier slip conditions. We will be using

$$\lambda(h)=\frac{\lambda_1}{h} \tag{8.9}$$

for our slip function, which was first introduced by Greenspan[35].

At the free boundary, $z = h(r, \phi, t)$, we are interested in the kinematic condition

$$-\frac{\partial h}{\partial t} - u\frac{\partial h}{\partial r} - \frac{v}{r}\frac{\partial h}{\partial \phi} + w = 0 \tag{8.10}$$

and the jump in normal stress condition

$$\hat{n} \cdot \boldsymbol{\tau} \cdot \hat{n} = -\sigma\kappa, \tag{8.11}$$

where $\boldsymbol{\tau}$ is the stress tensor and κ is the mean curvature of the surface. The other condition at the free surface boundary is the continuity of tangential stress condition

$$\hat{n} \cdot \boldsymbol{\tau} \cdot \hat{t} = 0 \tag{8.12}$$

where $\hat{n}$ and $\hat{t}$ are the unit normal and tangent vectors to the free surface, which are defined as

$$\hat{n} = \frac{< -\frac{\partial h}{\partial r}, -\frac{1}{r}\frac{\partial h}{\partial \phi}, 1 >}{\sqrt{1 + \left(\frac{\partial h}{\partial r}\right)^2 + \frac{1}{r^2}\left(\frac{\partial h}{\partial \phi}\right)^2}}, \tag{8.13}$$

$$\hat{t}_1 = \frac{< 1, 0, \frac{\partial h}{\partial r} >}{\sqrt{1 + \left(\frac{\partial h}{\partial r}\right)^2}}, \tag{8.14}$$

$$\hat{t}_2 = \frac{< 0, 1, \frac{1}{r}\frac{\partial h}{\partial \phi} >}{\sqrt{1 + \frac{1}{r^2}\left(\frac{\partial h}{\partial \phi}\right)^2}}. \tag{8.15}$$

It should be noted that, as with the Navier slip condition, since we have two unit tangent vectors we have two continuity of tangential stress conditions.

We now need boundary conditions for the contact line. Let

$$\hat{n}_p = \frac{< R, -\frac{\partial R}{\partial \phi}, 0 >}{\sqrt{R^2 + \left(\frac{\partial R}{\partial \phi}\right)^2}}, \tag{8.16}$$

$$\hat{t}_p = \frac{< \frac{\partial R}{\partial \phi}, R, 0 >}{\sqrt{R^2 + \left(\frac{\partial R}{\partial \phi}\right)^2}} \tag{8.17}$$

be unit normal and tangent vectors in the plane of the substrate. Let

$$u_s = < u, v, w > \cdot \hat{n}_p \tag{8.18}$$

$$= \frac{R\,u - \frac{\partial R}{\partial \phi} v}{\sqrt{R^2 + \left(\frac{\partial R}{\partial \phi}\right)^2}} \tag{8.19}$$

be the slip velocity. We know that the position vector is given by

$$\vec{x} = R\,\hat{r}. \tag{8.20}$$

By taking a time derivative of the position vector and dotting it into the unit normal on the substrate, we will pick out the slip velocity:

$$\frac{\partial \vec{x}}{\partial t} = \frac{\partial R}{\partial t}\hat{r} \tag{8.21}$$

$$u_s = \frac{\partial \vec{x}}{\partial t} \cdot \hat{n}_p \tag{8.22}$$

$$= \frac{R\frac{\partial R}{\partial t}}{\sqrt{R^2 + \left(\frac{\partial R}{\partial \phi}\right)^2}}. \tag{8.23}$$

Combining (8.19) and (8.23) we find

$$R\frac{\partial R}{\partial t} = Ru - \frac{\partial R}{\partial \phi}v. \tag{8.24}$$

While this equation defines the motion of the contact line, it is not convenient to use. We will construct a relationship between the slip velocity and the contact angle and then use (8.23) to solve for the evolution of the contact line. To begin, we formally define the contact line velocity as being related to the contact angle by

$$u_s = f(\theta), \tag{8.25}$$

where

$$f(\theta) = \hat{k}\begin{cases} (\theta - \theta_{Adv})\,, & \theta > \theta_{Adv} \\ 0, & \theta_{Rec} \le \theta \le \theta_{Adv} \\ (\theta - \theta_{Rec})\,, & \theta < \theta_{Rec} \end{cases} \tag{8.26}$$

and $\hat{k}$ is a characteristic unit of velocity, is the $m = 1$ form of the slip velocity - contact angle relationship (1.2)–(1.3) extended to allow for hysteresis. It has been used by, among others, Greenspan[35] and Haley and Miksis[37]. When the droplet is travelling rapidly down a steeply inclined plane, it can be moving faster than the contact angle – slip velocity relationship (8.26) can move the rear contact line. In this situation, the fluid will flow away from the contact line, leaving a nonphysical

dry spot inside the calculated contact line. We will investigate two additional contact angle – slip velocity relationships to solve this problem. The first is given by

$$f_1(\theta) = \hat{k} \begin{cases} \tan(\theta - \theta_{Adv}), & \theta > \theta_{Adv} \\ 0, & \theta_{Rec} \leq \theta \leq \theta_{Adv} \\ \tan\left(\frac{\pi(\theta-\theta_{Rec})}{2\theta_{Rec}}\right) \frac{3\theta_{Rec}}{4\tan\left(\frac{3\pi}{8}\right)}, & \theta < \theta_{Rec} \end{cases} \tag{8.27}$$

and the second by

$$f_2(\theta) = \hat{k} \begin{cases} \operatorname{arctanh}(\theta - \theta_{Adv}), & \theta > \theta_{Adv} \\ 0, & \theta_{Rec} \leq \theta \leq \theta_{Adv} \\ \operatorname{arctanh}\left(\frac{\theta-\theta_{Rec}}{\theta_{Rec}}\right) \frac{3\theta_{Rec}}{4\operatorname{arctanh}\left(\frac{3}{4}\right)}, & \theta < \theta_{Rec} \end{cases} . \tag{8.28}$$

Both (8.27) and (8.28) have been equalized so that $f\left(\frac{\theta_{Rec}}{4}\right) = f_1\left(\frac{\theta_{Rec}}{4}\right) = f_2\left(\frac{\theta_{Rec}}{4}\right)$. They all behave similarly for $\theta > \theta_{Adv}$ due to the linearity of tan and arctanh near 0. For θ near 0, then both f_1 and f_2 will produce large velocities, causing the contact line to rapidly advance and preventing the fluid from leaving it behind.

We now combine (8.25) with (8.23) to get

$$\frac{\partial R}{\partial t} = \frac{1}{R}\sqrt{R^2 + \left(\frac{\partial R}{\partial \phi}\right)^2} f(\theta). \tag{8.29}$$

Now that we have determined the motion of contact line as a function of the contact angle, we must now determine the contact angle. Let

$$\hat{t}_{cs} = \hat{n} \times \hat{t}_p \tag{8.30}$$

$$= \frac{< -R,\ \frac{\partial R}{\partial \phi},\ -\frac{\partial h}{\partial r}R + \frac{1}{R}\frac{\partial h}{\partial \phi}\frac{\partial R}{\partial \phi} >}{\sqrt{\left(1 + \left(\frac{\partial h}{\partial r}\right)^2 + \frac{1}{R^2}\left(\frac{\partial h}{\partial \phi}\right)^2\right)\left(R^2 + \left(\frac{\partial R}{\partial \phi}\right)^2\right)}} \tag{8.31}$$

be the unit vector tangent to the surface at the contact line in the plane containing $\hat{n}$ and normal to the substrate. We can use the requirement that the droplet make contact with the substrate at the contact line,

$$h\left(R(\phi, t), \phi, t\right) = 0, \tag{8.32}$$

to conclude, by differentiating (8.32) with respect to ϕ, that

$$\frac{\partial h}{\partial \phi} = -\frac{\partial h}{\partial r}\frac{\partial R}{\partial \phi}. \tag{8.33}$$

This result allows us to simplify (8.31) to

$$\hat{t}_{cs} = \frac{< -R,\ \frac{\partial R}{\partial \phi},\ -\frac{\partial h}{\partial r}\left(R + \left(\frac{\partial R}{\partial \phi}\right)^2\right) >}{\sqrt{\left[1 + \left(\frac{\partial h}{\partial r}\right)^2\left(1 + \frac{1}{R^2}\left(\frac{\partial R}{\partial \phi}\right)^2\right)\right]\left[R^2 + \left(\frac{\partial R}{\partial \phi}\right)^2\right]}}. \tag{8.34}$$

Now we recognize that, since $\hat{n}_p$ and $\hat{t}_{cs}$ are both unit vectors, we can use the definition of the dot product to arrive at a formulation for the contact angle, θ:

$$\hat{n}_p \cdot \hat{t}_{cs} = |\hat{n}_p||\hat{t}_{cs}|\cos(\theta) \tag{8.35}$$

$$= \cos(\theta). \tag{8.36}$$

We can now use this result to determine $\tan(\theta)$, which is a slightly more natural form for the contact angle:

$$\tan(\theta) = \frac{\sqrt{1 - \cos^2(\theta)}}{\cos(\theta)} \tag{8.37}$$

$$= \frac{\sqrt{1 - \left(\hat{n}_p \cdot \hat{t}_{cs}\right)^2}}{\hat{n}_p \cdot \hat{t}_{cs}} \tag{8.38}$$

$$= -\frac{1}{R}\frac{\partial h}{\partial r}\sqrt{R^2 + \left(\frac{\partial R}{\partial \phi}\right)^2}. \tag{8.39}$$

Finally, the volume of the droplet is given by

$$V = \int_0^{2\pi}\int_0^{R(\phi,t)} h(r,\phi,t)\ r\ dr\ d\phi. \tag{8.40}$$

8.2 Evolution Equations and Nondimensionalization

We will nondimensionalize the problem in a different manner than we used for the two-dimensional and axisymmetric three-dimensional problems. We will still be using lubrication theory, whose basic assumption is that the height of the droplet is much less than its height. This relationship also implies that the contact angle is small. We thus use the dimensional contact angle θ to define our small parameter $\epsilon \ll 1$. The problem that we have with nondimensionalizing the problem is due to the inclination

of the plane. We can nondimensionalize the problem for small angles of inclination or for a nearly vertical plane. Unfortunately, these two nondimensionalizations are mutually exclusive. The scalings used in one become invalid if the angle of inclination moves away from the assumed range. We will construct a universally valid thin film equation, then nondimensionalize it.

We know from Section 5.3 which terms should be preserved in the lubrication approximation. We assume that the height is scaled one order smaller in ϵ than the radial and angular coordinates. Similarly, the vertical component of velocity will be one order smaller than the other two components of velocity. While we will not formally introduce ϵ into the problem, we will take advantage of our knowledge of what its introduction would do to scale the equations and use that knowledge to pick out the leading order terms of the equations. As before, we will use the h_0 notation to refer to the leading order component of the dependent variables.

Conservation of mass (8.1) remains unchanged as

$$\frac{1}{r}\frac{\partial}{\partial r}\left(ru_0\right) + \frac{1}{r}\frac{\partial v_0}{\partial \phi} + \frac{\partial w_0}{\partial z} = 0 \tag{8.41}$$

Conservation of momentum in the radial, angular, and vertical directions (8.2)–(8.4) become:

$$\frac{\partial p_0}{\partial r} = \mu\frac{\partial^2 u_0}{\partial z^2} + \rho g\cos(\phi)\sin(\alpha), \tag{8.42}$$

$$\frac{1}{r}\frac{\partial p_0}{\partial \phi} = \mu\frac{\partial^2 v_0}{\partial z^2} - \rho g\sin(\phi)\sin(\alpha), \tag{8.43}$$

$$\frac{\partial p_0}{\partial z} = \rho g\cos(\alpha). \tag{8.44}$$

The two slip conditions from (8.6) are

$$u_0 = \lambda(h_0)\frac{\partial u_0}{\partial z}, \tag{8.45}$$

$$v_0 = \lambda(h_0)\frac{\partial v_0}{\partial z}. \tag{8.46}$$

At the free boundary, the kinematic condition (8.10) is now

$$\frac{\partial h_0}{\partial t} = -u_0\frac{\partial h_0}{\partial r} - \frac{v_0}{r}\frac{\partial h_0}{\partial \phi} + w_0, \tag{8.47}$$

while the jump in normal stress condition (8.11) is

$$p_0 - p_A = -\sigma\left[\frac{1}{r}\frac{\partial}{\partial r}\left(r\frac{\partial h_0}{\partial r}\right) + \frac{1}{r^2}\frac{\partial^2 h_0}{\partial \phi^2}\right], \tag{8.48}$$

and the two terms of the continuity of tangential stress condition (8.12) become

$$\frac{\partial u_0}{\partial z} = 0, \tag{8.49}$$

$$\frac{\partial v_0}{\partial z} = 0. \tag{8.50}$$

We will now drop the subscripts to the variables. To find the general thin-film evolution equation, we will integrate (8.44) once with respect to z, finding:

$$p = -\rho g \cos(\alpha) z + q(r, \phi, t). \tag{8.51}$$

We will use this solution for the pressure in (8.48) to solve for q:

$$q = \rho g \cos(\alpha) h + p_A - \sigma \left[\frac{1}{r} \frac{\partial}{\partial r} \left(r \frac{\partial h}{\partial r} \right) + \frac{1}{r^2} \frac{\partial^2 h}{\partial \phi^2} \right]. \tag{8.52}$$

Substituting (8.51) in (8.42), we can solve for the radial component of velocity:

$$u = \frac{1}{\mu} \frac{\partial q}{\partial r} \frac{z^2}{2} - \frac{\rho g}{\mu} \cos(\phi) \sin(\alpha) \frac{z^2}{2} + A(r, \phi, t) z + C(r, \phi, t). \tag{8.53}$$

This speed, when evaluated in (8.49), allows us to determine that

$$A = -\frac{1}{\mu} \left(\frac{\partial q}{\partial r} - \rho g \cos(\phi) \sin(\alpha) \right) h, \tag{8.54}$$

and, when used in (8.45), shows that

$$C = \lambda(h) A. \tag{8.55}$$

When we substitute (8.51) in (8.43) we can solve for the angular velocity

$$v = \frac{1}{\mu} \left(\frac{1}{r} \frac{\partial q}{\partial \phi} + \rho g \sin(\phi) \sin(\alpha) \right) \frac{z^2}{2} + D(r, \phi, t) z + E(r, \phi, t). \tag{8.56}$$

We now expand the conservation of mass equation (8.41) to find the vertical velocity

$$w = -\frac{1}{r} \frac{\partial}{\partial r} \left[r \int u dz \right] - \frac{1}{r} \frac{\partial}{\partial \phi} \left(\int v dz \right) + F(r, \phi, t). \tag{8.57}$$

We will (8.57) unsimplified for the moment until we determine the remaining variables. The no-penetration condition (8.5) allows us to determine that

$$F = 0 \tag{8.58}$$

while by substituting (8.56) into (8.45) we can find that

$$D = -\frac{1}{\mu}\left(\frac{1}{r}\frac{\partial q}{\partial \phi} + \rho g \sin(\phi)\sin(\alpha)\right) h, \tag{8.59}$$

and with (8.46) we solve for

$$E = \lambda(h) D. \tag{8.60}$$

We can now formulate the full equation for the vertical velocity (8.57)

$$\begin{aligned} w = \frac{1}{\mu}\frac{1}{r}\frac{\partial}{\partial r}\left[r\left(-\frac{z^3}{6} + \frac{hz^2}{2} + \lambda(h)hz\right)\left(\frac{\partial q}{\partial r} - \rho g\cos(\phi)\sin(\alpha)\right)\right] \\ + \frac{1}{\mu}\frac{1}{r}\frac{\partial}{\partial \phi}\left[\left(-\frac{z^3}{6} + \frac{hz^2}{2} + \lambda(h)hz\right)\left(\frac{1}{r}\frac{\partial q}{\partial \phi} + \rho g\sin(\phi)\sin(\alpha)\right)\right]. \end{aligned} \tag{8.61}$$

Finally, using (8.53), (8.56) and (8.61) in the kinematic condition (8.47) at $z = h$ produces the general, dimensional thin-film equation

$$\begin{aligned} \mu\frac{\partial h}{\partial t} = \frac{1}{r}\frac{\partial}{\partial r}\left[r\left(\frac{h^3}{3} + \lambda(h)h^2\right)\left(\frac{\partial q}{\partial r} - \rho g\sin(\alpha)\cos(\phi)\right)\right] \\ + \frac{1}{r}\frac{\partial}{\partial \phi}\left[\left(\frac{h^3}{3} + \lambda(h)h^2\right)\left(\frac{1}{r}\frac{\partial q}{\partial \phi} + \rho g\sin(\alpha)\sin(\phi)\right)\right] \end{aligned} \tag{8.62}$$

where q is given by (8.52). These equations preserve the terms that capture the behavior of the droplet at both low and high angles of inclination and should remain valid for intermediate angles. In order to keep these terms, we choose the following nondimensionalization:

$$\begin{aligned} t &= \tilde{t}\frac{R_c}{\hat{k}}, & r &= \tilde{r}R_c, & z &= \tilde{z}R_c, \\ u &= \tilde{u}\hat{k}, & v &= \tilde{v}\hat{k}, & w &= \tilde{w}\hat{k}, \\ p &= \frac{\tilde{p}\mu\hat{k}}{R_c} + p_A, & R &= \tilde{R}R_c, & h &= \tilde{h}R_c, \\ V &= \tilde{V}R_c^3, & \sigma &= \sigma_c\tilde{\sigma}, & \lambda_1 &= \tilde{\lambda}_1 R_c^2 \end{aligned}$$

The variables with tildes over them are nondimensional. We introduce the nondimensional parameters, the Bond, capillary, and Reynolds numbers:

$$B = \frac{\rho g R_c^2}{\sigma_c}, \qquad Ca = \frac{\mu\hat{k}}{\sigma_c}, \qquad Re = \frac{\rho R_c \hat{k}}{\mu}.$$

This nondimensionalization does not include the thin film assumption. We thus have to make certain that the droplets that we use in our computations are thin, with their height being much less than their width and a small contact angle. As long as this is the case then we are within the lubrication limit and the governing equations remain a reasonable composite approximation for the evolution of a thin drop sliding down an inclined plane.

We also initialize the droplet to a constant dimensional volume, which allows us to pick our characteristic length scale R_c. Substituting a simple initial droplet profile of

$$h = \frac{\theta_I \left(R_I^2 - r^2\right)}{2R_I}, \tag{8.63}$$

where θ_I is the initial contact angle and R_I the initial radius, into the volume integral (8.40) yields

$$V = \frac{\pi R_c^3 \theta_I R_I^3}{4}. \tag{8.64}$$

Requiring a constant volume imposes a condition that $\theta_I R_I^3$ must be equal to a constant. To impose the lubrication approximation requirement that the droplet's height be much smaller than its width, we require that

$$\theta_I R_I^3 = \frac{1}{3}, \tag{8.65}$$

which gives us with the length scale

$$R_c^3 = \frac{12}{\pi} V. \tag{8.66}$$

We will return to this relationship when we discuss the initial shape of the droplet.

Applying these scalings to (8.62)–(8.52), we arrive at our nondimensional evolution equation

$$\begin{aligned}\frac{\partial \tilde{h}}{\partial \tilde{t}} = &\frac{1}{Ca}\frac{1}{\tilde{r}}\frac{\partial}{\partial \tilde{r}}\left[\tilde{r}\left(\frac{\tilde{h}^3}{3} + \tilde{\lambda}(\tilde{h})\tilde{h}^2\right)\left(\frac{\partial q}{\partial \tilde{r}} - B\sin(\alpha)\cos(\phi)\right)\right] \\ &+ \frac{1}{Ca}\frac{1}{\tilde{r}}\frac{\partial}{\partial \phi}\left[\left(\frac{\tilde{h}^3}{3} + \tilde{\lambda}(\tilde{h})\tilde{h}^2\right)\left(\frac{1}{\tilde{r}}\frac{\partial q}{\partial \phi} + B\sin(\alpha)\sin(\phi)\right)\right]\end{aligned} \tag{8.67}$$

where

$$\tilde{q} = B\cos(\alpha)\tilde{h} - \frac{1}{\tilde{r}}\left[\frac{\partial}{\partial \tilde{r}}\left(r\frac{\partial \tilde{h}}{\partial \tilde{r}}\right) + \frac{1}{\tilde{r}}\frac{\partial^2 \tilde{h}}{\partial \phi^2}\right] = \frac{R_c}{\sigma_c}\left(q - p_A\right). \tag{8.68}$$

The contact boundary condition becomes

$$\tilde{h}\left(\tilde{R}(\phi,\tilde{t}),\phi,\tilde{t}\right)=0 \tag{8.69}$$

The nondimensionalization of (8.29) give us

$$\frac{\partial\tilde{R}}{\partial\tilde{t}}=\frac{1}{\tilde{R}}\sqrt{\tilde{R}^2+\left(\frac{\partial\tilde{R}}{\partial\phi}\right)^2}\,\tilde{f}(\theta) \tag{8.70}$$

while (8.39) gives us

$$\theta=\tan^{-1}\left(-\frac{1}{\tilde{R}}\frac{\partial\tilde{h}}{\partial\tilde{r}}\sqrt{\tilde{R}^2+\left(\frac{\partial\tilde{R}}{\partial\phi}\right)^2}\right), \tag{8.71}$$

where

$$\tilde{f}(\theta)=\begin{cases}(\theta-\theta_{Adv}), & \theta>\theta_{Adv}\\ 0, & \theta_{Rec}\le\theta\le\theta_{Adv}\\ (\theta-\theta_{Rec}), & \theta<\theta_{Rec}\end{cases}=\frac{1}{\hat{k}}f(\theta). \tag{8.72}$$

Similarly,

$$\tilde{f}_1(\theta)=\begin{cases}\tan(\theta-\theta_{Adv}), & \theta>\theta_{Adv}\\ 0, & \theta_{Rec}\le\theta\le\theta_{Adv}\\ \tan\left(\frac{\pi(\theta-\theta_{Rec})}{2\theta_{Rec}}\right)\frac{3\theta_{Rec}}{4\tan\left(\frac{3\pi}{8}\right)}, & \theta<\theta_{Rec}\end{cases}=\frac{1}{\hat{k}}f_1(\theta) \tag{8.73}$$

and

$$\tilde{f}_2(\theta)=\begin{cases}\operatorname{arctanh}(\theta-\theta_{Adv}), & \theta>\theta_{Adv}\\ 0, & \theta_{Rec}\le\theta\le\theta_{Adv}\\ \operatorname{arctanh}\left(\frac{\theta-\theta_{Rec}}{\theta_{Rec}}\right)\frac{3\theta_{Rec}}{4\operatorname{arctanh}\left(\frac{3}{4}\right)}, & \theta<\theta_{Rec}\end{cases}=\frac{1}{\hat{k}}f_2(\theta). \tag{8.74}$$

Finally, the volume of the droplet is now given by

$$\tilde{V}=\int_0^{2\pi}\int_0^{\tilde{R}(\phi,\tilde{t})}\tilde{h}(\tilde{r},\phi,\tilde{t})\;\tilde{r}\;d\tilde{r}\;d\phi. \tag{8.75}$$

We will now drop the tildes from the nondimensional variables.

It should be noted that this parameterization assumes that h is a function of r and ϕ with $0\le r\le R(\phi,t)$, and that R is a function of ϕ. This may not be the

case in all situations, e.g. where there is a rupture or a pearling instability. We will allow the origin of our cylindrical coordinate system to vary to compensate for more complicate interface shapes, but this parameterization is a limitation of the current numerical approach.

Chapter 9

Three-Dimensional Numerical Method

9.1 Outline of Numerical Method

The droplet evolution equation, (8.67), subject to boundary conditions (8.69), and the radius evolution equation (5.111) are solved using a numerical method employing semi-implicit time stepping and Chebyshev pseudo-spectral spatial derivatives. The Chebyshev scheme has the advantage that it bunches points near the contact lines, where the dynamics are the most sensitive. The resulting nonlinear system is then solved by Newton's method. Although the method is only first order in time, it is extremely robust.

9.2 Conversion into Chebyshev Space

In order to use Chebyshev derivatives, we must convert our problem from real space into Chebyshev space. We start with a rescaling of the parameters. We need to map the domain of the problem from $r \in [0, R]$ onto $\xi \in [-1, 1]$. In order to avoid the numerical singularity at $r = 0$, we will compute not on $r \in [0, R(\phi)]$ but on $r \in [-R(\phi - \pi), R(\phi)]$ and use an even number of collocation points, thus skipping over $r = 0$. This change of variables means that we do not need to evaluate the equation on the entire $\phi \in [0, 2\pi)$ domain; we can restrict ourselves to computing in $\phi \in [-\pi/2, \pi/2)$. For more information on this approach, please see Trefethen [81].

Let us now formally introduce our new variables. Let

$$r = \frac{R_R(t) - R_L(t)}{2}\xi^2 + \frac{R_R(t) + R_L(t)}{2}\xi \tag{9.1}$$

be the new scaling for the radial coordinate, where $\xi \in [-1,1]$, $R_R = R(\phi)$ and $R_L = R(\phi - \pi)$. Both R_R and R_L are positive. One advantage of this scaling is that r and ξ share the same sign, which prevents the numerical instabilities that would result if $\xi > 0$ and $r < 0$.

Since r is now a function of $R(\phi, t)$, we need to redefine derivatives with respect to t as

$$\frac{\partial}{\partial t} = \frac{\partial}{\partial \tau} - \frac{\frac{\partial}{\partial \tau}\left[\left(R_R - R_L\right)\xi^2 + \left(R_R + R_L\right)\xi\right]}{2\xi\left(R_R - R_L\right) + R_R + R_L}\frac{\partial}{\partial \xi}, \tag{9.2}$$

where $\tau = t$. The change of variables also results in the spatial derivatives becoming

$$\frac{\partial}{\partial r} = \frac{2}{2\xi\left(R_R - R_L\right) + R_R + R_L}\frac{\partial}{\partial \xi}, \tag{9.3}$$

$$\frac{\partial}{\partial \phi} = \frac{\partial}{\partial \beta} - \frac{\frac{\partial}{\partial \beta}\left[\left(R_R - R_L\right)\xi^2 + \left(R_R + R_L\right)\xi\right]}{2\xi\left(R_R - R_L\right) + R_R + R_L}\frac{\partial}{\partial \xi}, \tag{9.4}$$

where $\beta = \phi$.

Details of the Chebyshev pseudo-spectral method that is used to take the derivatives in the radial direction are given in Appendix B. One result of the distribution of Chebyshev collocation points is that it bunches points near the ends of the domain. This is fortuitous since it results in extra points near the contact line, where the dynamics occur on the shortest spatial scales.

Spatial derivatives in the angular direction are performed using a Fourier pseudo-spectral method. Details of this method are presented in Appendix B. The Fourier pseudo-spectral method requires periodic data, which does not exist in this formulation of the problem as $\beta \in [-\pi/2, \pi/2)$. This problem is easy to rectify, however, if we construct a temporary data array that reconstructs the height data on a $\beta \in [-\pi, \pi)$ domain and then maps the computed derivatives back. While the mapping and re-mapping process requires a modicum of computational effort, this cost is inconsequential in comparison to the increased grid size that would be needed to preserve accuracy if finite differences were used instead to take the derivatives.

9.3 Time Derivatives

We will use a semi-implicit timestepping scheme. Given that every spatial derivative involves multiple time dependent quantities, we have a large number of

potential schemes from which to choose. We have chosen a method that is robust and produces accurate results for the problems we have chosen to study. In conservative form, our numerical method is:

$$\frac{h^{n+1}-h^n}{\Delta t}-\frac{\left(R_R^n-R_R^{n-1}-R_L^n+R_L^{n-1}\right)\xi^2+\xi\left(R_R^n-R_R^{n-1}+R_L^n-R_L^{n-1}\right)}{\Delta t\left[2\xi\left(R_R^n-R_L^n\right)+R_R^n+R_L^n\right]}\frac{\partial h^n}{\partial\xi}=$$
$$\frac{1}{r^n}\frac{\partial}{\partial r^n}\left[r^n\left(\frac{\left(h^n\right)^3}{3}+\lambda^n\left(h^n\right)^2\right)\left(\frac{\partial q}{\partial r^{n+1}}-B\sin(\alpha)\cos(\beta)\right)\right]$$
$$+\frac{1}{r^n}\frac{\partial}{\partial\beta^n}\left[\left(\frac{\left(h^n\right)^3}{3}+\lambda^n\left(h^n\right)^2\right)\left(\frac{1}{r^n}\frac{\partial q}{\partial\beta^{n+1}}+B\sin(\alpha)\sin(\beta)\right)\right] \quad (9.5)$$

where

$$q = B\cos(\alpha)h^n-\frac{1}{r^n}\left[\frac{\partial}{\partial r^{n+1}}\left(r^n\frac{\partial h^{n+1}}{\partial r^{n+1}}\right)+\frac{1}{r^n}\frac{\partial^2 h^{n+1}}{\partial\left(\beta^{n+1}\right)^2}\right], \quad (9.6)$$

$$\frac{\partial}{\partial r^n} = \frac{2}{2\xi\left(R_R^n-R_L^n\right)+R_R^n+R_L^n}\frac{\partial}{\partial\xi}, \quad (9.7)$$

$$\frac{\partial}{\partial\beta^n} = \frac{\partial}{\partial\beta}-\frac{\frac{\partial}{\partial\beta}\left[\left(R_R^n-R_L^n\right)\xi^2+\left(R_R^n+R_L^n\right)\xi\right]}{2\xi\left(R_R^n-R_L^n\right)+R_R^n+R_L^n}\frac{\partial}{\partial\xi} \quad (9.8)$$

and the contact line is advanced by

$$\frac{R^{n+1}-R^n}{\Delta t}=\frac{1}{R^{n+1}}\sqrt{\left(R^{n+1}\right)^2+\left(\frac{\partial R^{n+1}}{\partial\phi}\right)^2}$$
$$\times\ f\left(\tan^{-1}\left[-\frac{1}{R^{n+1}}\frac{\partial h^{n+1}}{\partial r^{n+1}}\sqrt{\left(R^{n+1}\right)^2+\left(\frac{\partial R^{n+1}}{\partial\phi}\right)^2}\right]\right). \quad (9.9)$$

The method is computed in conservative form (e.g. the function q is constructed and derivatives are taken of it, rather than distributing the derivatives through to its constituent terms). At each timestep, each derivative in (9.5) and (9.9) is reconstructed from the Chebyshev coordinates into (r,ϕ) space via (9.3) and (9.4). Once assembled, the terms are used to advance h to the next timestep. The derivatives are always taken in Chebyshev space; the transition to (r,ϕ) space is done solely to calculate the evolution equation. Conservative form derivatives are used because it was found that they reduce numerical instabilities. The code was more stable when the derivatives were taken of the combined terms rather than taking fourth derivatives of h and assembling those. The one exception to this is that the $\frac{\partial^2 h^{n+1}}{\partial\left(\beta^{n+1}\right)^2}$ term in (9.6)

is calculated by analytically applying (9.4) to itself and then evaluating the resulting derivatives numerically. This is the only time that terms are expanded further than presented in (9.5). This one term is more accurate when expanded out analytically; other terms are not expanded out since the derivative of their sums (conservative form) is more accurate than the sum of their derivatives (expanded form).

To march forward from timestep t^n to $t^{n+1} = t^n + \Delta t$ we construct a series of nonlinear equations for $h_{i,j}^{n+1} = h(\xi_i, \beta_j, t^{n+1}, t^n)$, $R_j^{n+1} = R(t^{n+1}, \phi_j, t^n)$, where ξ_i represents the value of ξ at the i^{th} Chebyshev collocation point, $\beta_j = j\Delta\beta - \pi/2$ and $\phi_j = j\Delta\phi$. The index for j starts at 0 so $\beta_0 = -\pi/2$ and $\phi_0 = 0$. We then solve the resulting system via Newton's method. The resulting matrix is full. Using finite differences rather than a Chebyshev pseudo-spectral method to compute spatial derivatives would result in a sparse matrix, which would result in significant time savings when solving the nonlinear system. Unfortunately, in order to maintain a given level of accuracy, we would have to drastically increase the number of spatial gridpoints, which would result in a much larger matrix to invert, more than negating any time savings bought by using finite differences.

9.4 Regridding

As the droplet translates down the inclined plane it quickly spreads past the initial origin. This presents obvious difficulties since the cylindrical coordinates of our numerical scheme require the origin to be within the droplet so that $R(\phi)$ is single valued.

The solution to this difficulty is to regrid the data onto a new origin as the droplet translates. To capture the details of the behavior near the leading edge of the droplet as it spreads down the inclined plane, we keep the origin closer to the leading edge than to the trailing edge. Figure 9.1 shows the location of the origin before and after regridding. Regridding occurs whenever the distance between the old origin, O_{old}, and the trailing edge, $R_L(0)$, is 1.5 times the distance between the old origin and the leading edge, $R_R(0)$. In terms of Fig. 9.1, regridding occurs when d_L equals 1.5 d_R. We then move the origin to O_{new}, so that the trailing edge is twice as far away from the origin as the leading edge. In terms of the figure, we set $d_{L_{new}} = 2d_{R_{new}}$.

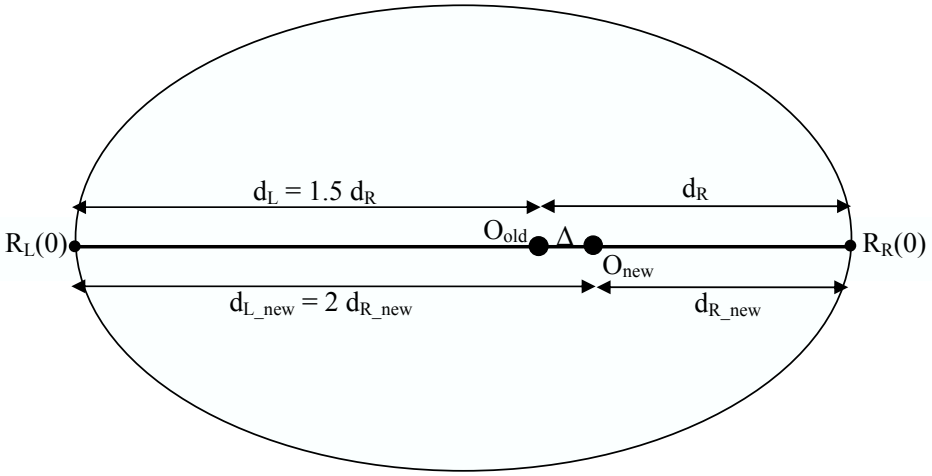

Figure 9.1: Movement of the origin during regridding.

The origin is moved a distance Δ.

The difficulty now is to map the droplet height function h and the droplet radius R from their old points onto the new ones, while preserving spectral accuracy. To map the contact line R onto the new origin, we must determine the distance between the old radii and the new origin. This is more difficult than it first appears, since by moving the origin an arbitrary distance, we do not know the angle from the new origin to the old radius. Figure 9.2 demonstrates this problem. (Note that Fig. 9.2 is not to scale.) In Fig 9.2, the locations of O_o and O_n are known, as is Δ, the distance between O_o and O_n. The length of the old radius, R_o is known, as is the angle ϕ_o between the droplet's centerline and old radius. The length of the new radius R_n is not known.

Note that the gridpoints on the contact line points are equally spaced in ϕ with respect to the old origin, but they are not equally spaced with respect to the new origin, as illustrated in Fig. 9.3 for four gridpoints. Here the four gridpoints are spaced at 90 degree intervals around O_o, but they are not equally spaced in ϕ around the new origin O_n.

We want to know the distance from the new origin to the contact line. The

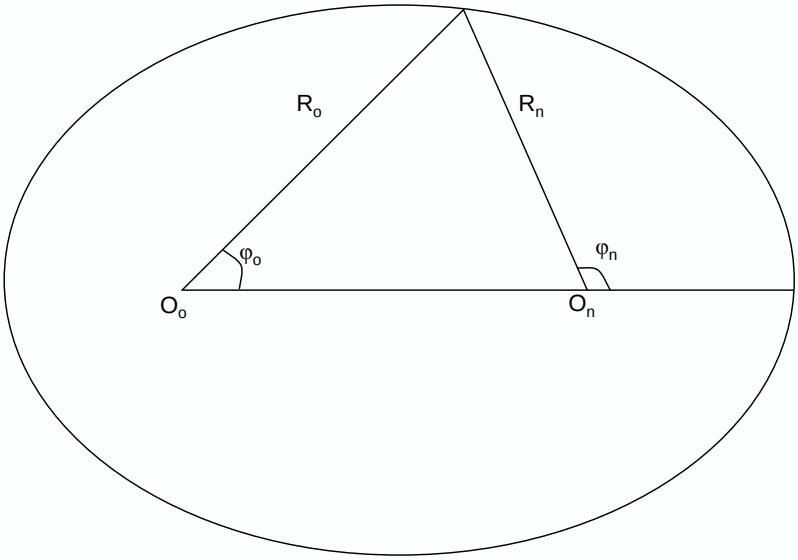

Figure 9.2: Illustrative figure of angles from new and old origins and distances to the contact line. Not to scale.

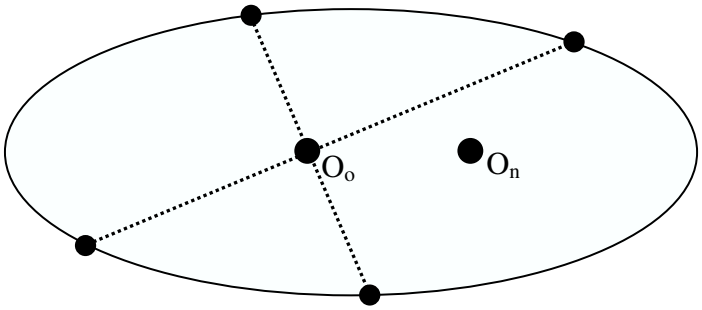

Figure 9.3: Illustrative figure of gridpoints spaced equally around the old origin and unequally around the new origin. Not to scale.

Law of Cosines defines the R_n for each point on the contact line:

$$R_n^2 = R_o^2 + \Delta^2 - 2R_o\Delta\cos(\phi_o). \tag{9.10}$$

These values of R_n are equally spaced in ϕ_o about O_o. The Law of Sines allows us to determine the values of ϕ_n that correspond to each R_n:

$$\frac{\sin(\phi_o)}{R_n} = \frac{\sin(\phi_n)}{R_o}. \tag{9.11}$$

We next need to find the values of the radius that lie on equally spaced ϕ around O_n. Refer to these equally spaced around O_n radii as R_n and the equally spaced angles as ϕ_n. (For the full details on the cubic spline, see Shampine *et al.*[71].) This interpolation function allows us to estimate the distance between the new origin and the contact line for any angle. In particular, we can estimate the values of R_e at the angles ϕ_e which are equally spaced about O_n.

These values of R_e are only an initial approximation. We use a Newton solver based on geometric constraints to find more accurate values for R_e. The spline step is important to determine a good initial guess for the Newton solver; if the spline is eliminated then the Newton solver has difficulties converging to the correct contact line. We will discuss the details of the Newton solver shortly.

Let us now reconsider the definitions of ϕ_o and R_o. For each ϕ_e in our domain, let (ϕ_e, R_e) be the angle and radius from the new origin to the point on the contact line corresponding to this equally spaced angle. Let (ϕ_o, R_o) be the angle and radius from the old origin to this same point. Swapping ϕ_n for ϕ_e, the picture of these points is the same as shown in Fig. 9.2, except that the point marked on the contact line is now on an equally spaced ϕ_e rather than an equally spaced ϕ_o. At this stage we only know ϕ_e; ϕ_o, R_o, and R_e are all unknown.

The Law of Sines can be rearranged and considered as a nonlinear equation for the angle ϕ_o:

$$\phi_o = \arcsin\left(\frac{R_e}{R_o}\sin(\phi_e)\right) \tag{9.12}$$

If we knew ϕ_o, we could use a Fourier series approximation to determine R_o:

$$R_o = \sum_{k=-N}^{N} \tilde{a}_k e^{ik\phi_o} \tag{9.13}$$

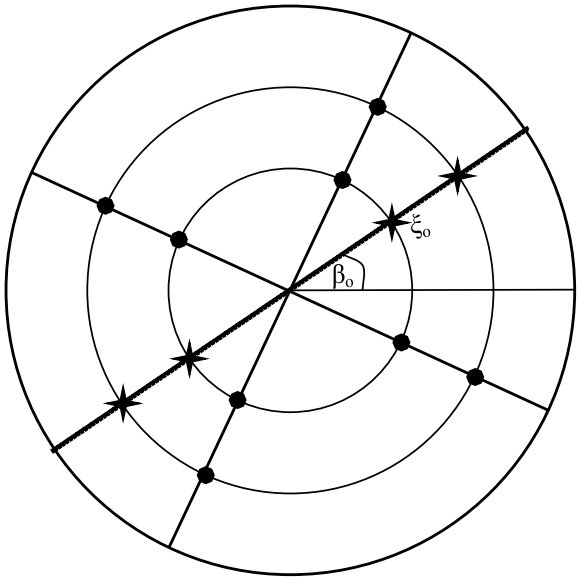

Figure 9.4: Illustrative figure of the Chebyshev coordinates associated with regridding.

where the $\tilde{a}_k$ terms are given by (B.16). Details on Fourier series are presented in Appendix B, specifically (B.15) and (B.16). Such a Fourier approximation is spectrally accurate, as we are already using Fourier derivatives in the angular direction. We could then use the Law of Cosines, (9.10), to calculate the actual item of interest: R_e.

$$R_e = \sqrt{R_o^2 + \Delta^2 - 2R_o\Delta\cos(\phi_o)} \tag{9.14}$$

The equations (9.12), (9.13), and (9.14) must be solved for the three unknowns ϕ_o, R_o, and R_n. We solve these equations simultaneously with a Newton solver, using the data from the spline as the initial guess.

After the Newton solver converges, we know the new location of the points along the new contact line and can extrapolate to find the (r_n, ϕ_n) locations of all the points inside the droplet by using (9.1). Using these points, it is trivial to locate the (r_o, ϕ_o) locations that correspond to each (r_n, ϕ_n) inside the droplet by translating the coordinates into x-y space, attaining the (x,y) coordinates of each (r_n, ϕ_n) and then calculating the (r_o, ϕ_o) of this (x,y) coordinate. Knowing the (r_o, ϕ_o) locations in the old space allows us to compute the (ξ_o, β_o) location of these points.

We now need to find the droplet height associated with each (ξ_o, β_o). It is helpful to now think of our (ξ, β) domain as a series of concentric circles and spokes,

as seen in Fig. 9.4. We compute Chebyshev coefficients of the height on every spoke. Then we compute the Fourier coefficients of the Chebyshev coefficients along each circle. For a given (ξ_o, β_o), we construct an imaginary "spoke" going through our domain on the angle ϕ_o, represented by the line with the stars in Fig. 9.4. To calculate the height at ξ_o along this spoke, we need to determine the Chebyshev coefficients along it. Thus for each "circle," we interpolate the Chebyshev coefficients for the angle β_o by using our previously calculated Fourier coefficients. Finally, we interpolate our new Chebyshev coefficients at the point ξ_o to determine the height at (ξ_o, β_o). This procedure is then repeated for every (ξ_o, β_o) to interpolate the old height function onto the new domain. Each interpolation should retain spectral accuracy since the underlying data was advanced using Fourier and Chebyshev derivatives.

9.5 Convergence Checks

More convergence checks are provided for the full three-dimensional numerical scheme than for the prior schemes since there are now two sets of variables that need to be analyzed: angular and radial coordinates. The first set of convergence checks is done on a steadily translating droplet. In these calculations, $\alpha = 90°, Ca = 0.1, B = 2.5, \theta_{Adv} = 30°, \theta_{Rec} = 20°$. We use the base contact angle – slip velocity relationship (8.72) and the results are shown at $t = 1000$. Table 9.1 shows the results when the number of angular gridpoints (in the ϕ direction) are kept at a constant 32 points and the number of radial gridpoints (in the r direction) are varied. Contrary to the previous convergence checks, each row here represents a true doubling in the number of collocation points. An even number of collocation points is used in order to avoid laying down a point on the origin, thus allowing for a proper doubling at each grid refinement. The columns of the table represent the difference in the volume of the droplet and the difference in the location of the forward edge of the droplet. Table 9.2 represents a similar convergence check but for successive doubling of the number of angular collocation points while keeping a fixed 32 radial collocation points. Finally, Table 9.3 gives the results of the convergence check in time. The timesteps represented here are multiples of the base timestep of 10^{-4}, where a constant 32 angular and radial collocation points are used.

Radial Gridpoints	V Difference	R Difference
$8 \rightarrow 16$	$2.70 \cdot 10^{-1}$	$1.75 \cdot 10^{-1}$
$16 \rightarrow 32$	$4.21 \cdot 10^{-3}$	$2.37 \cdot 10^{-3}$
$32 \rightarrow 64$	$1.64 \cdot 10^{-4}$	$1.57 \cdot 10^{-4}$

Table 9.1: Three-dimensional radial convergence for translating droplet. Using 32 angular gridpoints.

Angular Gridpoints	V Difference	R Difference
$8 \rightarrow 16$	1.13	$8.92 \cdot 10^{-2}$
$16 \rightarrow 32$	$1.15 \cdot 10^{-3}$	$1.28 \cdot 10^{-3}$
$32 \rightarrow 64$	$2.26 \cdot 10^{-4}$	$4.96 \cdot 10^{-6}$

Table 9.2: Three-dimensional angular convergence for translating droplet. Using 32 radial gridpoints.

From Tables 9.1–9.5 we can tell that the method is spectrally accurate in space. One important conclusion is that 8 points in either the radial or angular direction appears to be inadequate. While we expect, and see, that the difference in the computed metrics decreases with each successive doubling on the number of collocation points, the difference in going from 8 to 16 points is especially large in the fully three-dimensional method. For example, we see an order one change in the computed volume when going from 8 to 16 angular gridpoints. In particular, the method doubled in mass for 8 angular gridpoints. For 16 gridpoints, it has well under 1% mass gain. With 16 and more points, the mass change quickly converges toward zero as both radial and angular gridpoints are doubled.

Table 9.3 shows that the method converges as first order in time. Each halving of the timestep, shown on successive rows, results in a halving of the computed volume or location of the leading edge of the droplet. While the change in volume when timestep is changed from 8 times the base value to four times the base value is actually smaller than the change when the timestep is halved again, the difference in the location of the leading edge is reduced by approximately half. The differences in the volume after this are roughly halved with each halving of the timestep. As

Timestep	V Difference	R Difference
$32 \rightarrow 16$	$6.07 \cdot 10^{-3}$	$4.66 \cdot 10^{-2}$
$16 \rightarrow 8$	$3.81 \cdot 10^{-3}$	$2.56 \cdot 10^{-2}$
$8 \rightarrow 4$	$5.10 \cdot 10^{-4}$	$1.32 \cdot 10^{-2}$
$4 \rightarrow 2$	$2.77 \cdot 10^{-3}$	$5.99 \cdot 10^{-3}$
$2 \rightarrow 1$	$1.01 \cdot 10^{-3}$	$3.11 \cdot 10^{-3}$
$1 \rightarrow 1/2$	$6.37 \cdot 10^{-4}$	$1.14 \cdot 10^{-3}$
$1/2 \rightarrow 1/4$	$3.17 \cdot 10^{-4}$	$8.26 \cdot 10^{-4}$
$1/4 \rightarrow 1/8$	$1.65 \cdot 10^{-4}$	$4.44 \cdot 10^{-4}$

Table 9.3: Three-dimensional temporal convergence for translating droplet. Using 32 radial and angular gridpoints.

Radial Gridpoints	V Difference	R Difference
$8 \rightarrow 16$	$9.97 \cdot 10^{-3}$	$1.75 \cdot 10^{-1}$
$16 \rightarrow 32$	$1.90 \cdot 10^{-5}$	$2.37 \cdot 10^{-3}$
$32 \rightarrow 64$	$8.68 \cdot 10^{-7}$	$1.57 \cdot 10^{-4}$

Table 9.4: Three-dimensional radial convergence for deforming droplet. Using 32 angular gridpoints.

with the two-dimensional results, we do not find this aberrant result disturbing since convergence immediately reverts to first order in time and it only occurs for the volume calculation; the convergence of the location of the leading edge is always first order, without exception.

We then compute the convergence of a deforming droplet. Here we take $\alpha = 26°, Ca = 0.1, B = 1.9, \theta_{Adv} = 30°, \theta_{Rec} = 15°$ and the data is taken at $t = 100$ and we again use (8.72) for the contact angle – slip velocity relationship. The radial convergence checks are presented in Table 9.4, where the number of radial collocation points are doubled while the number of angular points is kept constant at 32. Next, the radial points are held at 32 while the number of angular points are successively doubled. The results of this check are shown in Table 9.5. These spatial convergence checks show that the volume and the difference in the location of

Angular Gridpoints	V Difference	R Difference
$8 \rightarrow 16$	$5.40 \cdot 10^{-2}$	$1.49 \cdot 10^{-2}$
$16 \rightarrow 32$	$8.62 \cdot 10^{-4}$	$4.37 \cdot 10^{-4}$
$32 \rightarrow 64$	$1.14 \cdot 10^{-5}$	$3.83 \cdot 10^{-6}$

Table 9.5: Three-dimensional angular convergence for deforming droplet. Using 32 radial gridpoints.

Timestep	V Difference	R Difference
$64 \rightarrow 32$	$1.32 \cdot 10^{-4}$	$7.26 \cdot 10^{-5}$
$32 \rightarrow 16$	$7.08 \cdot 10^{-5}$	$4.72 \cdot 10^{-5}$
$16 \rightarrow 8$	$3.52 \cdot 10^{-5}$	$8.20 \cdot 10^{-5}$
$8 \rightarrow 4$	$3.25 \cdot 10^{-5}$	$2.77 \cdot 10^{-5}$
$4 \rightarrow 2$	$1.25 \cdot 10^{-5}$	$1.87 \cdot 10^{-6}$
$2 \rightarrow 1$	$7.03 \cdot 10^{-6}$	$7.04 \cdot 10^{-6}$
$1 \rightarrow 1/2$	$3.74 \cdot 10^{-6}$	$4.21 \cdot 10^{-6}$
$1/2 \rightarrow 1/4$	$2.12 \cdot 10^{-6}$	$1.98 \cdot 10^{-6}$

Table 9.6: Three-dimensional temporal convergence for deforming droplet. Using 32 radial and angular gridpoints.

the droplet's leading edge converge spectrally as the number of points are doubled. Finally, both radial and angular points are held at 32 while the timestep is adjusted from a base of 10^{-4}. This temporal convergence check is shown in Table 9.6. As with the temporal convergence for the translating droplet, here we see a few occurrences where halving the timestep does not produce the expected halving of the metrics of interest. Reducing the timestep from 16 times the base to 8 times the base increases the difference in the location of the right endpoint when compared to the previous halving. Also, halving the timestep from 16 times the base to 8 times the base produces a volume difference of $3.52 \cdot 10^{-5}$ while a further doubling only results in a volume difference of $3.25 \cdot 10^{-5}$. Again, these are not considered worrying since they only occur for one of the two variables of interest at either halving and after that the difference continues to halve with each halving of the timestep. We thus conclude

that the method is first order in time for the deforming droplet case.

Chapter 10

Three-Dimensional Results

10.1 Introduction

Initial conditions are given by the steady-state solution to the axisymmetric problem, a paraboloid:

$$h = \frac{\theta_I}{2R_I}\left(R_I^2 - r^2\right) \tag{10.1}$$

with θ_I being the initial contact angle of the droplet and R_I being the droplet's initial radius.

As previously mentioned, to have the dimensional volume of the droplet remain a constant, we must enforce that

$$\theta_I R_I^3 = \frac{1}{3}. \tag{10.2}$$

To satisfy this relationship we specify θ_I and then force R_I. The initial contact angle is given as the average of the advancing and receding contact angles,

$$\theta_I = \frac{\theta_{Adv} + \theta_{Rec}}{2}. \tag{10.3}$$

Also, unless otherwise specified, (8.72) is used as the contact angle – slip velocity relation.

10.2 Effects of Inclination Angle on Stability

An important aspect of droplet motion is determining the various stability boundaries as a function of the physical parameters. On an inclined plane, a droplet may become "stuck" on the surface, with the forces operating on the droplet remaining in equilibrium, it may translate in a steady state down the surface at a constant

velocity, or it may continuously deform as it evolves down the plane. Three primary mechanisms govern the droplet's motion: first, the relative strength of gravity versus surface tension, represented by the Bond number, which, as it increases, exerts greater forces on the droplet to slide down the surface; second, the greater the hysteresis window ($\theta_{Adv} - \theta_{Rec}$), the more likely the droplet is to remain fixed to the surface; finally, the greater the inclination angle, the faster the droplet will translate down the surface. We can compute the stability boundary of the droplet as either a function of the inclination angle, holding the Bond number constant, or as a function of the Bond number, holding the inclination angle constant. In this section droplet motion will be discussed as a function of the inclination angle.

Kim *et al.*[49] construct the following analytic formulation for the steady sliding droplet velocity as a function of inclination angle:

$$U \sim \frac{\rho V g \left(\sin\left(\alpha\right) - \sin\left(\alpha_c\right)\right)}{\mu L c(\theta) \ln(\Lambda/\lambda)}, \tag{10.4}$$

where U is the steady velocity of the droplet, α_c is the critical inclination angle where the droplet begins sliding down the plane, L is the peripheral length of the drop/slid contact area, $c(\theta)$ is a monotonically decreasing function of contact angle, Λ is the length scale for which their wedge approximation of the droplet shape near the contact line holds, and λ is the cutoff length for which classical hydrodynamic theory ceases to hold (on the order of 1–100 nm). They derive this formula, given as equation (20) in their paper, by creating an energy balance between the gravitational potential energy of the droplet and the energy dissipated by the droplet sliding down the plane and solving for the speed when the two are equal. They showed that their results, when using (8.72) for the contact angle - slip velocity relationship, were reducible, in the lubrication limit, to those produced by Dussan V. and Chow[22]. Their results differed from those derived by Hocking[41] due to the limitations of Hocking's two-dimensional model.

We can compare our numerical calculations to (10.4) for the steady droplet sliding velocity. While (10.4) is dimensional and contains terms, such as the minimum distance over which continuum theory is valid, not included in our model, we can bypass a direct comparison by realizing that these parameters are constant for any given physical droplet. We instead compare the ratio of the analytical vs. numerical

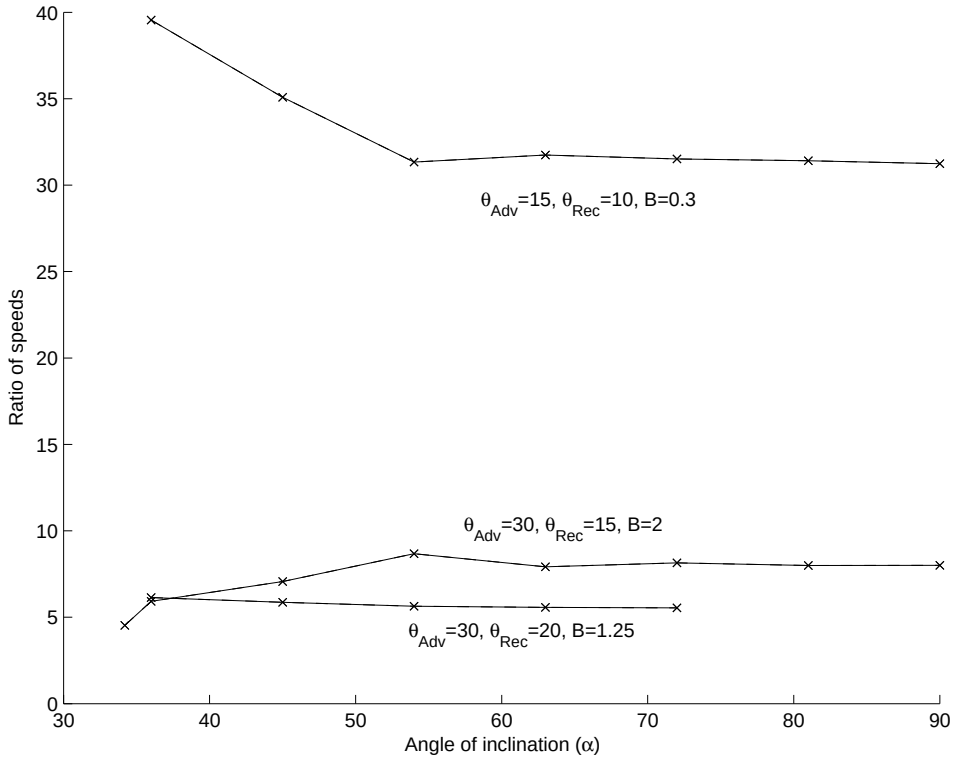

Figure 10.1: Comparison of speeds

results. We can then plot the ratio of velocities as a function of inclination angle. This comparison determines the relationship between the two computations; a straight line indicates that they differ only by a constant of proportionality. This constant is expected since we are neglecting constant terms from Kim *et al.*'s analytical formula.

To perform this comparison, we look at a droplet with $Ca = 0.1$. Solutions are then evolved in time until either a steady state or transient behavior was identified. The Bond numbers and advancing and receding static angles are given for each plot. As can be seen in Fig. 10.1, we get good agreement with Kim *et al.* for large inclination angles, but the agreement breaks down near the critical inclination angle, α_c. At this critical angle, the droplet breaks free of hysteresis and begins to translate down the substrate. The critical angle α_c is given by the leftmost point on the curves in Fig. 10.1. Obviously, the speed of the droplet is zero at angles lower than α_c and any comparison before this point is meaningless. Equation (20) of Kim *et al.* is highly sensitive when the inclination angle is near this critical angle. This sensitivity

is likely to be the cause of the discrepancies between the numerical and analytic results when α is close to α_c. If the numerical approximation to the critical angle is slightly off, then using this number in the analytic formula (as we do) will produce spurious "errors" when compared to the numerical results.

Examples of the steady-state droplet profiles for various inclination angles can be seen in Fig. 10.2. All the profiles are plotted with all of their origins at $x = 0$ for ease of viewing and the initial shape at $t = 0$ is also shown for reference. The $\alpha = 27^\circ$ droplet is stable and pinned to the substrate; it had some initial deformation but then became reattached to the plane. The $\alpha = 29^\circ - 32^\circ$ droplets are all traveling down the plane in the same basic steady-state profile. The minute differences in their shapes would not be noticeable in the scale presented here and they are all represented by a single curve. Snapshots of the droplet motion at $t = 1000$ are shown in Fig. 10.3. These are top-down views of the droplet near the critical angle of inclination, hence the spreading is only minor. At this point in time, the $\alpha = 27^\circ$ droplet has become re-attached to the plane. The $\alpha = 32^\circ$ droplet has finished temporary deformations and has reached its steady-state shape. The $\alpha = 29^\circ$ and $\alpha = 31^\circ$ droplets are still undergoing deformations. As shown in Fig. 10.2, they will eventually settle down into the same shape as the $\alpha = 32^\circ$ droplet, but they have not reached that shape by $t = 1000$. The $\alpha = 32^\circ$ droplet will continue to travel down the plane at its steady velocity while the $\alpha = 29^\circ$ and $\alpha = 31^\circ$ droplets deform and travel at a slower speed. It is only once they reach the steady-state shape that they will be traveling at the same speed as the $\alpha = 32^\circ$ droplet. By that point, however, the $\alpha = 32^\circ$ droplet will have traveled much further down the plane. The droplets in Fig. 10.2 are shown all starting at $x = 0$ for this reason; otherwise they would be strung out over a wide area and it would be difficult to compare their shapes.

Table 10.1 shows the computed critical inclination angles versus those predicted by Kim *et al.*[49] (setting their equations (7) and (9) equal to one another). We get very good agreement to the predicted critical angles. Their model makes the assumption that the droplet's contact area is close to a circle. While this is broadly true, our calculations indicate that the droplet stretches out, taking on a roughly ovoid profile, as seen in Fig. 10.3. This deviation from the assumption may be responsible for what discrepancies exist between the two calculations. Roura and Fort[69], like

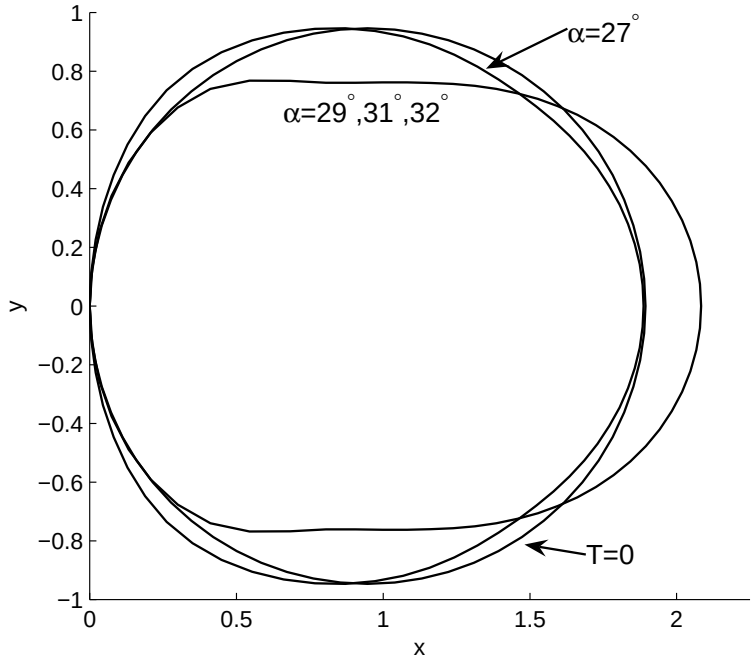

Figure 10.2: Comparison of steady-state shapes for different inclination angles. Origins have been moved to $x = 0$. $\theta_{Adv} = 30°, \theta_{Rec} = 15°, B = 2$

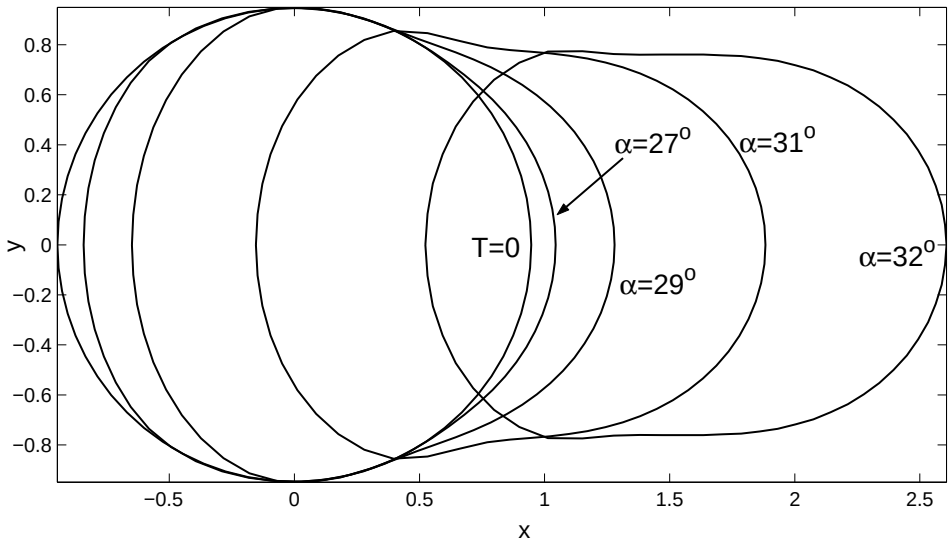

Figure 10.3: Comparison of spreading rates for different inclination angles. $\theta_{Adv} = 30°, \theta_{Rec} = 15°, B = 2, t = 1000$

θ_{Adv}	θ_{Rec}	B	Computed α_c	Kim α_c
30°	25°	2	11°	8°
30°	20°	2	20°	16°
30°	15°	2	27°	22°
30°	10°	2	32°	28°
30°	5°	2	34°	34°
15°	10°	0.5	20°	20°
15°	5°	0.5	36°	37°

Table 10.1: Comparison of critical angles

Kim *et al.*, calculate a relationship linking the critical angle of inclination to the contact angle. We do not compare our results to theirs due to difficulties in associating our advancing and receding contact angles to their single contact angle.

Krasovitski and Marmur[50] look at the differences between the front and back contact angles, θ measured at the front and rear of the droplet, and the advancing and receding contact angles, θ_{Adv} and θ_{Rec}. While they note that prior studies have always considered the two sets equal when the droplet is at the critical angle of inclination, α_c, they contend that there is no reason why the two should be identical. They examine two-dimensional droplets sliding down a heterogeneous surface, which provides for hysteresis. They find the highest angle of inclination for which a metastable equilibrium between the local geometric angle and ideal contact angle (i.e., the surface contact angle taking into account heterogeneity) is reached. For hydrophilic droplets, they find that while the advancing and front contact angles are almost identical at α_c, the back and receding contact angles are, in fact, quite different. They contend that the back contact angle is larger than θ_{Rec}, especially when θ_{Rec} is small. While this does not violate the slip velocity – contact angle relationship presented in (8.70), it does not agree with our results, which show that the rear contact angle is always equal to θ_{Rec} at α_c. Our results show that in every case the droplet undergoes a very rapid deformation starting from $t = 0$, wherein the rear contact angle decreases quickly, usually pushing below the hysteresis range. The rear contact angle then slowly increases, returning the rear contact angle to the very

edge of the hysteresis window. We also find that the front contact angle gradually moves from its initial value to just below the advancing contact angle. Krasovitski and Marmur only compute the contact angles of the pinned droplets at α_c, so the dynamics before then cannot be compared. If the angle of inclination is below α_c, the droplet can remain pinned to the surface while the front and rear contact angles remain within the hysteresis range (below θ_{Adv} and above θ_{Rec}, respectively). At α_c, however, the front and rear contact angles are equal to θ_{Adv} and θ_{Rec}. It is unclear what effect, if any, the fact that Krasovitski and Marmur rely on two-dimensional droplets rather than three-dimensional ones might play in the behavior seen.

10.3 Bond number stability

In this section, we compute the stability boundaries for a droplet where we hold the angle of inclination constant and vary the Bond number. The critical Bond number, B_d, for when a droplet begins translating for a given hysteresis window has been calculated for vertical droplets by Dimitrakopoulos and Higdon[20]. They specified a given Bond number and numerically computed the fixed shape that required the minimum hysteresis window ($\theta_{Adv} - \theta Rec$) using a spectral boundary element method combined with an optimization algorithm to find the equilibrium free surface. The droplet begins translating for $B > B_d$ while it's motion is arrested for $B < B_d$. We, however, specify the hysteresis window and compute the largest Bond number for which the droplet remains pinned to the surface. While Dimitrakopoulos and Higdon were only able to compute steady-state shapes, our code can calculate dynamics, in particular the steady state translating shapes. We are thus able not only to compare our results to theirs but also to extend the analysis to calculate a second critical Bond number at which the steady translation solutions no longer exist and an unsteady solution is observed. Please note that due to difference in the initial configuration of the droplet used to define the Bond number in Dimitrakopoulos and Higdon and our work, the Bond number from Dimitrakopoulos and Higdon, $B_{D\&H}$, has been rescaled to match our work: $2^{8/3}B_{D\&H} = B$.

In Fig. 10.4 we examine the behavior of a droplet on a vertical surface ($\alpha = 90°$). Starting with the initial configuration given by (10.1)–(10.3), we apply

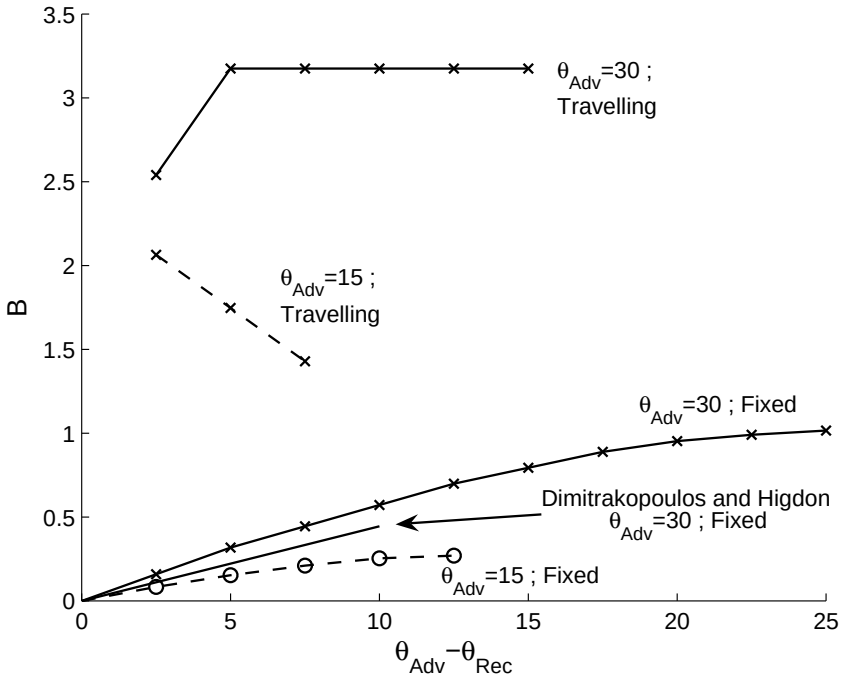

Figure 10.4: Stability as a function of Bond number and hysteresis window. The lower curves labeled 'Fixed' are the boundary between static and steady translating drops. The upper curves labeled 'Traveling' are the boundary between steady-state and unsteady translating drops.

our computational method to determine the evolution of the drop. Relatively good agreement with the results of Dimitrakopoulos and Higdon for $\theta_{Adv} = 30^o$ is seen. While they observed static droplets for a hysteresis window less than 10° when the advancing angle was 30°, we found static droplets for a hysteresis window of up to 25°. It should be noted that, for some of the cases considered, the droplet has some initial motion as it adjusts its shape from the initialized paraboloid, but then becomes fixed to the surface. The rear contact line is the first to move in this regime and it slides forward, shortening the droplet and steepening the forward contact line. Sometimes, as mentioned above, the droplet stabilizes before the forward contact line begins to move. Other times the forward contact angle becomes larger than the advancing contact angle and the droplet begins to advance forward. Once this begins, the droplet does not return to equilibrium and either continues down the plane as a steadily traveling droplet or else continues deforming. We ignore any transient behavior and consider the cases where the droplets return to stasis to still be below the critical Bond number.

For $\theta_{Adv} = 15^o$ and 30^o, Fig. 10.4 shows both the transition from fixed droplets to smoothly traveling droplets and then the transition from steady traveling droplets (lower curves) to unsteady droplets (upper curves). We discuss this latter transition, represented by the top two lines, shortly. The transition from fixed, or pinned, droplets to smoothly traveling ones is shown in the bottom three lines. The dashed line represents the $\theta_{Adv} = 15$ case and the solid line the $\theta_{Adv} = 30$ case, with the results from Dimitrakopoulos and Higdon[20] between them. As expected, a larger Bond number is required to force the droplet into motion as the hysteresis window increases, which is exactly what we see in Fig 10.4. This behavior is due to the fact that it is the back of the droplet that is the first to move and induce movement throughout the droplet. Thus a larger hysteresis window means a lower receding contact angle if the advancing contact angle is held fixed, as is the case with our code. This lower receding angle, in turn, allows the rear of the droplet to deform more before moving. Similarly, with a smaller advancing contact angle, the critical Bond number is lower.

The difference in droplet shapes between a pinned droplet and a smoothly translating droplet can be seen in Figs. 10.5 and 10.6. The different behaviors are

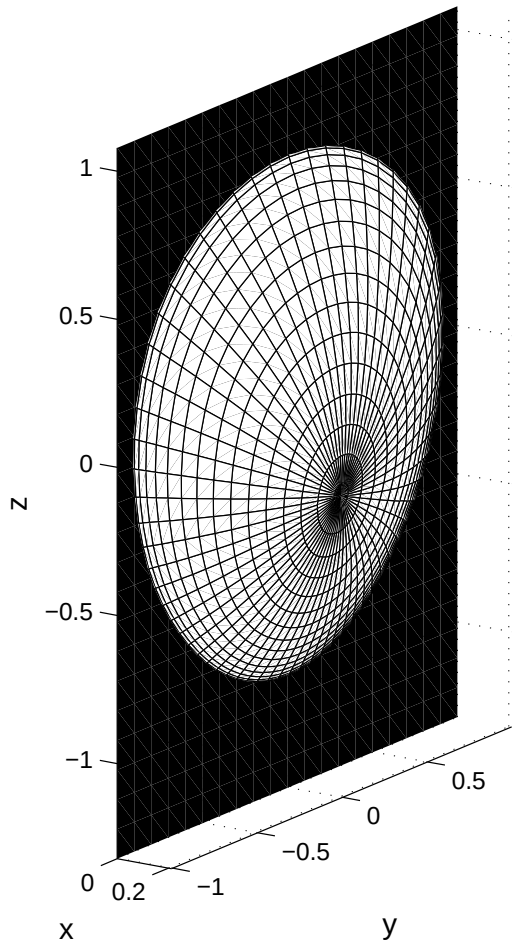

Figure 10.5: Pinned droplet: $\alpha = 90°, \theta_{Adv} = 30°, \theta_{Rec} = 20°, B = 0.635, t = 1000$

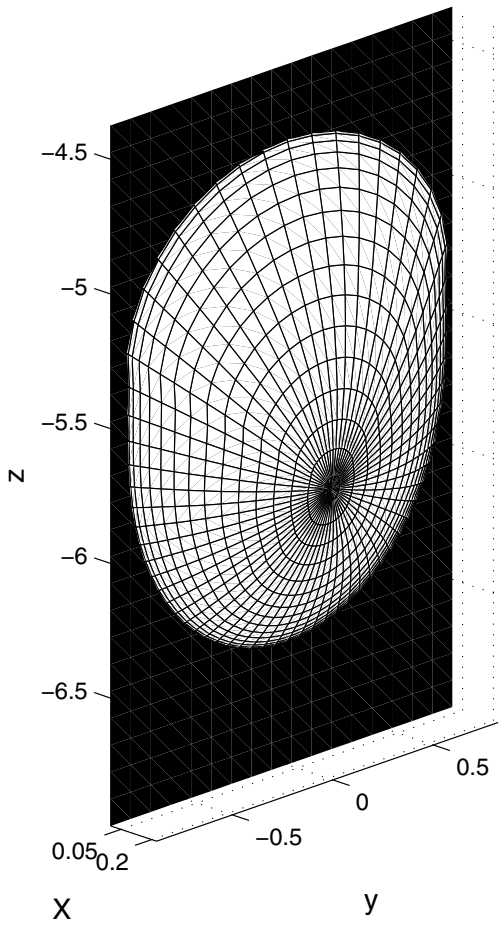

Figure 10.6: Smoothly translating droplet: $\alpha = 90°, \theta_{Adv} = 30°, \theta_{Rec} = 20°, B = 1.25, t = 1000$

due to increasing the Bond number while keeping all other parameters constant. Note how the pinned droplet is narrower at the front than the back. In the next section, we see that this behavior can be reversed, producing cusps in the rear while the front remains rounded. The translating droplet has elongated slightly and the front has steepened. This steepening is what allowed it to break free from hysteresis and begin translating.

As the force acting on the droplet is increased, either due to higher a Bond number or a greater inclination of the plane, the droplet breaks free from hysteresis and begins moving. If the hysteresis window is narrow enough, the droplet enters the smoothly translating state, the area between the upper and lower curves in Fig. 10.4. As the force acting on the drop increases, the droplet begins to deform and thus leaves the smoothly traveling regime. The droplet now begins deforming and does not return to a steady-state shape. This transition to deformation can also take place directly from the pinned state when the hysteresis window is large enough. The direct pinned to deformation transition is represented in Fig. 10.4 by the portions of the fixed line that are not below the traveling curve, thus signifying that the droplet transitions from the pinned state but not to the traveling state ($> 15^\circ$ for the $\theta_{Adv} = 30$ case and $> 7.5^\circ$ for the $\theta_{Adv} = 15$ case). Even larger Bond numbers cause this deformation to become more extreme, reaching the computational limits of our code. Above the traveling line (and above the fixed line where there is no traveling line above it), the droplets will continue to deform. Unlike the transition from pinned to steady translation, the transition from steady translation to deformation does not require ever increasing Bond numbers for greater hysteresis windows. This is most likely due to greater deformation that results from higher hysteresis window. The greater the window, the more extreme the deformation of the droplet before it begins to translate down the plane. It thus does not take that much extra force to push it out of the translating regime, as seen by the flat curve for $\theta_{Adv} = 30$ or the downward sloping curve for $\theta_{Adv} = 15$.

An example droplet profile for a deforming droplet is seen in Fig. 10.7. This picture is produced with the same parameters as those in Figs. 10.5 and 10.6 but with an even higher Bond number, $B = 1.25$, and at a much earlier point in time. This droplet has begun to spread quite rapidly, with the bulk of the fluid moving

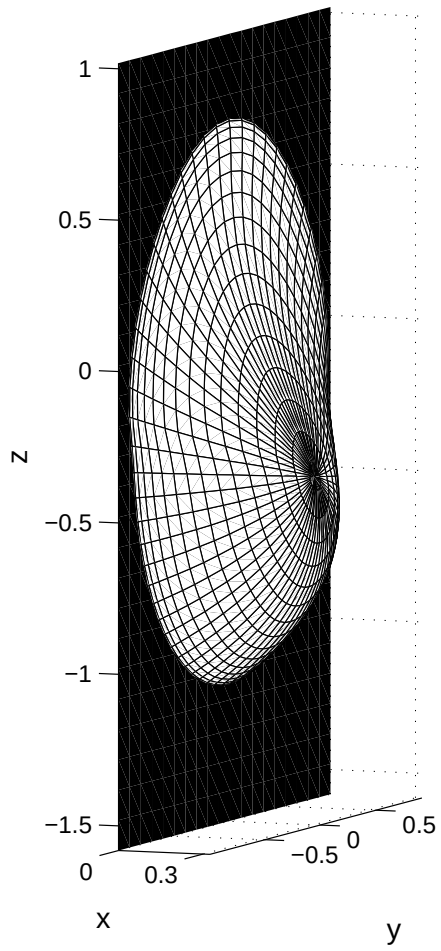

Figure 10.7: Deforming droplet. This droplet is near the computational limit for our code. $\alpha = 90°, \theta_{Adv} = 30°, \theta_{Rec} = 20°, B = 6.25, t = 7.5$

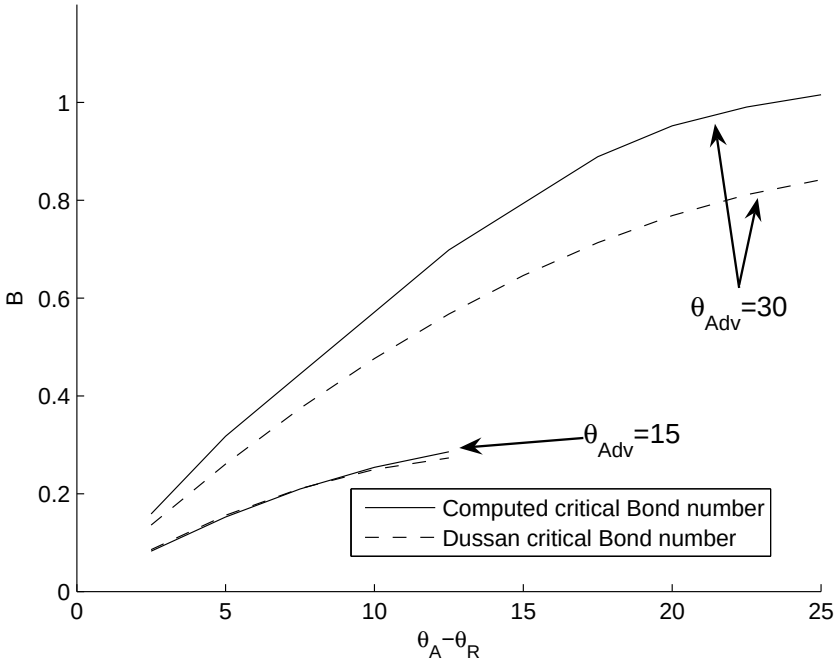

Figure 10.8: Comparison of critical Bond number with Dussan

toward the front of the drop and the rear of the droplet getting very thin. As time progresses, the fluid moves away from the rear faster than the contact line retreats toward the front. Eventually, the droplet is left with dry patches where there is no fluid within the contact line. This situation is obviously non-physical and represents the computational limit of the code in this situation.

We find that the smoothly translating droplet regime has a smaller stability window, as measured by the range of hysteresis for which the droplet is stable, than does the static droplet. If the droplet becomes too deformed, as results from a large hysteresis window, it bypasses the translating drop stage completely; once it begins to deform it does not stop but continues for as long as our code is able to model it. This phenomenon is visible in the early termination of the upper curves; this translating stability has a lower stability boundary than does the fixed droplet regime.

Dussan calculates the largest volume of a droplet that can remain stationary on an inclined plane[22]. This formulation can be transformed to show the largest Bond number which is stationary, as done by Dimitrakopoulos and Higdon[20]. We

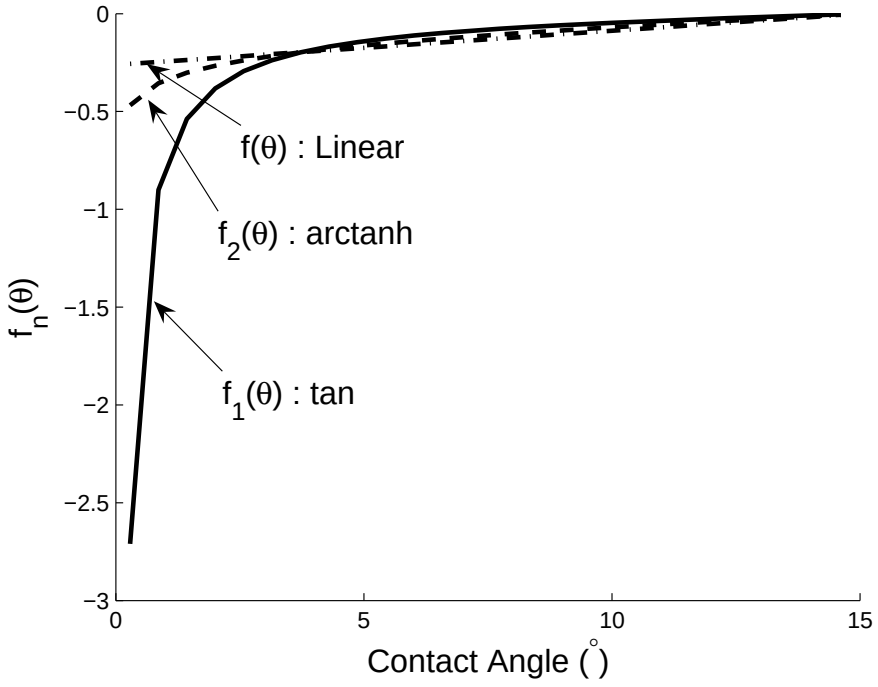

Figure 10.9: Comparison of contact angle – slip velocity relationships for $\theta_{Rec} = 30$

plot the comparison of our numerical calculation of critical Bond number with Dussan's asymptotic prediction in Fig. 10.8. The lower curve, $\theta_{Adv} = 15$, is much shorter since the hysteresis window can only be half as wide as in the $\theta_{Adv} = 30$ case. One potential source of divergence between Dussan's results and ours is that Dussan assumed only a small hysteresis window, $\theta_{Adv} - \theta_{Rec} \ll 1$. Thus it should not be surprising that the results diverge as we increase the hysteresis window and move away from the region in which the asymptotic result is valid.

When we are increasing the Bond number, it is possible for the effects of gravity to overpower the method. The droplet is move down the plane at a relatively high rate of speed, with the fluid in the rear convecting towards the front. This will reduce the contact angle in the rear of the droplet. The standard slip velocity – contact angle relationship (8.72) calls for the contact line velocity to increase linearly with the decrease in contact angle. Unfortunately, in some cases this is not fast enough. The contact angle does not retreat as fast as the fluid in the droplet. The results of this is that the contact angle becomes zero and the numerical method predicts negative

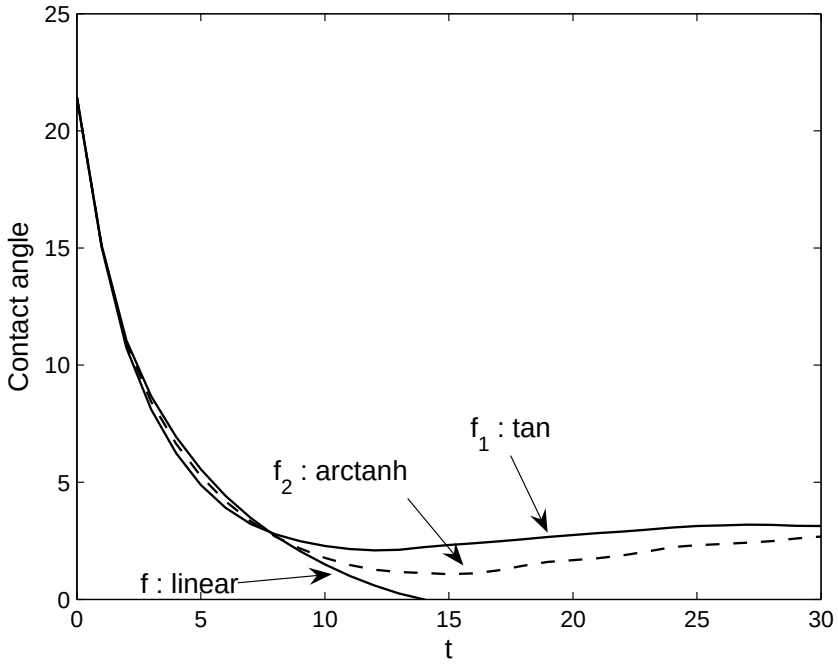

Figure 10.10: Comparison of contact angle at rear for different contact angle – slip velocity relationships. Here $\theta_{Adv} = 30°, \theta_{Rec} = 15°, B = 3.8$.

droplet height, a non-physical result. To correct this problem, we introduced two new contact angle – slip velocity relationships (8.73) and (8.74). The difference between these three relationships for $\theta \leq \theta_{Rec} = 30$ is shown in Fig. 10.9. As can be seen, the tan based f_1 (8.73) results in the largest velocity when the contact angle gets small, the existing linear relation f (8.72) has the smallest velocity for small contact angles, and the arctanh based f_2 (8.73) represents a middle ground.

An example of how these new slip laws can act to keep the contact angle in the rear from becoming negative is seen in Fig. 10.10. Here the droplet is initialized as the others in this section, but with $\theta_{Adv} = 30°, \theta_{Rec} = 15°, B = 3.8$. The existing linear contact angle – slip velocity relationship is obviously insufficient to keep the contact angle at the rear from becoming equal to zero. The arctanh based f_2 advances the contact line faster as the contact angle becomes small, and the tan based f_1 advances it the fastest, advancing the contact line faster and thus keeping the contact angle from getting too small. The location of the trailing edge of the droplet, formally

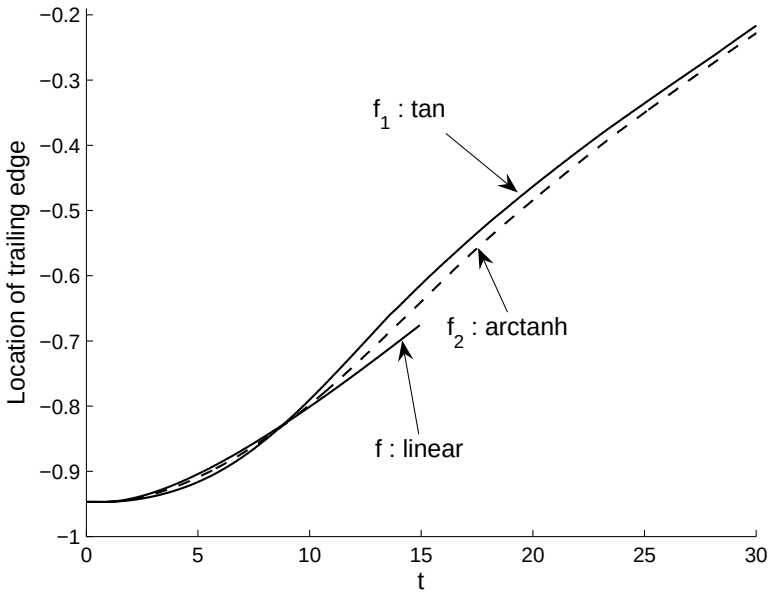

Figure 10.11: Comparison of trailing edge of droplet for different contact angle – slip velocity relationships. Here $\theta_{Adv} = 30°, \theta_{Rec} = 15°, B = 3.8$.

$L(0)$, is shown in Fig. 10.11. The new relationships do not need to move the contact line that much in order to prevent the rear contact angle from going negative. An important question is whether these results hold under grid refinement. We do not want the new contact angle – slip velocity relationships to only keep the contact angle from reaching zero for the chosen number of gridpoints. The results of a brief convergence check for f_1 are shown in Tables 10.2 and 10.2. The base number of gridpoints is 32 in both the angular and radial directions. These tables show how the minimum contact angle converges as the number of angular and radial gridpoints is increased. As can be seen, as the number of gridpoints is increased, the minimum contact angle gets closer and closer to a fixed, nonzero value. We are thus confident that the new contact angle – slip velocity relationships are able to prevent the contact angle at the rear of the droplet from becoming zero.

Since f_2 has a slower and less severe response to small contact angles than does f_1 (see Fig. 10.9), we expect to be able to find a case where it is incapable of responding fast enough to the contact angle becoming small. This behavior is seen in Fig. 10.12. Here $\theta_{Adv} = 15°, \theta_{Rec} = 2.5°, B = 3.2$ and the initial and rapid descent

Radial Gridpoints	Difference in Minimum Contact Angle
$8 \rightarrow 16$	$2.07 \cdot 10^{-1}$
$16 \rightarrow 32$	$1.56 \cdot 10^{-2}$
$32 \rightarrow 64$	$1.40 \cdot 10^{-3}$

Table 10.2: Radial convergence of contact angle – slip velocity relationship f_1. Using 32 angular gridpoints.

Angular Gridpoints	Difference in Minimum Contact Angle
$8 \rightarrow 16$	$3.05 \cdot 10^{-2}$
$16 \rightarrow 32$	$5.96 \cdot 10^{-3}$
$32 \rightarrow 64$	$2.31 \cdot 10^{-4}$

Table 10.3: Angular convergence of contact angle – slip velocity relationship f_1. Using 32 radial gridpoints.

in the contact angle at the rear has been cropped from the figure to focus on the behavior near zero. Please note that the contact angles are given in degrees, so the interface is nearly flat. The tan based f_1 retracts fast enough to keep the contact angle from going negative while the arctanh based f_2 does not.

The alternate contact angle – slip velocity relationships are not found to affect the stability curves in Fig. 10.4. The cases where they have an effect, those where the contact angle at the rear of the droplet gets very small, are cases where the droplet is already in the deformation regime. They have a mild effect on the spread rate of the translating drops, but do not affect the critical Bond numbers. While the problem of the contact angle going negative represents a limitation of our model, the problem only appears where the droplet is undergoing severe deformation. As long as we stay away from these cases, which are well above the top curves in Fig. 10.4, we can still use our linear (8.72) and trust the results that are produced.

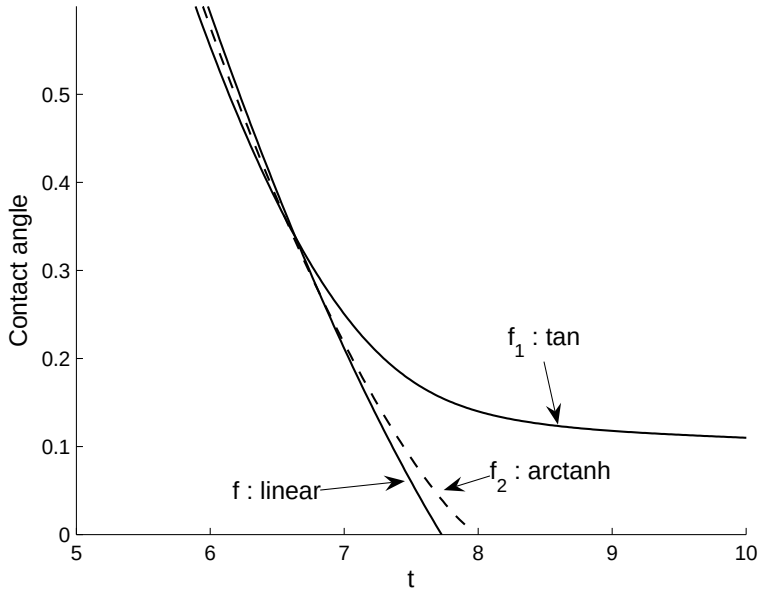

Figure 10.12: Comparison of contact angle at rear for different contact angle – slip velocity relationships. Here $\theta_{Adv} = 15°, \theta_{Rec} = 2.5°, B = 3.2$.

10.4 Rear angle

Stone *et al.*[76] and Amar *et al.*[1] have both formulated theories and problem formulations for the cusp formation and pearling behavior described by Podgorski *et al.*[66] and, although their theories differ, both find that pearling begins when the corner angle of the cusp becomes less than $\beta = \pi/6$ (Fig. 10.13 indicates the definition of β). Limat and Stone[54] have worked on developing a lubrication model to describe the nature of the cusp. Their model provides an analytic formulation for the height profile in the neighborhood of the cusp.

One way of looking at the behavior of the droplet is to look at the curvature of the rear, where we expect a cusp to form. The upper two curves in Fig 10.14 show the two-dimensional curvature of the contact line at $\phi = 0$ when $t = 200$ while the bottom two curves show the three-dimensional mean curvature of the surface at the same point. In these graphs, the plate is inclined at $\alpha = 81°$ and the capillary number is $Ca = 0.6$. The base contact angle – slip velocity relationship (8.72) is used. The two-dimensional curvatures are higher than the full three-dimensional

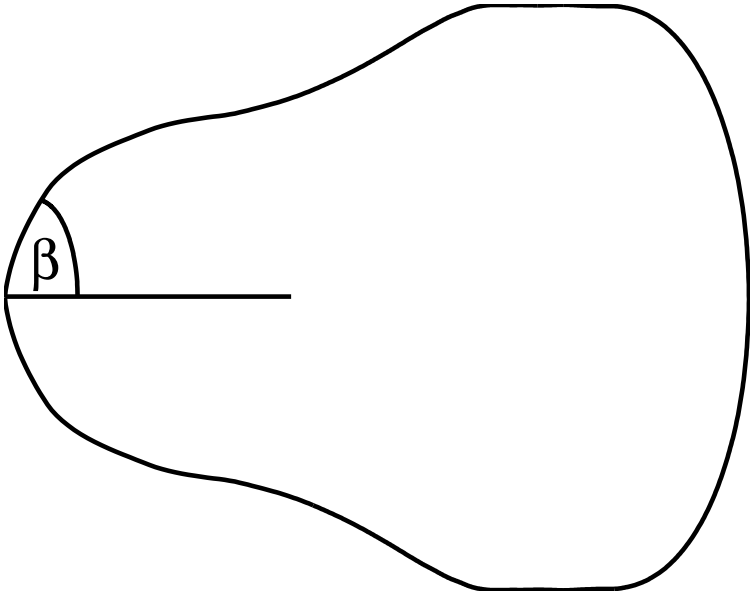

Figure 10.13: Example droplet shape showing rear contact angle β

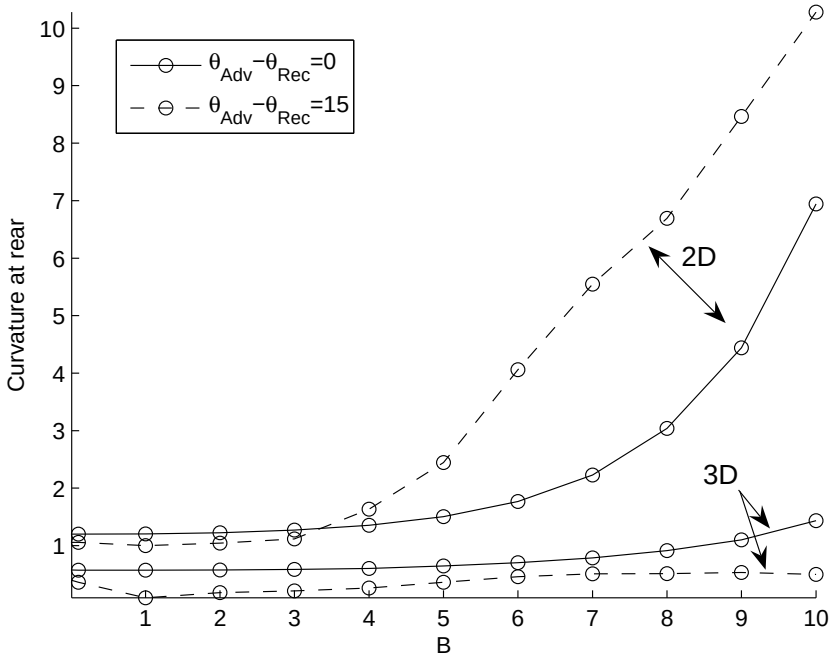

Figure 10.14: Curvature at rear of droplet

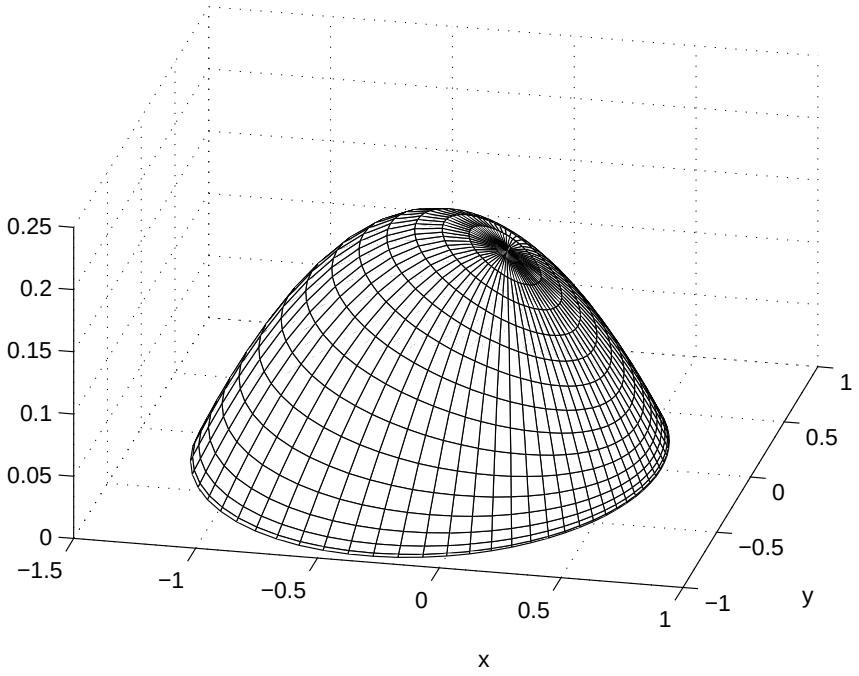

Figure 10.15: Droplet in pinned state with B=0.01

curvature because the droplets are, in a sense, the top portion of spherical caps. The mean curvature of a sphere is equal to $1/R$ everywhere on the sphere, while the two-dimensional curvature is equal to $1/r$, where r is the shrinking radius of the two-dimensional plane chosen. If the plane goes through the origin of the sphere, then $r = R$. If the plane does not go through the origin, though, then $r < R$ and thus the two-dimensional curvature is higher than the three-dimensional curvature.

As can be seen in Fig 10.14, both the two- and three-dimensional curvatures increase as the Bond number increases. The decline in three-dimensional mean curvature for B=1–3 is illustrated by Figs. 10.15 and 10.16. For $B = 0.01$, the droplet is still near its initial configuration. As it transitions to sliding down the substrate, the fluid flows to the front of the droplet, thinning the rear and reducing the three-dimensional curvature. As the droplet gains speed and begins to deform, the rear becomes narrower, thus increasing the two-dimensional curvature while having a reduced impact on the three-dimensional curvature since the droplet continues to thin in the rear.

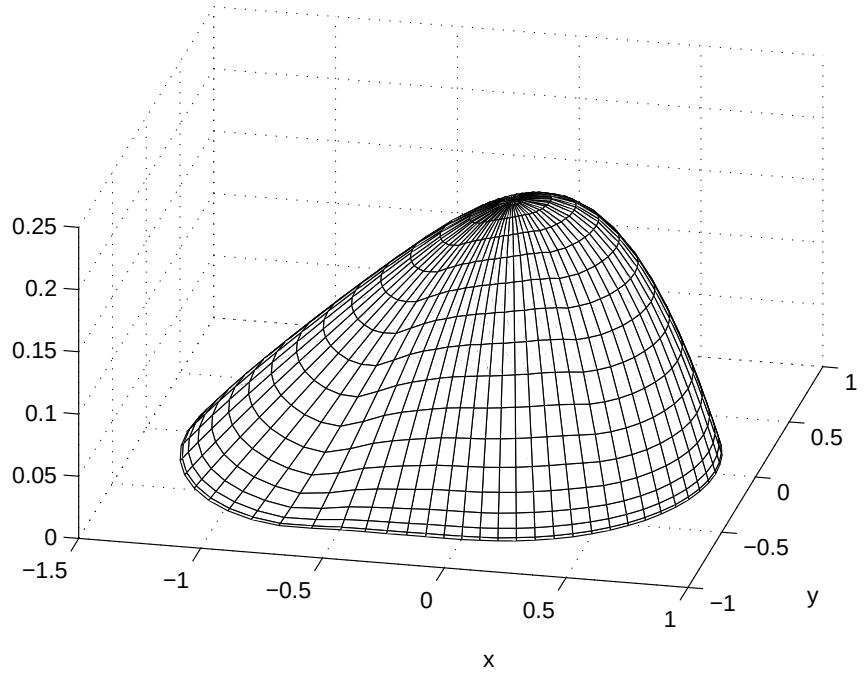

Figure 10.16: Droplet steadily traveling down substrate with B=3

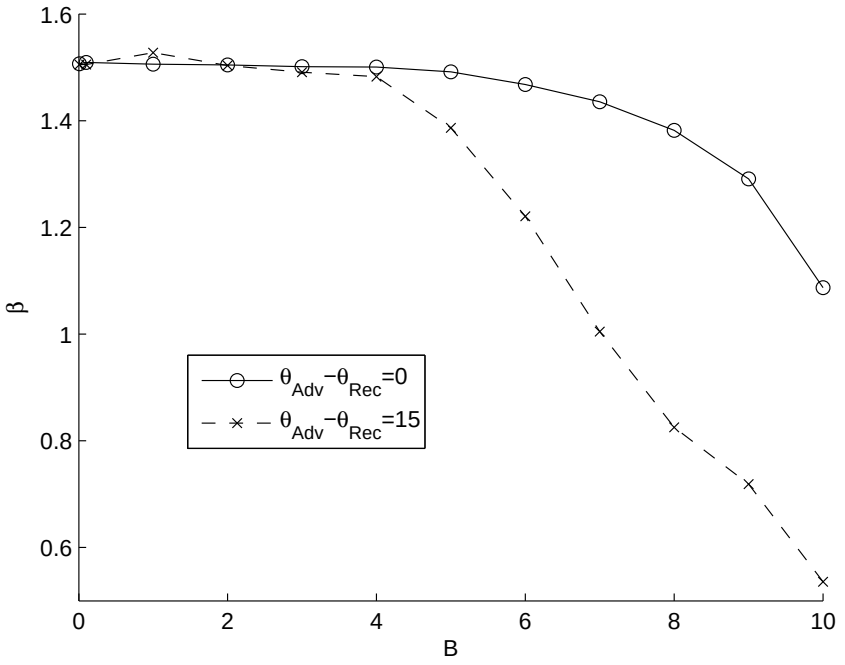

Figure 10.17: Rear angle of droplet

The rear angle of the droplet, β, is shown for different Bond numbers in Fig. 10.17. As can be seen, for a sufficiently large hysteresis window, $\theta_{Adv} - \theta_{Rec} = 15$, the rear angle approaches the critical $\beta = \pi/6 \sim 0.52$ value that is associated with the onset of pearling by Stone *et al.* and Amar *et al.*. This occurs at $B = 10$, which also represents the computational limit of our code. Past this point the code suffers instabilities and produces non-physical results. Our code is incapable of modeling the pearling behavior that is expected to occur at $\beta = \pi/6$ and thus we would expect that anything past this point would be a non-physical result. That our code suffers instabilities at this point may be taken as an indication that it is attempting to model behavior that it simply cannot do, and thus fails, showing that a new phenomenon, the pearling behavior, is encountered at $\beta = \pi/6$.

Chapter 11

Conclusion

The effects of insoluble surfactant on the spreading of a viscous droplet have been explored. The lubrication approximation was applied to the problem, and the resulting evolution equations were solved numerically using a pseudo-spectral method.

We first considered the spreading of an isothermal droplet with surfactant. It was found that surfactant decreases the spreading rate of the droplet by forming negative surface tension gradients near the contact line, which produced a Marangoni counterflow to oppose spreading. For a completely wetting droplet, i.e., $\theta_{Adv} = 0$, the concentration of surfactant and the magnitude of these gradients decreased as the droplet spread, allowing the drop to accelerate to nearly its clean spreading rate at large times. Increasing the surfactant Marangoni number, represented here by increasing β, slowed the droplet further by increasing the surface tension gradients. Similarly, increasing the Peclet number slowed the spreading rate by allowing for the surfactant to form steeper gradients, thus leading to larger surface tension gradients and stronger Marangoni flows.

We also studied the situation where surfactant was allowed to transfer onto and off of the droplet surface at the contact line. We used a linear relationship for the rate of transfer of surfactant between the contact line and the substrate. In this case, we found that a droplet that allows transfer at the contact line spreads faster than one with no-flux, if the droplet is losing surfactant to the substrate. If the droplet is gaining surfactant from the substrate it spreads slower than the no-flux case. The absorption of surfactant from the substrate offsets the decline in surfactant concentration along the interface due to the stretching of the interface, allowing the Marangoni counterflow to retain its strength longer. Similarly, the rapid loss of surfactant caused by desorption also reduces the slowing effect of the surfactant.

In the more extreme cases of rapid surfactant loss from the droplet interface, the presence of surfactant can increase the spreading rate of the droplet. The negative surfactant gradients in such cases are large enough to produce positive surface tension gradients and a reinforcing Marangoni flow, increasing the spreading rate.

Heating and hysteresis effects on droplet motion were studied for near steady state droplets. Without surfactant, the droplet would remain pinned in the hysteresis regime for some fixed amount of time and then break free due to heating. The presence of surfactant caused the droplet to slow its spreading rate, as seen in the isothermal case above. As the surfactant Marangoni number ($M_S = \beta/Ca$) was increased, the droplet could not break free of hysteresis and was permanently pinned. This result is a function of hysteresis, for without hysteresis, an increase in β would simply decrease the droplet's spreading rate.

We also allowed the steady contact angles of the droplet to vary with the surface tension at the contact line according to Young's Law. In this case, we found that, as before, a clean droplet would initially be pinned by hysteresis but then would eventually break free. We found that low surfactant Marangoni numbers (small β) delay the time at which the droplet breaks free. Increasing the surfactant Marangoni number (large β) further causes the droplet to remain pinned, as in the static steady contact angle case above. If we increase β even further, the droplet will immediately break free of the hysteresis regime and rapidly spread at a rate much faster than the clean droplet. This dependence of the contact angle on surface tension may explain experimental situations where surfactants are capable of drastically increasing the spreading rates of droplets.

We then studied the case where the substrate was assumed to have a surfactant gradient, the effect of which was to adjust its wettability. In this case, we were able to propel the droplet along the substrate at a faster rate than what was achieved through simply heating the substrate.

It is interesting to compare the results our model with some recent experiments by Nikolov *et al.*[63] on the spreading of droplets with surfactant. These authors were interested in studying superspreading and considered the spreading of 0.1 ml drops of a surfactant solution consisting of trisiloxane ethoxylate (Silwet L-77®) and water on polystyrene. The authors determined the spreading rate as a

function of surfactant concentration. With increasing surfactant concentration, the spreading rate initially increased, reached a maximum, and then decreased with increasing concentration. To explain this behavior, they first noted that as the droplet spreads, a surface tension gradient is generated along the interface as the interface stretches. The result is a lower surfactant concentration near the contact line than at the middle, and hence a surface tension gradient which enhances the spreading rate of the droplet. The effect is small at low concentrations, but as the surfactant concentration increases, so do the surface tension gradient and the rate of spreading. As the surfactant concentration increases further, the rate of surfactant diffusion from the bulk to the surface increases, which decreases the surface tension gradient on the interface and hence the rate of spreading. We can compare the results of Fig. 4.1 with these experiments. In this figure, we assume that the droplet will completely wet the substrate (i.e., $\theta_{Adv} = 0$). This is a reasonable assumption for the comparison since the presence of the surfactants in the experiments increases the spreading area of a water droplet, which in our model means decreasing θ_{Adv}. Our insoluble surfactant calculations suggest an additional possible reason for the observed decrease of spreading rate with concentration. As discussed in Sec. 4.2, we find that for the insoluble surfactant case, surfactant is driven along the interface towards the contact line as the drop spreads. This produces a surface tension gradient directed towards the center of the drop, and hence a Marangoni flow that opposes spreading. The result is a decrease in spreading rate with concentration as shown in Fig. 4.1. This mechanism clearly does not address the initial increase of spreading rate with concentration observed in the experiments of Nikolov *et al.*[63], but it may be a contributing factor at the higher concentrations for the situation they studied.

All the results discussed thus far were two-dimensional. While easy to compute, two-dimensional calculations can produce spurious results. Thus we next constructed a three-dimensional axisymmetric method to test our prior results. We did not include heat effects since they would break the included symmetry. We examined all the two-dimensional isothermal cases with the new three-dimensional axisymmetric method. While there were, of course, quantitative differences in the results, the important conclusion was that the qualitative behavior of the droplet and surfactant remained the same in three dimensions. Surfactant gradients still slowed down

the spreading rate of a wetting drop, with diminishing effects as the droplet continued to spread. One interesting development from the three-dimensional results was that it appeared that a boundary layer of surfactant developed near the contact line when the Peclet number became sufficiently large. Surfactant transfer to the substrate sped up spreading, and absorption from the substrate slowed spreading; both of these results are identical to the two-dimensional case. We thus feel confident that the two-dimensional results that include heat effects are also physically accurate.

Having explored the effects of surfactant and heat on the spreading of a droplet, we next looked at a droplet travelling down an inclined plane. Here gravity acts to propel the droplet down the plane. We only considered clean, isothermal droplets, so no surfactant effects were included. We constructed a composite lubrication theory solution to the Navier-Stokes equations, valid for all inclination angles α of the plane with respect to the horizontal. This necessitated enforcing the lubrication approximation with our initial data rather than the nondimensionalization. The first effect we considered was the stability of the droplet as the angle of the plane was changed. Hysteresis allows the droplet to remain "stuck" to the plane, if the contact angles remain within the hysteresis range while the plane is inclined. As the gravitational effects increase, either through greater inclination or increased Bond number, the droplet will break free and begin translating down the plane. We compared these translation speeds with the results of Kim *et al.*[49] and found good agreement. While there was some disagreement near the critical angle of inclination α_c, this was likely due to slight errors in measuring α_c and the sensitivity of the results when near this angle.

Determining the critical angle of inclination when the droplet began translating down the plane was then investigated. These results were again compared to those of Kim *et al.* and were found to be in close agreement. Their model made the assumption that the droplet remained circular, while our droplet deformed into an oblong shape, which likely accounts for some of the discrepancies.

We then turned to droplets sliding down vertical plates, where the parameter of interest was the Bond number. Here the droplet can be pinned to the plate due to hysteresis, smoothly translate down the plate at a constant velocity, or begin deforming and not return to either of the other two states. The hysteresis window,

$\theta_{Adv} - \theta_{Rec}$, played an important role in the droplet's behavior. As the window increased, it took larger Bond numbers to force the droplet to become unpinned and begin motion. For sufficiently large hysteresis windows, though, the droplet would transition directly from being pinned to continual deformation, never entering the steady translation state. The critical Bond numbers needed to force the droplet from the pinned state were compared to those found by Dimitrakopoulos and Higdon[20]. The results were quite close for the range of hysteresis windows considered by Dimitrakopoulos and Higdon; we computed pinned states for greater hysteresis windows than they reported. The critical Bond numbers were also compared to those found by Dussan[22]. When the hysteresis window was small, as assumed by Dussan, the results were in close agreement. Larger hysteresis windows resulted in slightly divergent results, as expected when we moved away from Dussan's assumptions. Our calculations reported that, in some cases, the droplet would briefly deform from its initial configuration before returning to a pinned state. We considered these cases to still be pinned since they remained stationary after this brief deformation. While the critical Bond number needed to force the droplet from the pinned state increased with the hysteresis window, the Bond number needed to transition the droplet from steadily translating to continual deformation was not found to increase with hysteresis window. We attributed this effect to the increased deformation that was allowed by the larger hysteresis windows before the droplet exited the pinned state. The droplet thus did not require as much additional force to move into the deformation regime.

As the droplet moves down the plane, the fluid tends to move towards the front of the drop. For sufficiently large Bond numbers, this movement happens quite rapidly. Fluid vacates the rear of the droplet near the contact line, causing the contact angle at the rear to decrease. The linear contact angle – slip velocity relationship proved insufficient to prevent the contact angle from becoming zero in some circumstances. It did not move the contact line back towards the body of the droplet rapidly enough. To solve this problem we introduced two new contact angle – slip velocity relationships, one based on tan and the other on arctanh. Both provided for large velocities when the contact angle became very small. We found that the arctanh model was superior to the base linear model, but could still result in zero contact angles. The tan based model solved this problem, converging to a nonzero contact

angle. The additional movement of the contact line at the rear of the droplet when compared to the linear case was small, but it was enough to keep the contact angle from becoming zero and producing nonphysical results. While the results solved a problem with the model, the problem only occurred when the droplet was deforming and the new contact angle – slip velocity relationships did not affect the computed stability diagram. Thus we determined that the linear relationship was valid for the cases of interest.

An interesting result of droplets sliding down inclined planes is that the droplets may experience "pearling" behavior whereby they shed small droplets in their wake. This pearling occurs when the rear of the droplet forms a cusp and the angle of this cusp equals $\pi/6$. We looked at droplets on plates inclined at 81° and showed that the rear curvature increased as the Bond number was increased. For a hysteresis window of $\theta_{Adv} - \theta_{Rec} = 15°$, we reached the computational limit of our code just as the rear angle reached the critical $\pi/6$. Since the numerical method we employed is incapable of reproducing the pearling behavior, we took it as a positive sign that the code became unstable at the point where the physics of the droplet diverged from what the code was capable of reproducing.

There is certainly much room for future work. Krasovitski and Marmur[50] recently investigated two-dimensional droplets on an inclined plane and found that the rear contact angle was sometimes well above θ_{Rec}. They contend that there is no physical reason why the contact angles need to be at the limits of the hysteresis window at the critical angle of inclination. In the three-dimensional results presented here, when the droplet was at the critical angle of inclination, the contact angle at the leading edge was almost perfectly equal to θ_{Adv} and the angle at the trailing edge was almost equal to θ_{Rec}. It is unclear if the difference in results is due to the two-dimensional nature of the experiments conducted by Krasovitski and Marmur. A two-dimensional model could be constructed to investigate the behavior. That would determine if this observation is a two-dimensional only effect or if there is something more fundamental occurring. Additionally, a thin precursor model that eliminates the contact line could be used to see if eliminating the slip velocity – contact angle relationship results in agreement with Krasovitski and Marmur.

Our three-dimensional computation method has certain limitations that

should be addressed. When the deformation is too severe, it can surpass the chosen resolution of the method. An adaptive regridding method would likely help to overcome this problem. It is also possible that, due to the Chebyshev pseudo-spectral method used, the points can bunch up severely in the neighborhood of the contact line. This is generally the result of the droplet becoming somewhat pinched in the neighborhood of the origin. The choice of the origin is thus an important decision. Place it to the front of the droplet and large deformations are clearly defined, but resolution at the rear of the droplet is degraded. Place the origin at the rear and any cusp-forming behavior is captured, but problems can occur if the fluid is pooled at the front. A seemingly good compromise is to keep the origin at the center of the drop. This, unfortunately, presents problems if the droplet becomes pinched or narrows as the rear is sharpening, or if the points bunch near the origin, as described above.

Pearling behavior also deserves further study. Our method, as currently implemented, is incapable of actually reproducing the pearling. It suffers general instabilities at the parameter values needed to induce pearling. A change to a method that allows for pearling, such as a level set method, would be most helpful. Also, a method that employs adaptive regridding would allow the regions of the droplet that undergo large deformations to be highly resolved without inducing instabilities elsewhere. While this would require moving away from spectral methods, the advantages would more than outweigh any extra computational costs.

Surfactants and heat effects were completely ignored in the study of three-dimensional droplets on inclined planes. Given that surfactants were found to balance a non-uniform thermal gradient in the two-dimensional case and pin the droplet, it would be interesting to see their effects when coupled with gravity. While the effect of the thermal gradient was ignored in the axisymmetric case due to symmetry, it could certainly be added to the full three-dimensional problem. It would be interesting to examine the surfactant distribution during droplet translation, as well as how a deforming droplet could create large surfactant gradients.

References

[1] M. B. Amar, L. J. Cummings, and Y. Pomeau. Transition of a moving contact line from smooth to angular. *Phys. Fluids*, 15(10):2949–2960, 2003.

[2] D. M. Anderson and S. H. Davis. The spreading of volatile liquid droplets on heated surfaces. *Phys. Fluids*, 7(2):248–265, 1995.

[3] A. Bayliss, A. Class, and B. J. Matkowsky. Roundoff error in computing derivatives using the Chebyshev differentiation matrix. *J. Comput. Phys.*, 116:380–383, 1994.

[4] S. W. Benintendi and M. K. Smith. The spreading of a non-isothermal liquid droplet. *Phys. Fluids*, 11(5):983–989, 1999.

[5] J. J. Bikerman. Sliding of drops from surfaces of different roughnesses. *J. Colloid Sci.*, 5:349–359, 1950.

[6] T. D. Blake and M. J. Haynes. Kinetics of liquid / liquid displacement. *J. Colloid Interface Sci.*, 30:421–424, 1969.

[7] M. S. Borgas and J. B. Grotberg. Monolayer flow on a thin film. *J. Fluid Mech.*, 193:151–170, 1988.

[8] A. Borhan and C.-F. Mao. Thermocapillary motion of deformable drops at finite reynolds and marangoni numbers. *Phys. Fluids A*, 4(12):2628–2640, 1992.

[9] M. L. Chabinyc, W. S. Wong, A. Salleo, K. E. Paul, and R. A. Street. Organic polymeric thin-film transistors fabricated by selective dewetting. *App. Phys. Lett.*, 81(22):4260–4262, 2002.

[10] J. Chen. Experiments on a spreading drop and its contact angle on a solid. *J. Colloid Interface Sci.*, 122:60–72, 1988.

[11] A. Chengara, A. Nikolov, and D. Wasan. Surface tension gradient driven spreading of trisiloxane surfactant solution on hydrophobic solid. *Colloids and Surfaces A*, 206:31–39, 2002.

[12] R. G. Cox. The dynamics of the spreading of liquids on a solid surface. Part 2. Surfactants. *J. Fluid Mech.*, 168:195–220, 1986.

[13] R. V. Craster and O. K. Matar. Surfactant transport on mucus films. *J. Fluid Mech.*, 425:235–258, 2000.

[14] S. Daniel, M. K. Chaudhury, and J. C. Chen. Fast drop movements resulting from the phase change on gradient surface. *Science*, 291(5504):633–636, 2001.

[15] S. H. Davis. Contact-line problems in fluid mechanics. *Trans. ASME E: J. Appl. Mech.*, 50:977–982, 1983.

[16] P. G. de Gennes. Wetting: Statics and dynamics. *Rev. Mod. Phys.*, 57:827–863, 1985.

[17] J. A. Diez and L. Kondic. Contact line instabilities of thin liquid films. *Phys. Rev. Lett.*, 86(4):632–635, 2001.

[18] J. A. Diez and L. Kondic. Instabilities in the flow of thin films on heterogeneous surfaces. *Phys. Fluids*, 16(9):3341–3360, 2004.

[19] J. A. Diez, L. Kondic, and A. Bertozzi. Global models for moving contact lines. *Phys. Rev. E*, 63:011208, 2000.

[20] P. Dimitrakopoulos and J. J. L. Higdon. On the gravitational displacement of three-dimensional fluid droplets from inclined solid surfaces. *J. Fluid Mech.*, 395:181–209, 1999.

[21] E. B. Dussan V. On the spreading of liquids on solid surfaces: Static and dynamic contact lines. *J. Fluid Mech.*, 11:371–400, 1979.

[22] E. B. Dussan V. On the ability of drops or bubbles to stick to non-horizontal surfaces of solids. Part 2. Small drops or bubbles having contact angles of arbitrary size. *J. Fluid Mech.*, 151:1–20, 1985.

[23] E. B. Dussan V. and S. H. Davis. On the motion of a fluid-fluid interface along a solid surface. *J. Fluid Mech.*, 65:71–95, 1974.

[24] P. Ehrhard. Experiments on isothermal and non-isothermal spreading. *J. Fluid Mech.*, 257:463–483, 1993.

[25] P. Ehrhard and S. H. Davis. Non-isothermal spreading of liquid drops on horizontal plates. *J. Fluid Mech.*, 229:365–388, 1991.

[26] G. E. P. Elliot and A. C. Riddiford. Dynamic contact angles. I. The effect of impressed motion. *J. Colloid Interface Sci.*, 23:289–298, 1967.

[27] C. G. L. Furmidge. Studies at phase interfaces. 1. the sliding of liquid drops on solid surfaces and a theory for spray retention. *J. Colloid Sci.*, 17:309–324, 1962.

[28] B. S. Gallardo, V. K. Gupta, F. D. Eagerton, L. I. Jong, V. S. Craig, R. R. Shah, and N. L. Abbot. Electrochemical principles for active control of liquids on submillimeter scales. *Science*, 283(5398):57–60, 1999.

[29] H. Gau, S. Herminghaus, P. Lenz, and R. Lipowsky. Liquid morphologies on structured surfaces: from microchannels to microchip. *Science*, 283(5398):46–49, 1999.

[30] D. P. Gaver, III and J. B. Grotberg. The dynamics of a localized surfactant on a thin film. *J. Fluid Mech.*, 213:127–148, 1990.

[31] D. P. Gaver, III and J. B. Grotberg. Droplet spreading on a thin viscous film. *J. Fluid Mech.*, 235:399–414, 1992.

[32] J. M. Gomba, J. Diez, A. G. González, and R. Gratton. Spreading of a micrometric fluid strip down a plane under controlled initial conditions. *Phys. Rev. E*, 71:016304, 2005.

[33] A. G. González, J. Diez, J. Gomba, and R. Gratton. Spreading of a thin two-dimensional strip of fluid on a vertical plane: Experiments and modeling. *Phys. Rev. E*, 70:026309, 2004.

[34] D. Gottlieb and S. A. Orszag. *Numerical Analysis of Spectral Methods: Theory and Applications*. SIAM, Philadelphia, PA, 1977.

[35] H. P. Greenspan. On the motion of a small viscous droplet that wets a surface. *J. Fluid Mech.*, 84:125–143, 1978.

[36] M. Grunze. Surface science: Driven liquids. *Science*, 283(5398):41–42, 1999.

[37] P. J. Haley and M. J. Miksis. The effect of the contact line on droplet spreading. *J. Fluid Mech.*, 223:57–81, 1991.

[38] S. He and J. B. Ketterson. Surfactant-driven spreading of a liquid on a vertical surface. *Phys. Fluids*, 7(11):2640–2647, 1995.

[39] L. M. Hocking. A moving fluid interface. Part 2. The removal of the force singularity by a slip flow. *J. Fluid Mech.*, 79:209–229, 1977.

[40] L. M. Hocking. Sliding and spreading of thin two-dimensional drops. *J. Q. Mech. Appl. Math.*, 34:37–55, 1981.

[41] L. M. Hocking. Spreading and instability of a viscous fluid sheet. *J. Fluid Mech.*, 211:373–392, 1990.

[42] L. M. Hocking. Rival contact-angle models and the spreading of drops. *J. Fluid Mech.*, 239:671–681, 1992.

[43] L. M. Hocking and M. J. Miksis. Stability of a ridge of fluid. *J. Fluid Mech.*, 239:671–681, 1993.

[44] R.L. Hoffman. A study of the advancing interface. i. interface shape in liquid-gas systems. *J. Colloid Interface Sci.*, 50:228–241, 1975.

[45] C. Huh and S. G. Mason. The steady movement of a liquid meniscus in a capillary tube. *J. Fluid Mech.*, 81:401–419, 1977.

[46] C. Huh and L. E. Scriven. Hydrodynamic model of steady movement of a sold / liquid / fluid contact line. *J. Colloid Interface Sci.*, 35:85–101, 1971.

[47] O. E. Jensen and J.B. Grotberg. The spreading of heat or soluble surfactant along a thin liquid film. *Phys. Fluids A*, 5(1):58–68, 1993.

[48] R. A. Johnson and A. Borhan. Stability of the shape of a surfactant-laden drop translating at low reynolds number. *Phys. Fluids*, 12(4):773–784, 2000.

[49] H.-Y. Kim, H. J. Lee, and B. H. Kang. Sliding of liquid drops down an inclined solid surface. *J. Colloid Interface Sci.*, 247:372–380, 2002.

[50] B. Krasovitski and A. Marmur. Drops down the hill: Theoretical study of limiting contact angles and the hysteresis range on a tilted plate. *Langmuir*, 21:3881–3885, 2005.

[51] E. Kreyszig. *Differential Geometry*. Dover, New York, 1991.

[52] S. Kumar and O. K. Matar. Instability of long-wavelength disturbances on gravity-modulated surfactant-covered thin liquid layers. *J. Fluid. Mech.*, 446:249–258, 2002.

[53] M. Lelah and A. Marmur. Spreading kinetics of drops on glass. *J. Colloid Interface Sci*, 82(518-525), 1981.

[54] L. Limat and H. A. Stone. Three-dimensional lubrication model of a contact line corner singularity. *Europhys. Lett.*, 65(3):365–371, 2004.

[55] P. Gilberto López, S. G. Bankoff, and M. J. Miksis. Non-isothermal spreading of a thin liquid film on an inclined plane. *J. Fluid Mech*, 324:261–286, 1996.

[56] P Gilberto López, M. J. Miksis, and S. G. Bankoff. Stability and evolution of a dry spot. *Phys. Fluids*, 13:1601–1614, 2001.

[57] O. K. Matar. Nonlinear evolution of thin free viscous films in the presence of soluble surfactant. *Phys. Fluids*, 14(12):4216–4234, 2002.

[58] O. K. Matar, R. V. Craster, and M. R. E. Warner. Surfactant transport on highly viscous surface films. *J. Fluid Mech.*, 466:85–111, 2002.

[59] O. K. Matar and S. M. Troian. Linear stability analysis of an insoluble surfactant monolayer spreading on a thin liquid film. *Phys. Fluids*, 9(12):3645–3657, 1997.

[60] O. K. Matar and S. M. Troian. The development of transient fingering patterns during the spreading of surfactant coated films. *Phys. Fluids*, 11(11):3232–3246, 1999.

[61] M. J. Miksis. Contact lines. In D. Givoli, M. J. Gnote, and G. C. Papanicolaou, editors, *A Celebration of Mathematical Modeling: The Joseph B. Keller Anniversary Volume*, pages 161–180. Kluwer Press, 2004.

[62] W. J. Milliken, H. A. Stone, and L. G. Leal. The effect of surfactant on the transient motion of Newtonian drops. *Phys. Fluids A*, 5(1):69–79, 1993.

[63] A. D. Nikolov, D. T. Wasan, A. Chengara, K. Koczo, G. A. Policello, and I. Kolossvary. Superspreading driven by Marangoni flow. *Adv. Colloid Interface Sci.*, 96:325–338, 2002.

[64] A. Oran, S. H. Davis, and S. G. Bankoff. Long-scale evolution of thin liquid films. *Rev. Mod. Phys.*, 69(3):931–980, 1997.

[65] H. J. Palmer and J. C. Berg. Hydrodynamic stability of surfactant solutions heated from below. *J. Fluid Mech.*, 51:385–402, 1972.

[66] T. Podgorski, J.-M. Flesselles, and L. Limat. Corners, cusps, and pearls in running drops. *Phys. Rev. Lett.*, 87(3):036102, 2001.

[67] W. H. Press, B. P. Flannery, S. A. Teukolsky, and W. T. Vetterling. *Numerical Recipes in FORTRAN: The Art of Scientific Computing*. Cambridge University Press, New York, 1992.

[68] E. Ramé. The spreading of surfactant-laden liquids with surfactant transfer through the contact line. *J. Fluid Mech.*, 440:205–234, 2001.

[69] P. Roura and J. Fort. Equilibrium of drops on inclined hydrophilic surfaces. *Phys. Rev. E*, 64:011601, 2001.

[70] A. M. Schwartz and S. B. Tejeda. Studies of dynamic contact angles on solids. *J. Colloid Interface Sci.*, 38:359–375, 1972.

[71] L. Shampine, R. Allen, and S. Pruess. *Fundamentals of Numerical Computing.* John Wiley & Sons, New York, 1996.

[72] M. K. Smith. Thermocapillary migration of a two-dimensional liquid droplet on a solid surface. *J. Fluid Mech.*, 294:209–230, 1995.

[73] M. K. Smith, S. W. Benintendi, and C. P. Benjamin. Thermocapillary Droplet Migration on an Inclined Solid Surface. *LNP Vol. 628: Interfacial Fluid Dynamics and Transport Processes*, 628:263–289, 2003.

[74] H. A. Stone. A simple derivation of the time-dependent convective-diffusion equation for surfactant transport along a deforming interface. *Phys. Fluids A*, 2(1):111–112, 1990.

[75] H. A. Stone and L. G. Leal. The effects of surfactants on drop deformation and breakup. *J. Fluid Mech.*, 220:161–186, 1990.

[76] H. A. Stone, L. Limat, S. K. Wilson, J.-M. Flesselles, and T. Podgorski. Singularité anguleuse d'une ligne de contact en mouvement sur un substrat solide. *C. R. Physique*, 3:103–110, 2002.

[77] L. H. Tanner. The spreading of silicone oil drops on horizontal surfaces. *J. Phys. D*, 12:1473–1484, 1979.

[78] U. Thiele and E. Knobloch. Sliding drops on an inclined plane. *Phys. Fluids*, 15(4):892–907, 2003.

[79] U. Thiele, K. Neuffer, M. Bestehorn, Y. Pomeau, and M. G. Velarde. Sliding drops on an inclined plane. *Colloids and Surfaces A*, 206:87–104, 2002.

[80] P. A. Thompson and S. M. Troian. A general boundary condition for liquid flow at surfaces. *Nature*, 389:360–362, 1997.

[81] L. N. Trefethen. *Spectral Methods in Matlab.* SIAM, Philadelphia, PA, 2001.

[82] S. M. Troian, E. Herbolzheimer, S. A. Safran, and J. F. Joanny. Fingering instabilities of driven spreading films. *Europhys. Lett.*, 10:25–30, 1989.

[83] D. T. Wasan, A. D. Nikolov, and H. Brenner. Droplets speeding on surfaces. *Science*, 291(5504):605–606, 2001.

[84] J. Zhang. *The dynamics of a viscous drop with a moving contact line*. PhD thesis, Department of Engineering Sciences and Applied Mathematics, Northwestern University, Evanston, IL, 2003.

A. Frobenius Analysis of Two-Dimensional Droplet

In this section we will perform a Frobenius analysis at the contact lines of the two-dimensional drop. This analysis will show the nature of the singularity that develops at the endpoint .

A.1 Right Endpoint

The behavior of the droplet near the right endpoint will be examined first. Here, $x = R$, and the droplet makes contact with the substrate with an angle θ. A stretching in an inner region is introduced by rescaling x by the following relationship:

$$R - x = \epsilon\xi, \tag{A.1}$$

where $\epsilon \ll 1$. The height of the droplet near the contact point is also rescaled. The boundary conditions on h are fulfilled via a generic stretching of the form

$$h = \frac{-\theta}{2R}(R - \epsilon\xi)^2 + \frac{R\theta}{2} + \epsilon^{\chi}H, \tag{A.2}$$

where χ is some as yet undetermined constant. We will now move our frame of reference with the contact line. In this frame

$$\xi = \frac{R - x}{\epsilon}. \tag{A.3}$$

Moving with the contact line means that time now scales as

$$\frac{\partial}{\partial t} = \frac{\partial\tau}{\partial t}\frac{\partial}{\partial\tau} + \frac{\partial\xi}{\partial t}\frac{\partial}{\partial\xi}, \tag{A.4}$$

$$\frac{\partial}{\partial t} = \frac{\partial}{\partial\tau} + \frac{\dot{R}}{\epsilon}\frac{\partial}{\partial\xi} \tag{A.5}$$

where $\tau = t$. Then, to leading order,

$$\frac{\partial h}{\partial t} = \frac{\dot{R}}{\epsilon}\frac{\partial h}{\partial\xi} \tag{A.6}$$

and

$$\frac{\partial S}{\partial t} = \frac{\dot{R}}{\epsilon}\frac{\partial S}{\partial \xi}. \tag{A.7}$$

The boundary conditions on the surfactant equation are used to pick the proper scaling by which to stretch the surfactant concentration S. The general form of the boundary condition is

$$(S - c_1) + c_2\frac{\partial S}{\partial x} = c_3, \tag{A.8}$$

with $c1$, $c2$, and c_3 being constants. Introducing stretched coordinates local to the contact line changes (A.8) to

$$(S - c_1) - \frac{c_2}{\epsilon}\frac{\partial S}{\partial \xi} = c_3. \tag{A.9}$$

This implies that, to leading order, the boundary condition is no-flux. Since this goes against our model, which allows for flux, S must be expanded as

$$S(\xi) = S_0 + \epsilon S_1(\xi) \tag{A.10}$$

in order to preserve flux at the contact line. Here S_0 is the concentration of surfactant at the contact line and $S_1(0) = 0$.

In order to derive the scaling on h, the most singular term in (2.104) is balanced against the velocity term $\dot{R}$ and then the value of χ that makes this balance possible is found:

$$\dot{R}\epsilon^{\chi-1}\frac{\partial H}{\partial \xi} = -\lambda\epsilon^{2\chi-3}\theta\xi H\frac{\partial^4 H}{\partial \xi^4}. \tag{A.11}$$

Balancing these two terms requires that

$$\chi = 2. \tag{A.12}$$

The rescaled variables are now introduced into (2.104) and the terms are collected by orders of ϵ. Balancing terms in (2.104), we find that the leading order terms in the droplet evolution equation are

$$-2\lambda\theta^2\xi\frac{\partial^3 H}{\partial \xi^3} - \lambda\theta^2\xi^2\frac{\partial^4 H}{\partial \xi^4} - 2\lambda\theta\left[-\beta\frac{\partial S}{\partial \xi} - \delta\left(N - Bi\theta\left(1 - NR\right)\right)\right] + 2\lambda\theta M_S\frac{\partial^2 S}{\partial \xi^2} - \dot{R}\theta = 0 \tag{A.13}$$

and the leading order terms in the surfactant transport equation are

$$\frac{\lambda}{Ca}\left(2\beta\frac{\partial^2 S_1}{\partial\xi^2}-\theta\xi\frac{\partial^4 H}{\partial\xi^4}-\theta\frac{\partial^3 H}{\partial\xi^3}\right)S_0+\frac{1}{Pe}\frac{\partial^2 S_1}{\partial\xi^2}=0. \tag{A.14}$$

A Frobenius analysis is performed by assuming a solution of the form

$$H(\xi)=a\xi^2\ln(\xi)+b\xi^2+c\xi^3\ln(\xi)+d\xi^3+e\xi^4\ln(\xi)+f\xi^4+\ldots \tag{A.15}$$

$$S_1(\xi)=g_1\xi+g_2\xi^2\ln(\xi)+g_3\xi^2+g_4\xi^3\ln(\xi)+g_5\xi^3+g_6\xi^4\ln(\xi)+\ldots \tag{A.16}$$

where $a, b, c, d, e, f, g_1, g_2, g_3, g_4, g_5$, and g_6 are constants.

Substituting these ansatzes into (A.13) and (A.14) and collecting orders of ξ allows one to solve the resulting equations at each order to determine the coefficients of (A.15)–(A.16). At $O(1)$ in (A.13)

$$-2\lambda\theta^2 a-2\lambda\theta\left[\beta g_1-\delta\left(N-Bi\theta\left(1-NR\right)\right)\right]-\dot{R}\theta=0 \tag{A.17}$$

and at $O(\ln(\xi))$ in (A.14) it is found that

$$\frac{\lambda}{Ca}\left(2\beta g_2-3c\theta\right)S_0+\frac{g_2}{Pe}=0. \tag{A.18}$$

Solving these two equations gives solutions for a and g_2, but these constants are not yet fully determined since g_2 includes c. Not surprisingly, the nature of the contact line singularity in the coupled system is, indeed, dependent upon the droplet height and surfactant concentration.

One must now go on to the next order to solve for a and g_2. At $O\left(\xi\ln(\xi)\right)$ in (A.13) it is found that

$$-12\lambda\theta^2 c+8\beta\lambda\theta g_2=0 \tag{A.19}$$

which can be solved to find that $c=0$. This gives the surprising result that $g_2=0$.

An initial formulation of the droplet height and surfactant concentration at the right endpoint can now be constructed:

$$\begin{aligned}h=\frac{-\theta}{2R}(R-\epsilon\xi)^2+\frac{R\theta}{2}&\\ +\epsilon^2\Bigg\{\frac{1}{2}\frac{2\lambda\left[\beta g_1+\delta\left(N-Bi\theta\left(1-NR\right)\right)\right]-\dot{R}}{\theta\lambda}\xi^2\ln(\xi)&\\ +b\xi^2+O(\xi^3)\Bigg\}&\end{aligned} \tag{A.20}$$

and

$$S = S_0 + \epsilon \left[g_1 \xi + O(\xi^2) \right], \tag{A.21}$$

where

$$g_1 = -\frac{\partial S}{\partial x}\bigg|_{x=R}. \tag{A.22}$$

One could go to higher order to pick up more terms in S and h but this is not needed for accuracy in the method.

A.2 Left Endpoint

The analysis at the left endpoint, $x = L$, is nearly identical to the above problem with a few differences, which are discussed below.

First, the stretching near the contact line, (A.1), now becomes

$$x - L = \epsilon \xi. \tag{A.23}$$

The height of the droplet is now stretched by

$$h = \frac{\theta}{2L}(L + \epsilon\xi)^2 - \frac{L\theta}{2} + \epsilon^{\chi} H. \tag{A.24}$$

The moving frame of reference is now defined as follows

$$\frac{\partial}{\partial t} = \frac{\partial \tau}{\partial t}\frac{\partial}{\partial \tau} + \frac{\partial \xi}{\partial t}\frac{\partial}{\partial \xi} \tag{A.25}$$

$$\frac{\partial}{\partial t} = \frac{\partial}{\partial \tau} - \frac{\dot{L}}{\epsilon}\frac{\partial}{\partial \xi} \tag{A.26}$$

As before, at leading order,

$$\frac{\partial}{\partial t} = -\frac{\dot{L}}{\epsilon}\frac{\partial}{\partial \xi}. \tag{A.27}$$

Finally, when the change of variables is performed, one sees that (A.9) becomes

$$(S - c_1) + \frac{c_2}{\epsilon}\frac{\partial S}{\partial \xi} = c_3. \tag{A.28}$$

This still results in the same scaling of S as in (A.10), namely

$$S(\xi) = S_0 + \epsilon S_1(\xi). \tag{A.29}$$

Also, as would be expected, here $\chi = 2$.

The rescaled variables are introduced into (2.104) and the terms are collected by orders of ϵ. The first order terms, those with the lower power of ϵ are $O(1)$ in the droplet evolution equation:

$$-2\lambda\theta^2\xi\frac{\partial^3 H}{\partial\xi^3} - \lambda\theta^2\xi^2\frac{\partial^4 H}{\partial\xi^4} - 2Ca\lambda\theta\left[-M_S\frac{\partial S}{\partial\xi} + M_T\left(N + Bi\theta\left(1 - NL\right)\right)\right] + 2Ca\lambda\theta M_S\frac{\partial^2 S}{\partial\xi^2} + \dot{R}\theta = 0 \quad \text{(A.30)}$$

and $O(\epsilon^{-1})$ in the surfactant transport equation is:

$$\lambda\left(-2M_S\frac{\partial^2 S_1}{\partial\xi^2} + \frac{\theta\xi}{Ca}\frac{\partial^4 H}{\partial\xi^4} + \frac{\theta}{Ca}\frac{\partial^3 H}{\partial\xi^3}\right)S_0 + \frac{1}{Pe}\frac{\partial^2 S_1}{\partial\xi^2} = 0. \quad \text{(A.31)}$$

A Frobenius analysis is performed exactly as before by assuming a solution of the form:

$$H(\xi) = a\xi^2\ln(\xi) + b\xi^2 + c\xi^3\ln(\xi) + d\xi^3 + e\xi^4\ln(\xi) + f\xi^4 + \ldots \quad \text{(A.32)}$$

$$S_1(\xi) = g_1\xi + g_2\xi^2\ln(\xi) + g_3\xi^2 + g_4\xi^3\ln(\xi) + g_5\xi^3 + g_6\xi^4\ln(\xi) + \ldots \quad \text{(A.33)}$$

where $a, b, c, d, e, f, g_1, g_2, g_3, g_4, g_5$, and g_6 are constants.

These ansatzes are substituted into (A.30) and (A.31) and terms are collected by order of ξ. By solving the resulting equations at each order, the coefficients of (A.32)–(A.33) are determined. At $O(1)$ in (A.30) it is found that

$$-2\lambda\theta^2 a - 2Ca\lambda\theta\left[-M_S g_1 + M_T\left(N + Bi\theta\left(1 - NL\right)\right)\right] + \dot{L}\theta = 0 \quad \text{(A.34)}$$

and at $O(\ln(\xi))$ in (A.31) one sees that

$$\lambda\left(-2M_S g_2 + \frac{3c\theta}{Ca}\right)S_0 + \frac{g_2}{Pe} = 0. \quad \text{(A.35)}$$

From here a and g_2 can be determined but, since g_2 references c, that term is also needed to understand the singularity in S. To find c one must go to the next order of terms, $O\left(\xi\ln(\xi)\right)$, in (A.30):

$$-12\lambda\theta^2 c + 8M_S Ca\lambda\theta g_2 = 0 \quad \text{(A.36)}$$

which can be solved to find that $c = 0$ and $g_2 = 0$.

An initial formulation of the droplet height and surfactant concentration at the left endpoint is given by:

$$h = \frac{\theta}{2L}(L+\epsilon\xi)^2 - \frac{L\theta}{2} + \epsilon^2\left\{\frac{1}{2}\frac{2Ca\lambda\left[M_S g_1 - M_T\left(N + Bi\theta\left(1-NL\right)\right)\right] + \dot{L}}{\theta\lambda}\xi^2\ln(\xi) + b\xi^2 + O(\xi^3)\right\} \quad \text{(A.37)}$$

and

$$S = S_0 + \epsilon\left[g_1\xi + O(\xi^2)\right] \quad \text{(A.38)}$$

where

$$g_1 = \left.\frac{\partial S}{\partial x}\right|_{x=L}. \quad \text{(A.39)}$$

The analysis ends here as these terms are sufficient to stabilize the numerical scheme.

B. Pseudo-Spectral Derivatives

All derivatives performed in this thesis are performed using pseudo-spectral methods. These methods have the advantage of very high accuracy for sufficiently smooth functions.

B.1 Chebyshev Derivatives

Chebyshev polynomials, $T_n(x)$, are a set of orthogonal polynomials defined by

$$T_n(x) = \cos\left[n \arccos(x)\right] \tag{B.1}$$

for $n = 0, 1, 2, \ldots$ on $x \in [-1, 1]$. A recursion relationship between the Chebyshev polynomials also exists and is sometimes easier to work with:

$$\begin{aligned} T_0(x) &= 1 \\ T_1(x) &= x \\ T_n(x) &= 2\, x\, T_{n-1}(x) - T_{n-2}(x). \end{aligned} \tag{B.2}$$

A very useful property of Chebyshev polynomials is their orthogonality relationship:

$$\int_{-1}^{1} \frac{T_n(x) T_m(x)}{\sqrt{1-x^2}} dx = \begin{cases} 0, & n \neq m \\ \frac{\pi}{2}, & n = m \neq 0 \\ \pi, & n = m = 0 \end{cases} \tag{B.3}$$

One can approximate any function $f(x)$ via a Chebyshev expansion. The pseudo-spectral approximation to $f(x)$ is arrived at by truncating the Chebyshev expansion after N terms:

$$f_N(x) = \sum_{k=0}^{N} a_k T_k(x) \tag{B.4}$$

where

$$a_k = \frac{2}{c_k \pi} \int_{1}^{-1} \frac{f(x) T_k(x)}{\sqrt{1-x^2}} \tag{B.5}$$

with

$$c_k = \begin{cases} 1, & k \neq 0 \\ 2, & k = 0. \end{cases} \tag{B.6}$$

Unfortunately, the Chebyshev approximation to a function is not useful to use in a numerical method as it requires that the values of the function f are known everywhere in the domain. A numerical method only knows the values of f at discrete points. The Chebyshev pseudo-spectral approximation is the solution to these difficulties. The coefficients a_k are computed by introducing the temporary variable $x = \cos(\theta)$ to transform (B.5) into a periodic domain and then applying the trapezoid rule. When transformed back into x, we arrive at:

$$\tilde{a}_k = \frac{2}{N\gamma_k} \sum_{j=0}^{N} \frac{f(x_j)T_k(x_j)}{\gamma_j} \tag{B.7}$$

where

$$\gamma_j = \begin{cases} 2, & j = 0, N \\ 1, & j \neq 0, N \end{cases} \tag{B.8}$$

and $x_j = \cos(\frac{j\pi}{N})$ is the j^{th} Chebyshev collation point for $j = 0, 1, \ldots, N$. The pseudo-spectral approximation of f is given by

$$\tilde{f}_N(x) = \sum_{k=0}^{N} \tilde{a}_k T_k(x). \tag{B.9}$$

It can be shown that for infinitely smooth functions, the Chebyshev approximation is "infinitely accurate." The feature is generally referred to as spectral accuracy and is highly advantageous as a Chebyshev approximation can accurately reproduce a function with far fewer collocation points than can other methods. For additional details on the derivation of the approximation, please see Gottlieb and Orszag[34].

Of primary interest is using the Chebyshev pseudo-approximation to take derivatives. The derivative can be expressed as a matrix operator, $\boldsymbol{D}$ whose elements are given by

$$D_{jk} = \begin{cases} \frac{\gamma_j}{\gamma_k} \frac{(-1)^{j+k}}{x_j - x_k}, & j \neq k \\ -\frac{1}{2} \frac{x_k}{1-x_k^2}, & j = k, \quad k = 1, 2, \ldots, N-1 \\ \frac{2N^2+1}{6}, & j = k = 0 \\ -\frac{2N^2+1}{6}, & j = k = N. \end{cases} \tag{B.10}$$

To take the derivative of a function f, the function is first expressed as an array $\boldsymbol{f}$ whose entries are $f(x_j)$. Then the derivative is given by

$$\frac{d\boldsymbol{f}}{dx} = \boldsymbol{D}f. \tag{B.11}$$

The derivative may also be taken via fast Fourier transforms, but this places limitations on the number of collocation points; these limitations are impossible to fulfill while avoiding placing a collocation point at the origin in three dimensions. We thus use the fast Fourier transform method in two-dimensional and three-dimensional axisymmetric problems and the matrix formulation is used for full three-dimensional computations. Bayliss *et al.*[3] have shown that a minor change to (B.10) can lead to much greater accuracy when computing higher derivatives. The modification is to change the diagonal entries to be

$$D_{ii} = -\sum_{j=0,\, j\neq i}^{N} D_{ij}. \tag{B.12}$$

This modification ensures that the entries in each row of the derivative matrix sum to zero. Roundoff error when numerically computing the entries can introduce small errors which are magnified when the matrix is raised to powers in order to compute higher derivatives.

B.2 Fourier Derivatives

A Fourier pseudo-spectral scheme has many of the advantages of Chebyshev derivatives but it requires a periodic domain. A finite term Fourier series approximation of a function can be created by

$$u_N(x) = \sum_{k=-N}^{N} a_k e^{ikx} \tag{B.13}$$

where

$$a_k = \frac{1}{2\pi}\int_0^{2\pi} u(y)e^{-iky}dy. \tag{B.14}$$

on the interval $x \in [0, 2\pi]$. This Fourier series approximation is not practical in numerical studies since the limitation on accuracy will be the integration method

used to compute a_k. This problem can be avoided by using equally spaced points on $[0, 2\pi]$ and using the trapezoid rule to integrate. The resulting pseudo-spectral approximation to u is given by

$$\tilde{P}_N u = \sum_{k=-N}^{N} \tilde{a}_k e^{ikx} \tag{B.15}$$

where

$$\tilde{a}_k = \frac{1}{2N}\frac{1}{c_k}\sum_{j=0}^{2N-1} u(x_j) e^{-ikx_j} \tag{B.16}$$

and

$$c_k = \begin{cases} 1, & |k| \leq N \\ 2, & |k| = N. \end{cases} \tag{B.17}$$

The $2N$ evenly spaced collocation points are given by $x_j = \pi j/N$. As with the Chebyshev approximation, the Fourier approximation is highly accurate and produces extremely accurate derivatives at the collocation points x_j. The r^{th} derivative of u is approximated as

$$\frac{d^r}{dx^r}\tilde{P}_N u\Big|_{x=x_k} = \sum_{j=-N}^{N} (ij)^r \tilde{a}_j e^{ijx_k}. \tag{B.18}$$

As with the Chebyshev pseudo-spectral approximation, this derivative can be computed either using a matrix formulation or using fast Fourier transforms. The matrix $\boldsymbol{D}$ has the entries

$$D_{jk} = \begin{cases} \frac{1}{2}(-1)^{j+k}\cot\left(\frac{x_j - x_k}{2}\right), & j \neq k \\ 0, & j = k. \end{cases} \tag{B.19}$$

Since there are no limitations on the number of radial collocation points, there is no reason to not use 2^n collocation points and thus the fast Fourier transform method of computing the derivatives as it has a significantly shorter computation time than using the matrix formulation.